

UCLA

UCLA Electronic Theses and Dissertations

Title

Understanding and Manipulation of Emerging Quantum Phases in Topological Insulators

Permalink

<https://escholarship.org/uc/item/3j4560tx>

Author

Zhang, Peng

Publication Date

2021

Peer reviewed|Thesis/dissertation

UNIVERSITY OF CALIFORNIA

Los Angeles

Understanding and Manipulation of Emerging Quantum Phases in Topological
Insulators

A dissertation submitted in partial satisfaction of the
requirements for the degree Doctor of Philosophy in
Electrical and Computer Engineering

by

Peng Zhang

2021

© Copyright by

Peng Zhang

2021

ABSTRACT OF THE DISSERTATION

Understanding and Manipulation of Emerging Quantum Phases in Topological Insulators

by

Peng Zhang

Doctor of Philosophy in Electrical and Computer Engineering

University of California, Los Angeles, 2021

Professor Kang Lung Wang, Chair

Topological insulator (TI) is a new class of quantum material with inverted band structure caused by strong spin-orbit coupling (SOC), resulting an insulating bulk and topologically protected surface states. By introducing magnetism to break the time-reversal symmetry, it can host emerging topological quantum phases such as quantum anomalous Hall (QAH) effect, axion insulator quantum phase, and can host chiral Majorana fermion when coupled to superconductors. The goal of this dissertation is to study these quantum phases by material growth and transport measurements.

First, we studied the growth condition by molecular beam epitaxy (MBE) and achieved high quality magnetically doped topological insulator (MTI) film growth that can host QAH effect. To understand the different origins of zero Hall conductance plateau in QAH insulators and axion insulators, we carried out the thickness dependent study on MTI sandwiched structures and observed a dimension crossover between 2D QAH and 3D axion insulators by minor loops

measurements and scaling analysis. Then, we investigated the QAH insulator and antiferromagnetic heterostructures which offer an additional degree of freedom to manipulate the QAH state in MTI. By proximity coupling the QAH insulator to antiferromagnetic insulator Al-Cr₂O₃, we observed an exchange biased QAH effect, and the exchange bias can be effectively controlled by a field training process. In addition, chiral Majorana edge modes are reported to exist in QAH insulator and superconductors heterostructures. Aiming to understand the discrepancy of recent experimental reports, we fabricated QAH insulator with superconductor and normal metals hybrid devices, and we found the details of material characteristics, interface conditions play important roles on the experiment observations. Finally, two collaborative works closely related to the main scope of this dissertation are introduced. To probe the size limit and to understand the inter-channel scattering of QAH effect, we fabricated mesoscopic scale sub-micron size QAH insulator devices and carried out size dependent studies. Enabled by the successful growth of QAH film on insulating 2D van-der-Waals substrate MICA, we were able to fabricate dual-gate QAH device by exfoliation and transfer techniques. By applying a vertical electric field, we observe a topological phase transition from QAH to a trivial insulator state. This research will greatly improve the understanding of emerging topological quantum physics, and lead to the new revolution of quantum electronic devices.

The dissertation of Peng Zhang is approved.

Chee Wei Wong

Robert N. Candler

Yaroslav Tserkovnyak

Kang Lung Wang, Committee Chair

University of California, Los Angeles

2021

*This dissertation is dedicated to my family,
for their love, encouragement, and support*

TABLE OF CONTENTS

Chapter 1 Introduction.....	1
1.1 Topological insulator.....	1
1.2 Magnetic topological insulator.....	5
1.3 Quantum anomalous Hall.....	10
1.4 Axion insulator.....	15
1.5 Organization.....	17
Chapter 2 Molecular Beam Epitaxy Growth of Topological Insulators.....	19
2.1 Molecular beam epitaxy.....	19
2.2 MBE growth of TI and MTI.....	24
2.3 Cryogenic magneto-transport measurement.....	28
2.4 Recipe development for QAH.....	32
2.6 Summary of chapter 2.....	36
Chapter 3 Quantum anomalous Hall (QAH) effect and axion insulator.....	37
3.1 Dimension crossover from QAH to axion insulator.....	39
3.2 Zero-Hall plateau in QAH and axion insulator.....	40
3.3 Temperature scaling behaviors.....	43
3.4 Summary of chapter 3.....	47
Chapter 4 QAH insulator and antiferromagnetic heterostructures.....	49
4.1 Cr-BST/Cr ₂ O ₃ heterostructures.....	49
4.2 Cr-BST/Al-Cr ₂ O ₃ heterostructures.....	51
4.3 Interfacial coupling in Cr-BST/Al-Cr ₂ O ₃ probed by PNR.....	55

4.4 Exchange-biased QAH effect	57
4.5 Exchange-bias controlled by field training.....	60
4.6 Summary of chapter 4.....	63
Chapter 5 QAH insulator and superconductor heterostructures.....	65
5.1 Chiral Majorana Fermion in hybrid QAH-SC bilayers.....	66
5.2 QAH-SC and QAH-normal metal devices	68
5.3 Possible non-Majorana origins of the $\frac{1}{2}$ conductance plateau.....	71
5.4 Ultra-wide $\frac{1}{2}$ conductance plateau in another device.....	76
5.5 Summary of chapter 5	78
Chapter 6 Collaborative works	80
6.1 Size dependence of QAH in mesoscopic scale	80
6.1.1 QAH down to sub-micron size.....	81
6.1.2 Size dependence of QAH.....	83
6.1.3 Summary of chapter 6.1.....	90
6.2 Manipulation of QAH Through Electric Field.....	90
6.2.1 MBE growth of QAH quality Cr-BST on MICA.....	91
6.2.2 Dual-gated QAH devices.....	93
6.2.3 Electric field induced topological quantum phase transition	96
6.2.4 Thickness-dependent surface bands evolution.....	101
6.2.5 Summary of chapter 6.2.....	101
Chapter 7 Conclusion and Perspectives.....	103
References.....	104

LIST OF FIGURES

Figure 1- 1 Quantum spin Hall effect in 2D TI CdTe/HgTe/CdTe quantum wells.....	3
Figure 1- 2 Electronic band structure of 3D TI Bi ₂ Se ₃ measured by ARPES	5
Figure 1- 3 TRS-breaking magnetic topological insulators	6
Figure 1- 4 Coexistence of hole-mediated RKKY and bulk van Vleck mechanisms revealed by electric-field-controlled anomalous Hall effect	9
Figure 1- 5 Evolution of the subband structure upon increasing the exchange field	11
Figure 1- 6 The QAH effect in Cr-doped (Bi, Sb) ₂ Te ₃	12
Figure 1- 7 Scale-invariant QAH effect beyond 2D limit and metal-to-insulator transition in 6 QL Cr- (Bi, Sb) ₂ Te ₃	13
Figure 1- 8 Realization of axion insulator state	16
Figure 2- 1 MBE system in Device Research Lab at UCLA	20
Figure 2- 2 Schematic of RHEED pattern formation	22
Figure 2- 3 RHEED patterns of some typical surfaces.....	23
Figure 2- 4 Crystal structure of Bi ₂ Te ₃ TI family.	25
Figure 2- 5 Characterization of MTI growth	28
Figure 2- 6 PPMS system with and dilution fridge unit in Device Research Lab at UCLA.....	29
Figure 2- 7 Schematic of the Hall bar transport measurement setup	30
Figure 2- 8 Landauer Büttiker formalism on a Hall bar device.....	31
Figure 2- 9 Fermi level tuning by varying Bi to Sb ration.....	33
Figure 2- 10 Magnetic tuning by Cr doping	35

Figure 3- 1 Quantum anomalous Hall insulator and its sandwich heterostructures	39
Figure 3- 2 Minor loop hysteresis of QAH insulator and axion insulators	41
Figure 3- 3 Magnetic field dependence of σ_{xy} at various temperatures.....	44
Figure 3- 4 Conductivity tensor flow diagram at various temperatures.....	45
Figure 3- 5 Temperature scaling behaviors of the plateau-to-plateau transition.....	47
Figure 4- 1 QAH and exchange bias in Cr-BST/Cr ₂ O ₃ heterostructure.....	51
Figure 4- 2 Atomic structure and magnetic property of Al-doped Cr ₂ O ₃ . (a) Atomic and magnetic structure of Al-doped Cr ₂ O ₃	53
Figure 4- 3 High quality Cr doped BST grown by molecular beam epitaxy on Al-doped Cr ₂ O ₃ (0001).....	55
Figure 4- 4 Interfacial coupling between Al-Cr ₂ O ₃ and CBST layers probed by PNR.....	56
Figure 4- 5 Observation of quantum anomalous Hall effect in Al-Cr ₂ O ₃ /CBST heterostructure	59
Figure 4- 6 Exchange-biased quantum anomalous Hall effect.....	60
Figure 4- 7 Exchange bias manipulated by field-training of Al-Cr ₂ O ₃	61
Figure 4- 8 Exchange bias manipulated by field-training of Al-Cr ₂ O ₃	62
Figure 4- 9 Transport result of 6 nm undoped BST grown on Al-Cr ₂ O ₃	63
Figure 5- 1 Theoretical proposal and current experiment status for detecting CMF in hybrid QAH-SC bilayers	67
Figure 5- 2 Device fabrication and resistance characterization of superconductor Nb	69
Figure 5- 3 Transport results of quantum anomalous Hall insulator with various metal bars	70
Figure 5- 4 Half-integer longitudinal conductance plateau in QAH with normal metal Ti bar ...	72

Figure 5- 5 Explanation of Half-integer longitudinal conductance plateau by contact resistance condition.....	74
Figure 5- 6 Another QAH-superconductor device Nb #2 shows an ultra-wide $\frac{1}{2}$ conductance plateau	78
Figure 6- 1 QAH devices with sub-micron size fabricated by the hybrid method of photolithography and E beam lithography	82
Figure 6- 2 ρ_{xx} and ρ_{xy} of QAH devices with various sizes measured at 100K	83
Figure 6- 3 σ_{xx} and σ_{xy} of QAH devices with various sizes measured at different temperatures	84
Figure 6- 4 Transport result of QAH devices with various sizes measured at different temperatures.....	85
Figure 6- 5 Summary of the size dependence of QAH quality	87
Figure 6- 6 Size dependence of the current induced breakdown of QAH.....	89
Figure 6- 7 MBE growth of QAH quality Cr-BST on MICA.....	92
Figure 6- 8 Fabrication process of dual-gated QAH devices	94
Figure 6- 9 Single top-gate response of the QAH device	95
Figure 6- 10 Dual-gate response of the QAH device	96
Figure 6- 11 Electric field and carrier dependence	98
Figure 6- 12 Electric field induced topological quantum phase transition.....	99
Figure 6- 13 Electric field induced closing of surface magnetic gap.....	100
Figure 6- 14 Thickness dependent dual-gate response	101

ACKNOWLEDGMENTS

I would like to express my special thanks of gratitude to my advisor, Dr. Kang L. Wang, for his professional guidance and valuable support throughout my Ph.D. life. His passion and devotions to science deeply inspired me and shaped my life value and career goals. I would also like to thank Mrs. Wang for the warmest caring towards every DRL members. I would like to express my sincere appreciation to my committee members: Professor Chee Wei Wong, Professor Robert N. Candler and Professor Yaroslav Tserkovnyak for their time, encouragement and insightful guidance. I would like to thank the tremendous help I received from all the collaborators: Dr. Tomohiro Nozaki and Prof. Sahashi Masashi from Tohoku University, Dr. Alex Grutter and Dr. Purnima Balakrishnan from National Institute of Standards and Technology, Prof. Ni Ni from UCLA, Prof. Peter Yeh from Purdue University, Prof. Jing Shi from UC Riverside, Prof. Jing Xia from UC Irvine. One of the most valuable assets I received at DRL is the opportunity to work with excellent colleagues. I would like to thank Dr. Lei Pan and Dr. Peng Deng who taught me most experimental skills and shared me with great research insights into this field. I would like to thank Dr. Gang Qiu who led the collaborative work described in Chapter 6.1, and Dr. Sukong Chong who led the collaborative work described in Chapter 6.2. For both works, I worked on the QAH film growth and participated in part of the measurements. I would like to thank the financial support from the NSF under Grants No. 1936383 and No. 2040737, the U.S. Army Research Office MURI program under Grants No. W911NF-20-2-0166 and No. W911NF-16-1-0472. Last but not the least, I would like to thank the love and support I received from my parents in China. Though without meeting in person for more than five years, they gave me the ultimate strength to overcome all the hard times I have faced during my PhD life.

VITA

2016-2021 M.S./ Ph.D. Candidate, Electrical & Computer Engineering, UCLA, CA, US

2012-2016 B.S., Information Engineering (Optics), Zhejiang University, Hangzhou, China

Publications (*co-first author):

- [1] I. Rosen, C. Trimble, M. Andersen, E. Mikheev, Y. Li, Y. Liu, L. Tai, **P. Zhang**, K.L. Wang, Y. Cui, M. Kastner, J. Williams, D. Goldhaber-Gordon. "Fractional AC Josephson effect in a topological insulator proximitized by a self-formed superconductor." *arXiv*:2110.01039 (2021).
- [2] H. Wu, A. Chen*, **P. Zhang***, H. He, J. Nance, C. Guo, J. Sasaki, T. Shirokura, P. Hai, B. Fang, S. Razavi, K. Wong, Y. Wen, Y. Ma, G. Yu, G. Carman, X. Han, X. Zhang, K.L. Wang. "Magnetic memory driven by topological insulators." *Nature communications*, 12.1 (2021): 1-7.
- [3] L. Rodenbach, I. Rosen, E.J. Fox, **P. Zhang**, L. Pan, K.L. Wang, M.A. Kastner, D. Goldhaber-Gordon. "Bulk dissipation in the quantum anomalous Hall effect." *APL Materials* 9, no. 8 (2021):081116
- [4] T. Yu, H. Wu, H. He, C. Guo, C. Fang, **P. Zhang**, K. Wong, S. Xu, X. Han, K.L. Wang. "Large spin to charge conversion in antiferromagnetic Weyl semimetal Mn₃Sn. " *APL Materials* 9, no. 4 (2021): 041111.
- [5] Y.T. Yang, C. Hu, **P. Zhang**, N. Shakoorzadeh, N. Ni, K.L. Wang, S.S. Iyer. "Nb-based superconducting silicon interconnect fabric for cryogenic electronics." *Quantum Science and Technology* 6, no. 2 (2021):025014.
- [6] A. Shuvaev, L. Pan, **P. Zhang**, K.L. Wang, A Pimenov. "Faraday Rotation Due to Quantum Anomalous Hall Effect in Cr-Doped (Bi,Sb)₂Te₃." *Crystals* 11, no. 2 (2021): 154.
- [7] L. Pan, A. Grutter*, **P. Zhang***, X. Che, T. Nozaki, A. Stern, M. Street, B. Zhang, B. Casas, Q. He, E. Choi, S. Disseler, D. Gilbert, G. Yin, Q. Shao, P. Deng, Y. Wu, X. Liu, X. Kou, S. Masashi, X. Han, C. Binek, S. Chambers, J. Xia, K.L. Wang. "Observation of Quantum Anomalous Hall Effect and Exchange Interaction in Topological Insulator/Antiferromagnet Heterostructure." *Advanced Materials* 32, no. 34 (2020): 2001460.

- [8] L. Pan, X. Liu, Q. He, A. Stern, G. Yin, X. Che, Q. Shao, **P. Zhang**, P. Deng, C. Yang, B. Casas, E. Choi, J. Xia, X. Kou, K.L. Wang. "Probing the low-temperature limit of the quantum anomalous Hall effect." *Science advances* 6, no. 25 (2020): easaz3595.
- [9] H. Wu, F. Groß, B. Dai, D. Lujan, S.A. Razavi, **P. Zhang**, Y. Liu, K. Sobotkiewich, J. Förster, M. Weigand, G. Schütz, X. Li, J. Gräfe, K.L. Wang. "Ferrimagnetic Skyrmions in Topological Insulator/Ferrimagnet Heterostructures." *Advanced Materials* 32, no. 34 (2020): 2003380.
- [10] X. Che, Q. Pan, B. Vareskic, J. Zou, L. Pan, **P. Zhang**, G. Yin, H. Wu, Q. Shao, P. Deng, K.L. Wang. "Strongly Surface State Carrier-Dependent Spin–Orbit Torque in Magnetic Topological Insulators." *Advanced Materials* 32, no. 16 (2020): 1907661.
- [11] **P. Zhang**, L. Pan, G. Yin, Q. He, K.L. Wang. "A Note on Half-quantized Conductance Plateau of Chiral Majorana in Quantum Anomalous Hall Insulator and Superconductor Structures." *arXiv*:1904.12396 (2019).
- [12] H. Wu, **P. Zhang**, P. Deng, Q. Lan, Q. Pan, S. Razavi, X. Che, L. Huang, B. Dai, K. Wong, X. Han, K.L. Wang. "Room-temperature spin-orbit torque from topological surface states." *Physical review letters* 123, no. 20 (2019): 207205.
- [13] Q. Wan, **P. Zhang**, Q. Shao, M.T. Sharbati, J.R. Erickson, K.L. Wang, F. Xiong. "(Bi_{0.2}Sb_{0.8})₂Te₃ based dynamic synapses with programmable spatio-temporal dynamics." *APL Materials* 7, no. 10 (2019): 101107.
- [14] Q. Shao, C. Tang, G. Yu, A. Navabi, H. Wu, C. He, J. Li, P. Upadhyaya, **P. Zhang**, S. Razavi, Q. He, Y. Liu, P. Yang, S. Kim, C. Zheng, Y. Liu, L. Pan, R. Lake, X. Han, Y. Tserkovnyak, J. Shi, K.L. Wang. "Role of dimensional crossover on spin-orbit torque efficiency in magnetic insulator thin films." *Nature communications* 9, no. 1 (2018): 1-7.
- [15] Q. Shao, H. Wu, Q. Pan, **P. Zhang**, L. Pan, K. Wong, X. Che, K.L. Wang. "Room temperature highly efficient topological insulator/Mo/CoFeB spin-orbit torque memory with perpendicular magnetic anisotropy." In 2018 IEEE International Electron Devices Meeting (IEDM), pp. 36-3. IEEE, 2018. (San Francisco, CA, USA) Oral.

Chapter 1 Introduction

1.1 Topological insulator

Topological insulator (TI) is a new class of quantum materials which behaves as an insulator in its interior but contains conducting surface states [1-3]. Distinguished from other insulators, the surface states of TI have a spin-momentum locking mechanism where the spin polarization of surface electron is tightly locked to its momentum direction. These unique properties of TI are because its surface states are topologically protected Dirac fermions, and its non-trivial topology comes from the inverted band structure caused by strong spin-orbit coupling (SOC). In common semiconductor materials, the conduction band is usually formed from s-orbitals while valence band is usually formed from p-orbitals. The valence band has a lower energy than conduction band, thus causing a trivial band gap. On the contrary, due to the strong SOC in TI, its p-orbitals can locate at a higher energy level above s-orbitals, causing the band inversion (*i.e.*, band gap E_g is negative). As a result, topologically protected surface/edge states would arise when TI is interfaced with materials with a trivial bandgap (*e.g.*, vacuum), because the wavefunction must follow continuity law across the two medias.

Topological insulator in two-dimension (2D TI), is predicted to host dissipationless spin-polarized helical edge states and result in the quantum spin Hall (QSH) effect, which can be viewed as a quantized version of spin Hall effect [4]. Being protected by time-reversal symmetry (TRS), odd number of pairs of helical states cannot open a gap at the edge which ensures that the back-scattering by non-magnetic impurities are forbidden. The QSH insulators, 2D TIs, regarded as the most suitable candidate to implement the “electron/spin highway” concept, raised broad interests in spintronic applications as well as scientific studies in condensed matter physics. in

2006, B.A Bornevig et al. theoretically proposed the CdTe/ HgTe/ CdTe quantum well structure as a suitable candidate to host QSH state after fine tuning the HgTe thickness [5]. In fact, the CdTe/ HgTe/ CdTe quantum well can be described by an effective Hamiltonian given by [5]

$$H_{eff}(k_x, k_y) = \begin{bmatrix} H(k) & 0 \\ 0 & H^*(-k) \end{bmatrix} \quad (1 - 1)$$

$$H(k) = \varepsilon(k) + A(k_x\sigma_y - k_y\sigma_x) + m(k)\sigma_z \quad (1 - 2)$$

, where $\varepsilon(k) = C - D(k_x^2 + k_y^2)$ is the contribution from trivial band bending, $m(k) = m_0 + B(k_x^2 + k_y^2)$ is the gap parameter and σ_i are the Pauli matrices, and $H^*(-k)$ is unitarily equivalent to $H(k)$ for this system protected by the time reversal symmetry. As shown in Fig. 1-1 a, CdTe is a trivial semiconductor with s-type conduction band Γ_6 above its p-type Γ_8 valence band, while in HgTe the bands are inverted due to its strong SOC. The theoretical calculation suggests that the HgTe has a critical thickness d_c of 6.5 nm (Fig. 1-1 b), below which the structure is a trivial semiconductor dominated by CdTe, and above which the structure is a 2D TI and can host QSH effect. For $m/B < 0$ (i.e., $d < d_c$), the eigenstates of the model describe a trivial insulator. As the thickness of the HgTe quantum well increases, m becomes negative due to band inversion, and the $m/B > 0$ condition gives rise to the edge states of the QSH insulator. A schematic of the spin-polarized helical edge channels is shown in Fig. 1-1 c.

Followed by this proposal, the QSH effect was experimentally observed by König et al. in the CdTe/ HgTe/ CdTe quantum wells in 2007, as shown in Fig. 1-1 d [6]. Several samples with different HgTe thickness were prepared by molecular beam epitaxy (MBE), and resistance measurements were carried out at various gate voltages to tune the Fermi level in and out of its bulk gap. The authors found that, when HgTe thickness $d < 6.3$ nm, the longitudinal resistance became very large indicating the sample is a normal insulator. As the thickness increased to $d >$

6.3 nm, the longitudinal conductance tends to quantize at $2 e^2/h$ (where e is the electron charge and h is Planck's constant), matching well with the theory. Recently, beside the CdTe/HgTe quantum wells, the QSH effect has also been observed in other materials systems including InAs/GaSb quantum wells [7] and the single layer WTe_2 [8].

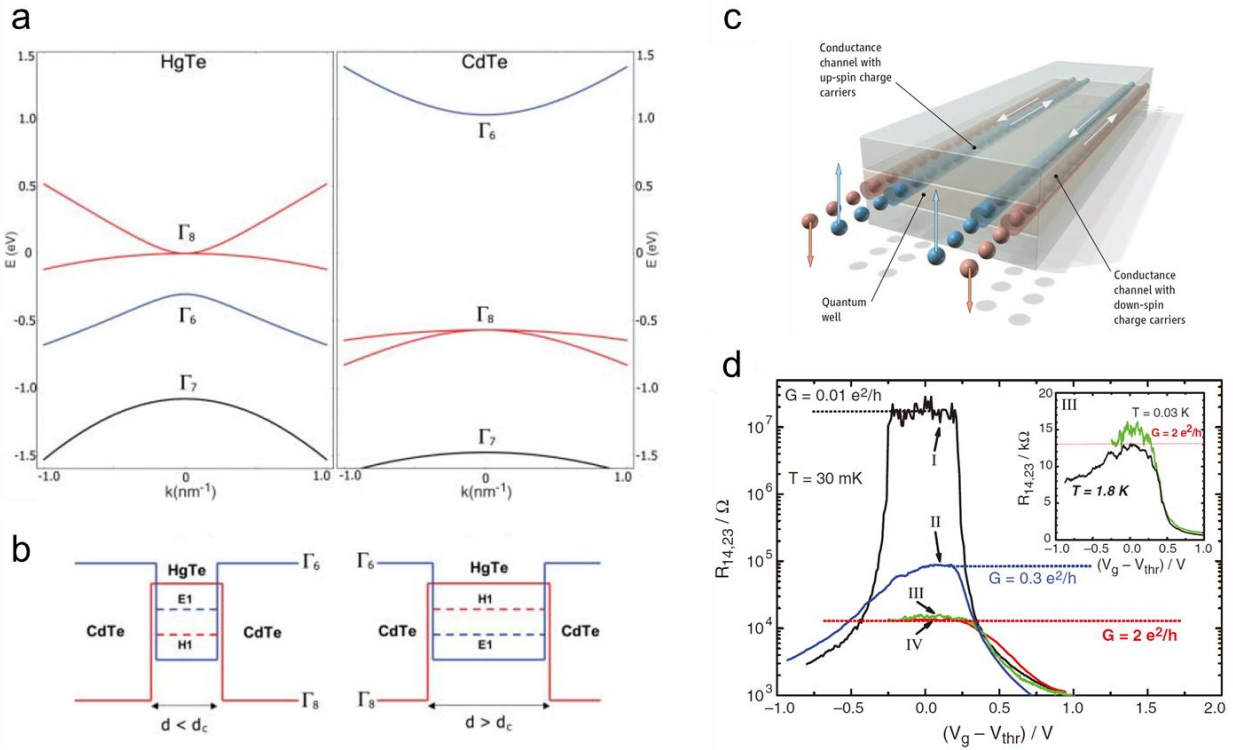


Figure 1- 1 Quantum spin Hall effect in 2D TI CdTe/HgTe/CdTe quantum wells. (a) Bulk energy bands of HgTe and CdTe near the Γ point. (b) Left: quantum well in normal regime $E_1 > H_1$ with HgTe thickness $< d_c$. Right: quantum well in inverted regime $H_1 > E_1$ with HgTe thickness $> d_c$. Adopted from Ref. [5]. (c) Illustration of the spin-polarized helical edge channels in a 2D TI. (d) Experimentally measured longitudinal four-terminal resistance, $R_{14,23}$, of various normal ($d = 5.5$ nm) (I) and inverted ($d = 7.3$ nm) (II, III, and IV) quantum well structures as a function of the gate voltage measured for $B = 0$ T at $T = 30$ mK. Adopted from Ref. [6].

From the above review, we can conclude that non-trivial band inversion due to strong SOC in 2D TIs can give rise to the QSH effect. The topological insulator theory can also be extended to three-dimensions, where the topologically non-trivial boundaries extend from the 1D edges to 2D surface states and the gapless surface states are protected by time-reversal symmetry [9], as schematically shown in Fig. 1-2 a. Based on the theory, F. Liang and C.L. Kane predicted that the $\text{Bi}_{1-x}\text{Sb}_x$ alloy with a critical Bi to Sb ratio would be a 3D TI [10]. One year later, D. Hsieh et al. applied surface-sensitive angle-resolved photoemission spectroscopy (ARPES) to observe the topological surface states in $\text{Bi}_{0.9}\text{Sb}_{0.1}$ for the first time [11], indicating the birth of 3D TI. However, the surface states and the underlying mechanism of $\text{Bi}_{1-x}\text{Sb}_x$ alloy turned out to be extremely complex. Instead, tetradymite-type materials Bi_2Se_3 , Bi_2Te_3 , and Sb_2Te_3 were later proposed to be 3D TIs with a single surface Dirac cone [12], and later been experimentally demonstrated by ARPES techniques [13-15]. The electronic band structure of Bi_2Se_3 measured by ARPES is shown in Fig. 1-2 b, c [14]. This tetradymite family tend to be preferable 3D TI families by researchers, as they have a single Dirac cone at Γ point and a bulk band gap up to 0.3eV, allowing for studying their surface states by transport measurement. In addition, they are layered single-crystalline materials that can be grown by MBE, which makes them become the most widely studied TI system. Especially Bi_2Te_3 and Sb_2Te_3 are able to form ternary 3D TI compound $(\text{Bi}_{1-x}\text{Sb}_x)_2\text{Te}_3$ where Bi to Sb ratio can be tuned during growth thus tuning its Fermi level position [16].

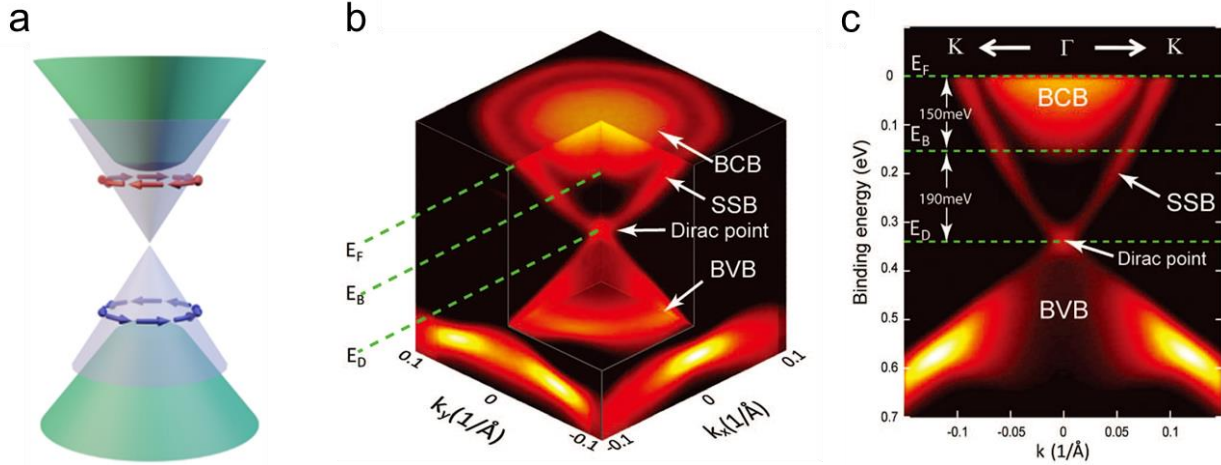


Figure 1- 2 Electronic band structure of 3D TI Bi₂Se₃ measured by ARPES. (a) Schematic of the band structure of 3D TI with spin-moment locked surface states. (b) The bulk conduction band (BCB), bulk valence band (BVB), and surface-state band (SSB) are indicated, along with the Fermi energy (E_F), the bottom of the BCB (E_B), and the Dirac point (E_D). (c) Band structure along the K- Γ - K direction, where Γ is the center of the hexagonal surface Brillouin zone (BZ). Adopted from Ref. [14].

1.2 Magnetic topological insulator

As described before, the surface states of TI are topologically protected by the time-reversal symmetry (TRS). From Eq. (1-1) and (1-2), the Hamiltonian for non-magnetic TI is protected by TRS given $H(k) = H^*(-k)$. However, it is also of great interest to introduce magnetic exchange interaction into TI, which will break the TRS of the topological surface states and result a gap opening at the Dirac point, making the surface Dirac fermion massive [14, 17, 18]. For magnetic TI, the mass term will change to

$$m(k) = m_0 + B(k_x^2 + k_y^2) + gM_z \quad (1 - 3)$$

, where M_z is the magnetic exchange term perpendicular to its surface. Consequently, $H(k) \neq H^*(-k)$ so the Hamiltonian no longer has TRS-protected property, and the massless surface Dirac fermions with linear dispersion will become massive where the Dirac point opens a gap, as shown in Fig. 1-3. Experimentally, Y.L. Chen et al. observed a small surface exchange gap opening in transition-metal Mn doped Bi_2Se_3 using ARPES [14]. L.A. Wray et al. also observed the surface exchange gap opening when they deposited Fe ions on top surface of Bi_2Se_3 [17]. The TRS-breaking physics and applications in magnetic TI can be multiplied through the interplay among the band topology (SOC strength), the magnetic orders (magnetic exchange coupling strength), and structural engineering. The breaking of time-reversal symmetry may lead to many other exotic physics including the quantum anomalous Hall effect (QAHE), axion electrodynamics, induced magnetic monopole, etc. [1, 19, 20].

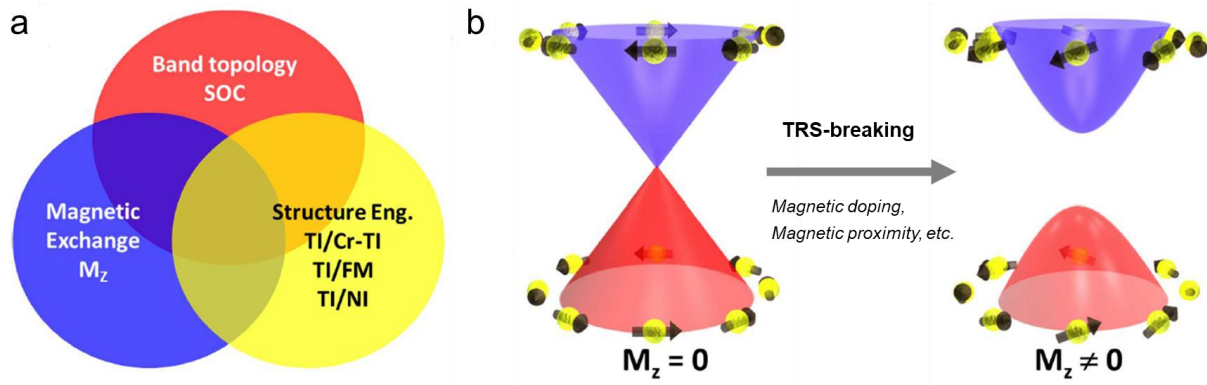


Figure 1- 3 TRS-breaking magnetic topological insulators. (a) The interplay among band topology, magnetic exchange, and structure engineering in the TRS-breaking phenomena. (b) Topological surface band diagram in undoped TI (massless) and MTI (massive), respectively. Adopted from Ref. [21].

In order to introduce magnetic exchange term M_z into TI, there are two widely studied approaches. First, by coupling TI with a topologically trivial magnetic material, the magnetic

proximity effect at the interface can locally align the spin moments of the TI electrons out of plane and thus breaking the TRS at the interface. Followed by this approach, ferromagnetism has been introduced into otherwise nonmagnetic TIs by proximity coupling to ferromagnetic insulator YIG [22-24], TmIG [25], EuS [26-28], Cr₂Ge₂Te₆ [29, 30], and antiferromagnetic CrSe [31] and CrSb [32]. However, the magnetization introduced by such short-range magnetic exchange coupling are usually very weak probably due to the poor interface quality.

Alternatively, directly doping magnetic ions into the host TI materials turns out to be a more effective approach to introduce robust magnetism. Zhang et al. reported a carried out detailed theoretical study on the stability, electronic, and magnetic properties of the magnetically doped topological insulators Bi₂Se₃, Bi₂Te₃, and Sb₂Te₃ [33], and they found the 3d transition metals favored the substitutional doping by using first-principles calculations within density functional theory [34]. Experimentally, transition metal doped TI have been successfully grown by chemical vapor deposition (CVD) [35], Bridgeman growth [36, 37], and MBE [38-41]. The MBE techniques has unique advantages of non-equilibrium growth, precise thickness and doping control, and capability of integrating heterostructures or superlattices. In fact, most of the exotic quantum physics were discovered in magnetically doped TI, due to its stronger magnetic exchange interaction and better controllability through MBE.

There are mainly two kinds of magnetic coupling mechanisms in transition metal doped Bi₂Se₃, Bi₂Te₃, and Sb₂Te₃. It is well known that in magnetically doped semiconductors or conventional dilute magnetic semiconductors (DMS), the neighboring magnetic dopants are aligned through the Ruderman-Kittel-Kasuya-Yoshida (RKKY) interaction [42, 43]. The Hamiltonian of RKKY model can be expressed by the following equation [44, 45]:

$$H_{12}^{RKKY} = \frac{i}{\pi} \int_{-\infty}^{E_F} dE \sum_{i \neq j} \text{Tr} \{ [-J(E) \vec{\sigma} \cdot \vec{S}_1] G(\vec{R}_{12}) [-J(E) \vec{\sigma} \cdot \vec{S}_2] G(-\vec{R}_{12}) \} \quad (1 - 4)$$

, where $J(E)$ is the exchange coupling coefficient, \vec{S}_1 and \vec{S}_2 are the spins of local magnetic ions, \vec{R}_{12} is the distance between the two localized ions, G stands for the Green's function, and $\vec{\sigma}$ is the Pauli matrix of itinerant electrons. The Hamiltonian can then be expressed into

$$H_{12}^{RKKY} = F_1(R, E_F) \vec{S}_1 \cdot \vec{S}_2 + F_2(R, E_F) (\vec{S}_1 \times \vec{S}_2)_y + F_3(R, E_F) S_1^y S_2^y \quad (1 - 5)$$

Which shows that the RKKY interaction consists of three terms: the Heisenberg-like term, the DM-like term, and the Ising-like term, displaying different range functions [44]. Unlike the RKKY interactions mediated by itinerant carriers, it was found that the magnetic exchange among local moments in magnetic TIs could also be mediated by band electrons, through the van Vleck mechanism. In 2010, R. Yu et al. predicted that tetradymite TI materials ($\text{Bi}_2\text{Se}_3/\text{Bi}_2\text{Te}_3/\text{Sb}_2\text{Te}_3$) could form such magnetic order from van Vleck mechanism when doped with Cr or Fe by first-principles calculations [19]. Later, C.Z Chang et al. carried out an experimental study to investigate the Van Vleck mechanism in magnetic TIs [39], where they found the ferromagnetism of the $\text{Cr}_{0.22}(\text{Bi}_x\text{Sb}_{1-x})_{1.78}\text{Te}_3$ films remained the same, regardless of the carrier type and density modulated by Bi to Sb ratio. In 2013, X. Kou et al. from UCLA reported the experimental evidence of the coexistence of both magnetisms in 6 QL Cr-doped topological insulators with the Cr doping levels of 2%, as shown in Fig. 1-4 [41]. Fig. 1-4 a shows the device structure with a top gate control, and Fig. 1-4 b shows the gate-dependent anomalous Hall. As shown in Fig. 1-4 c, the observed ambipolar effect of R_{xx} (red solid lines) indicates that the Fermi level can be effectively tuned across the surface band gap. The Hall density (blue) determined from the linear R_{xy} curve at high field changes sign accordingly.

Fig. 1-4 d shows the changes of coercivity field H_c at 1.9 K (red hollow circles) and Curie temperature T_c (blue solid squares) with applied top-gate voltages. Both gradually decrease when the sample is biased from p-type to n-type, indicating the hole-mediated RKKY interaction signature in this region (green region, $V_g < -1$ V). With the V_g further increases and E_F shifts into conduction band (yellow region, $V_g > -1$ V), H_c and T_c became saturated, indicating the existence of electric-field independent bulk van Vleck ferromagnetism.

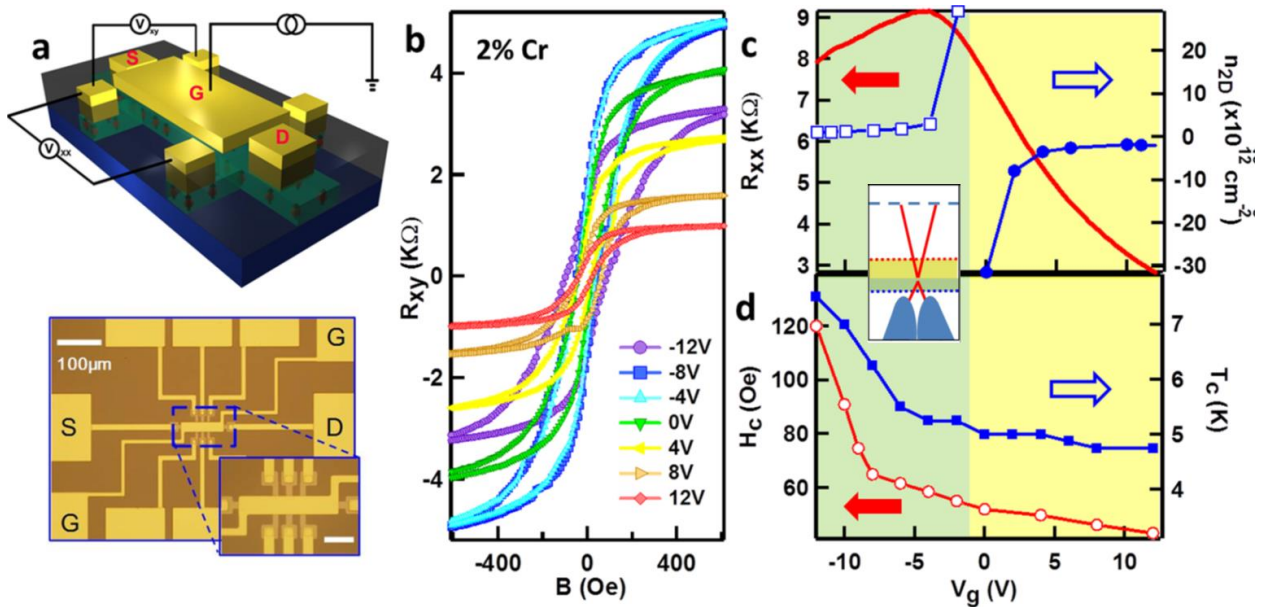


Figure 1- 4 Coexistence of hole-mediated RKKY and bulk van Vleck mechanisms revealed by electric-field-controlled anomalous Hall effect. (a) Top-gated Hall bar device structure. The effective size is $10 \mu\text{m}$ (L) by $40 \mu\text{m}$ (W). (b) Gate-dependent anomalous Hall effect at 1.9 K in 6 QL $\text{Cr}_{0.04}(\text{Bi}_{0.49}\text{Sb}_{0.49})_2\text{Te}_3$ thin films. (c) Top-gate modulations of R_{xx} and R_{xy} in the sample. (d) The changes of coercivity field H_c at 1.9 K (red hollow circles) and Curie temperature T_c (blue solid squares) with applied top-gate voltages. Adopted from Ref. [41].

1.3 Quantum anomalous Hall

The quantum anomalous Hall (QAH) effect is known as a “zero-field version” of quantum Hall effect, which can be viewed as spontaneous magnetization replacing the external magnetic field. It is characterized by a quantized Hall resistance $R_{xy} = e^2/h$ with vanishing longitudinal resistance at zero magnetic field. Unlike quantum Hall which is due to the Landau level and cyclotron orbit localization in two-dimensional electron gas (2DEG) under strong external magnetic field at low temperature [46], the quantum anomalous Hall (QAH) effect has a different physical origin arising due to the combination of topologically nontrivial band structures and ferromagnetism-induced TRS-breaking. For 3D TIs, the ferromagnetism from magnetic dopants can introduce an exchange field along the out-of-plane direction thus the Hamiltonian of the surface states can be written as [19]:

$$H = H_{SS} + H_{Zeeman} = \begin{bmatrix} m_k + gM & iv_F k_- & 0 & 0 \\ -iv_F k_+ & -m_k - gM & 0 & 0 \\ 0 & 0 & m_k - gM & -iv_F k_+ \\ 0 & 0 & iv_F k_- & -m_k + gM \end{bmatrix} \quad (1 - 6)$$

with the following basis: $|+\uparrow\rangle, |-\downarrow\rangle, |+\downarrow\rangle, |-\uparrow\rangle$, where $|\pm\uparrow\rangle = (|t\uparrow\rangle \pm |b\uparrow\rangle)/\sqrt{2}$, $|\pm\downarrow\rangle = (|t\downarrow\rangle \pm |b\downarrow\rangle)/\sqrt{2}$. Here t, b stands for top and bottom surface and \uparrow, \downarrow represent the spin up and spin down states. To achieve QAH effect, starting from either a topologically trivial semiconductor or TI, the surface band evolution when exchange field is introduced is shown in Fig. 1-5. If the system starts from a topological trivial case where subbands are not inverted as shown in Fig. 1-5 a, the exchange field can shift the bands with opposite spins and a pair of inverted subbands will appear (red dashed line and blue solid line) when the exchange field is strong enough. For TI system where the initial subbands are already inverted as shown in Fig. 1-5 b, the exchange field can release the band inversion in one pair of subbands (red solid line and

blue dashed line) and increase the band inversion in the other pair (red dashed line and blue solid line). In principle, QAH effect could occur in both cases. However, in practical, the route starting from TI (Fig. 1-5 b) is more feasible.

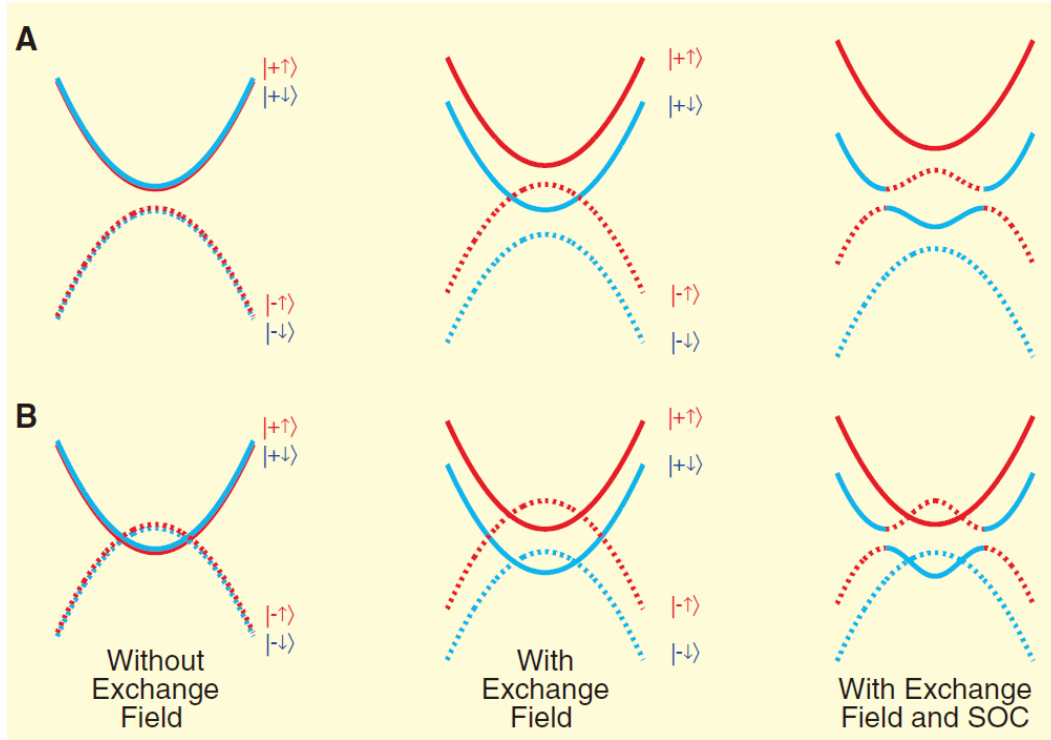


Figure 1- 5 Evolution of the subband structure upon increasing the exchange field. The solid lines denote the subbands that have even parity at Γ point, and dashed lines denote subbands with odd parity at Γ point. The blue color denotes the spin down electrons; red, spin up electrons. (a) The initial subbands are not inverted. When the exchange field is strong enough, a pair of inverted subbands appears (red dashed line and blue solid line). (b) The initial subbands are already inverted. The exchange field releases the band inversion in one pair of subbands (red solid line and blue dashed line) and increase the band inversion in the other pair (red dashed line and blue solid line). Adopted from Ref. [19].

In 2013, the QAH effect was first experimentally observed in magnetically Cr- doped

(Bi,Sb)₂Te₃ (Cr-BST) thin films by Chang et al. [47]. Five quintuple layer (QL) Cr_{0.15}(Bi_{0.1}Sb_{0.9})_{1.85}Te₃ thin films were grown on SrTiO₃ substrates, and by applying a back gate voltage through SrTiO₃, the Fermi level can be tuned into its bulk energy gap. As shown in Fig. 1-6, a quantized Hall resistivity ρ_{yx} of h/e^2 and a vanishing longitudinal resistivity ρ_{xx} ($\sim 0.098 h/e^2$) at zero magnetic field can be observed when the gate is at an optimized voltage of $V_g \sim -1.5$ V. The QAH state only happened at a very small back-gate voltage window around -1.5 V. As shown in Fig. 1-6 b and d, the ρ_{yx} , ρ_{xx} and the converted conductivity quickly deviated from the quantized value as its Fermi level tuned away by the gate voltage.

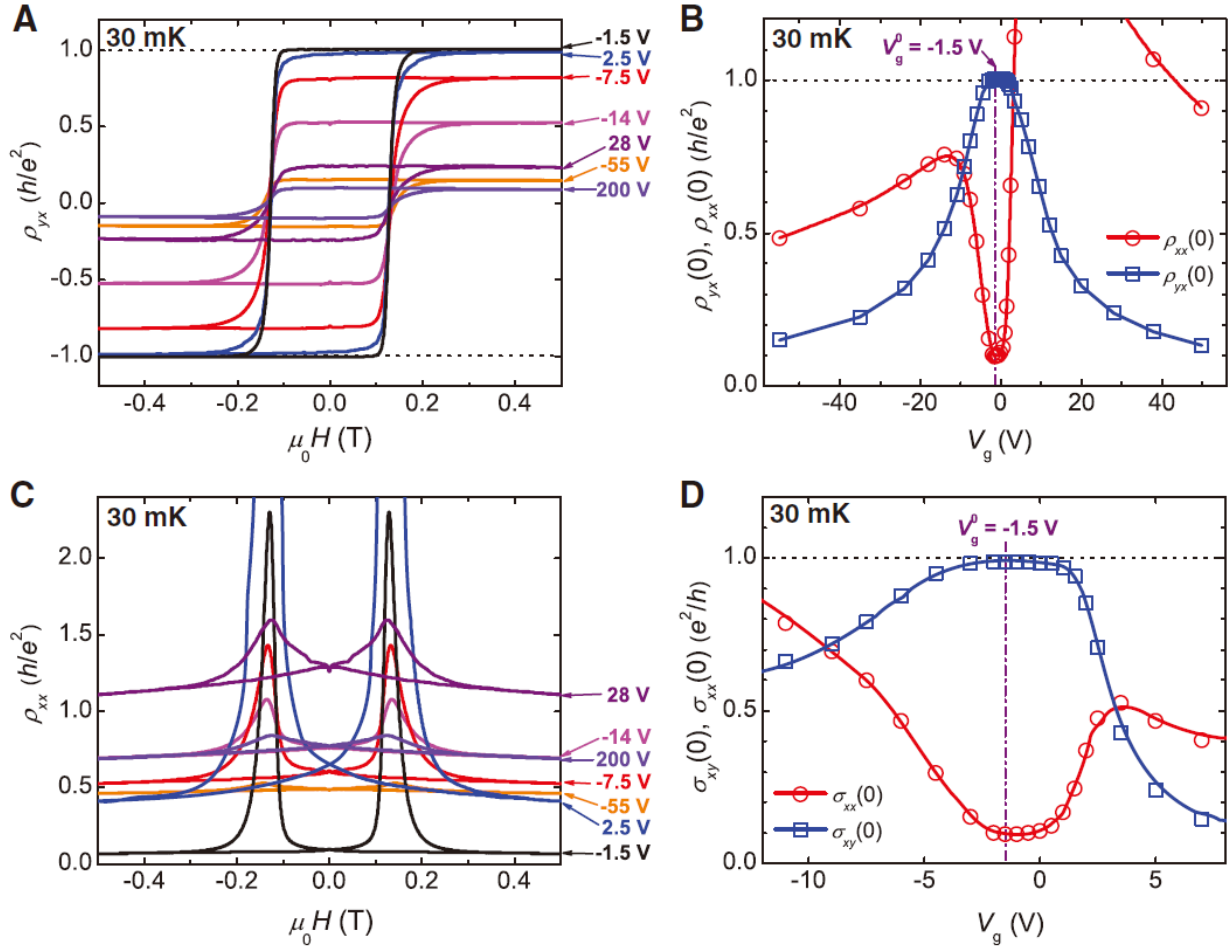


Figure 1- 6 The QAH effect in Cr-doped (Bi, Sb)₂Te₃. (a) Magnetic field dependence of ρ_{yx} at

different back-gate voltage. (b) Dependence of $\rho_{yx}(0)$ (empty blue squares) and $\rho_{xx}(0)$ (empty red circles) on V_g . (c) Magnetic field dependence of ρ_{xx} at different V_g . (d) Dependence of $\sigma_{xy}(0)$ (empty blue squares) and $\sigma_{xx}(0)$ (empty red circles) on V_g . Adopted from Ref. [47].

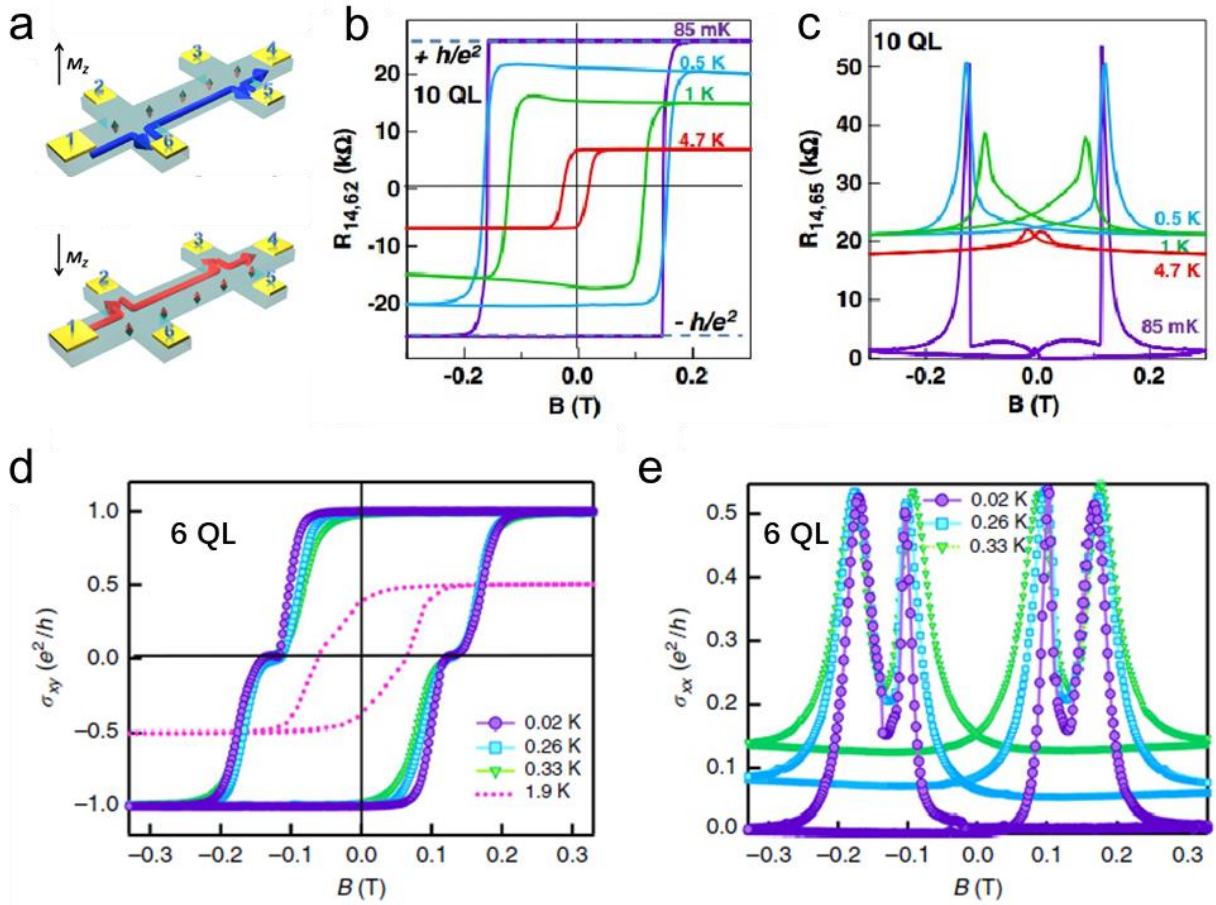


Figure 1-7 Scale-invariant QAH effect beyond 2D limit and metal-to-insulator transition in 6 QL Cr- (Bi, Sb)₂Te₃. (a) Schematics of the chiral edge conduction in the QAHE regime. (b) Hysteresis $R_{xy} - B$ curves of the 10 QL film at different temperatures. For $T < 85$ mK, R_{xy} attains the quantized value of h/e^2 . (c) Butterfly-shaped $R_{xx} - B$ curves of the 10 QL film. In the QAHE regime, R_{xx} nearly vanishes at low fields. Adopted from Ref. [48] (d) Magnetic field-dependent σ_{xy} at different temperatures. Zero Hall plateaus at $\pm H_C$ are developed between the two QAHE states up to 0.33 K. (e) Magnetic field-dependent σ_{xx} at different temperatures. Even when the

film already deviates from the perfect QAHE state at $T=0.33$ K, both the zero σ_{xy} plateaus and double-peaked σ_{xx} still persist. Adopted from Ref. [49].

Soon after the first discovery of QAH effect, X. Kou et al. from UCLA observed the QAH effect in 10 QL $\text{Cr}_{0.12}\text{Bi}_{0.26}\text{Sb}_{0.62}$ films showing that the QAH effect can persist even when the film thickness is beyond the two dimensional (2D) hybridization limit [48]. As shown in Figure 1- 7 b and c, the R_{xy} attains the quantized value of h/e^2 and R_{xx} nearly vanishes at low temperatures. The extension of the QAHE into the three-dimensional thickness region addresses the universality of this quantum transport phenomenon. Figure 1- 7 a show the schematics of the chiral edge conduction in QAHE regime under different magnetization. Later, X. Kou et al. further observed giant longitudinal resistance peaks and zero Hall conductance plateau at the coercive field in the 6 QL $\text{Cr}_{0.12}\text{Bi}_{0.26}\text{Sb}_{0.62}$ films, demonstrating the metal-to-insulator switching between two opposite QAHE plateaus [49]. As shown in Figure 1- 7 d and e, the high resistance insulator state, after conductivity matrix conversion, would result in a zero plateau in σ_{xy} and a four-peak behavior in σ_{xx} . The realization of this QAHE insulating state near coercivity unveils new ways to explore quantum phase-related physics and applications and is closely related the work that will be introduced in Chapter 3.

The exploration of materials systems that can host QAH effect aroused worldwide interest. In 2015, V- dopant was also shown to introduce robust ferromagnetism in $(\text{Bi,Sb})_2\text{Te}_3$ with perpendicular anisotropy (PMA) and QAH effect was observed in V-BST [50]. More recently, QAH effect was also observed in other material systems, such as intrinsic magnetic topological insulator MnBi_2Te_4 [51], twisted bilayer graphene [52], and $\text{MoTe}_2/\text{WSe}_2$ Moiré heterostructures [53].

1.4 Axion insulator

Axion, in high energy physics is a hypothetical elementary particle and is of interest as a possible as a building block of dark matter [54]. The axion has signatored axial electrodynamics, where the electric field and magnetic field are in parallel direction, defying the conventional Maxwell electrodynamics, in which electric field and magnetic field are orthogonal. It is intriguing to note that these ingenious structures give a possibility to study the counterpart of the physics of dark matter in solid states. The topological magnetoelectric (TME) effect, is a signature phenomenon derived from the axion electrodynamics, where the crossed induction of magnetization and electric polarization are expected to occur by applying external electric and magnetic fields, respectively [1, 55-57]. A theoretical proposal to achieve axion insulator state on 3D TI is shown Fig. 1-8 [1]. In the proposed structure, a cylindrical 3D TI is surrounded by a ferromagnetic material with magnetization in the radial direction. Due to the magnetic proximity effect, the 3D TI will become an axion insulator and host TME effect. Fig. 1-8 a and b illustrate the magnetization induced by an electric field, and charge polarization induced by a perpendicular magnetic field in the cylindrical structure, respectively.

However, the cylindrical structure is not practical to realize in experiments. A simplified sandwich structure, where two compositional different MTI layers with different coercivity are separated by an undoped TI layer, is also proposed to host the axion insulator state [1]. As shown in Fig. 1-8 c and d, the electric field E_x with direction into the paper would induce Hall currents j_t and j_b for parallel and antiparallel magnetizations, respectively. For the parallel case (Fig. 1-8 c), the sandwiched structure would be in a QAH state, while for the antiparallel case (Fig. 1-8 d), the system could form a circulating Hall current is neglecting un-gaped side surface, which is analogy to Fig. 1-8 a, representing the axion insulator state. With each surface contributing 1/2

e^2/h conductance, the QAH insulator would have a Hall conductance of e^2/h while axion insulator would have Hall conductance of 0, as two surfaces canceled each other. This makes the detection of axion insulator accessible through transport measurement.

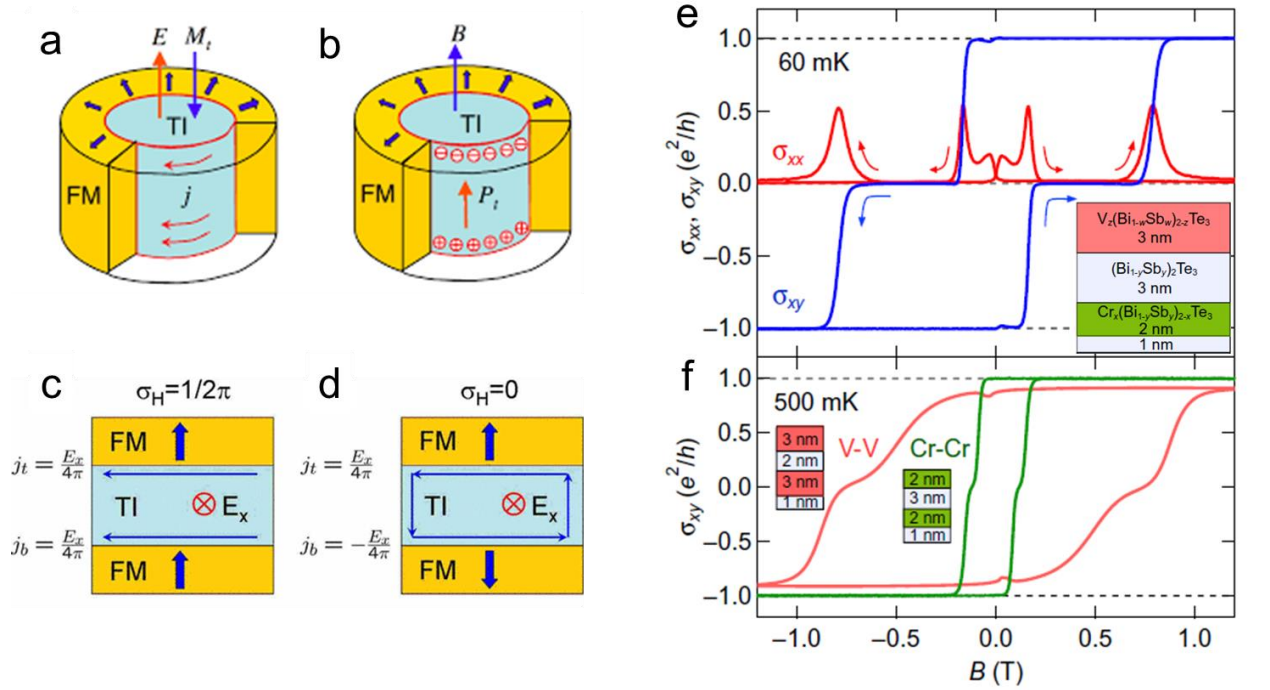


Figure 1- 8 Realization of axion insulator state. (a) Illustration of the magnetization induced by an electric field in a cylindrical geometry. (b) Illustration of the charge polarization induced by a perpendicular magnetic field in the same geometry. (c-d) The electric field E_x with direction into the paper and the induced Hall currents j_t and j_b for parallel and antiparallel magnetizations, respectively. In (d) the Hall currents on the two surfaces are opposite and form a circulating current. Adopted from Ref. [1]. (e) Magnetic field dependence of Hall conductivity (σ_{xy}) and longitudinal conductivity (σ_{xx}) of the MBE-grown TI (BST) film doped with Cr and V individually on top and bottom (inset) measured at 60 mK. (f) Magnetic field dependence of σ_{xy} at 500 mK in the Cr-Cr-doped (shown in green) and the V-V-doped (shown in red) bicolor TI heterostructures. Adopted from Ref. [58].

Followed by this proposal, the axion insulator state was first experimentally achieved in 2017 in asymmetrically doping Cr- and V- MTI sandwiched structures [58]. As shown in Fig. 1-8 e and f, the V-BST has a larger coercivity than Cr-BST, so the configuration in Fig. 1-8 d can be realized at certain magnetic field where top and bottom surface magnetization have the opposite directions. In the transport measurement, a signature zero Hall conductance plateau ($\sigma_{xy} = 0$), as the direct evidence of axion insulator state, was observed in Cr-BST/ BST/ V-BST sandwiched structures (Fig. 1-8 e), while absent in symmetrically doped Cr-BST/ BST/ Cr-BST or V-BST/ BST/ V-BST (Fig. 1-8 f).

1.5 Organization

In this Dissertation, we summarize our work on the emerging topological quantum states that can be hosted in TI and MTI. The contents are arranged as follows. In Chapter 2, we show the molecular beam epitaxy growth of TI and MTI, and the recipe development to achieve QAH effect in MTI. The challenges to realized QAH effect and effort to transfer QAH insulator growth recipe on various substrates will be discussed. In Chapter 3, we focus on the QAH effect on MTI and axion insulator state in MTI sandwiched structures. The similarity and difference of the two states will be discussed. In Chapter 4, we focus on the QAH insulator and antiferromagnetic heterostructures. We observed an exchange biased QAH effect resulted from the interfacial exchange coupling results, and a field training process as an effective method to manipulate the QAH state will be discussed. In Chapter 5, we focus on the QAH insulator and superconductor heterostructures which was believed to host chiral Majorana edge mode. To understand recent debate on the experimental observations, both superconductor and control experimental normal metal hybrid devices are fabricated and measured. The important role of

interface details will be discussed. In Chapter 6, two collaborative works will be introduced. Aiming to understand and address the inter-channel scattering in QAH, the size dependence on mesoscopic devices is studied. Enabled by the successful growth of QAH insulator on mica, an electric field induced topological phase transition was observed in dual-gate devices, fabricated by exfoliation and transfer techniques. Chapter 7 is the conclusion chapter of this dissertation.

Chapter 2 Molecular Beam Epitaxy Growth of Topological Insulators

In this dissertation, all TI and MTI films were grown in an ultrahigh vacuum Perkin Elmer MBE system at the Device Research Laboratory of UCLA. The in-situ reflection high-energy electron diffraction (RHEED), atomic force microscopy (AFM), X-ray diffraction (XRD), and transmission electron microscopy (TEM) were used to characterize the film surface morphology and crystal quality. Cryogenic magneto-transport measurement was carried out to characterize the film magnetic property and study quantum transport behavior. In this chapter, most of the tools will be described, and the process development to realize QAH effect will be discussed in detail.

2.1 Molecular beam epitaxy

Molecular beam epitaxy is a popular thin-film epitaxy technique which has several unique advantages. It can realize good crystalline growth, maintain a low impurity level, and has precise control over thickness and doping levels.

All TI and MTI films are grown in an ultrahigh vacuum Perkin Elmer MBE system at the Device Research Laboratory of UCLA with a base pressure as low as 10^{-10} Torr. The system consists of three vacuum stages: first, sample is loaded into the system through a load-lock with pressure $\sim 10^{-5}$ Torr maintained by a turbomolecular pump; then, sample was transferred through a transfer tube with pressure $\sim 10^{-8}$ Torr maintained by an ion pump, and finally sample is loaded into the growth chamber (shown in Fig. 2-1 a) with pressure $\sim 10^{-10}$ Torr maintained by a cryo-pump and an ion pump. The growth chamber is equipped with 8 effusion cells and enabling the

growth of Bi, Sb, Te, Se, Mn, Cr, Fe, Sn, where the Sb and Se cells are especially designed with high-temperature crackers to achieve monomeric element flux. In addition, an e-gun evaporator is integrated into the system, which enables the growth of low vapor pressure materials that requires high evaporation temperature. It can evaporate W, Mo, Nb, and V by using high power electron beam heating the source above 1300°C, which is beyond the limit of conventional Knudsen cells.

The system is also equipped with in-situ process monitoring tools. The ionization gauge inside the chamber can measure the total pressure, and a residual gas analyzer (RGA) can provide accurate residual gases' mass spectrum, which may also serve as a leak detector by monitoring helium partial pressure when flushing ultra-high purity helium gas outside the chamber through possible leakage spots. An in-situ reflective higher-energy electron diffraction (RHEED) is also equipped in the system, which can provide with the real-time crystal growth information on the surface.

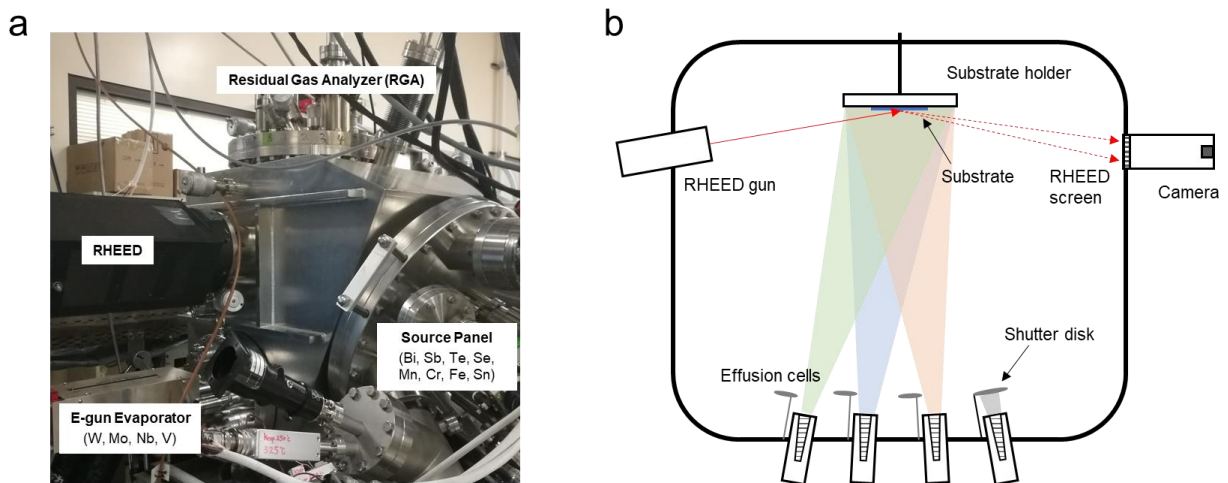


Figure 2- 1 MBE system in Device Research Lab at UCLA. (a) The system is equipped with 8 Knudsen cells and 1 e-gun evaporator with 4 crucibles, making it capable of growing 12 elements including Bi, Sb, Te, Se, Cr, Fe, Sn, Mn, W, Nb, Mo and V. This system is equipped

with *in-situ* RHEED, RGA. (b) Schematic drawing of the MBE setup.

Fig. 2-1 b shows the schematic drawing of the setup inside the chamber. During the growth, pneumatic shutters can be controlled to allow the molecular beam we would like to grow. The flux of each element is precisely controlled by its crucible temperature heated by either tungsten filaments (effusion cells) or high-power electron beams (e-beam evaporator). The substrate holder is heated by radiation heating of tantalum filaments on its back and can be precisely controlled ($\pm 0.1^\circ\text{C}$) by the computer software. The substrate holder can also rotate in its surface plane, allowing the film growth with better uniformity. During the growth, high energy electron beams ($>8\text{keV}$) will be emitted from the RHEED gun, and shotted on to the substrate in a grazing angle ($<5^\circ$). The reflected and diffracted electrons are then collected and imaged by a phosphor screen and CCD camera developed by KSA Associates.

RHEED is a powerful tool for real-time characterization of epitaxial growth, due to its surface sensitivity and small electron wavelength. For example, 8keV electron energy corresponds to a wavelength around 0.14 \AA which is sufficient to resolve crystal details down to atomic scale. The interaction of grazing angle incident electrons and surface crystal lattice and be expressed by the Laue diffraction condition:

$$\mathbf{k}_{out} - \mathbf{k}_{in} = \mathbf{G} \quad (2 - 1)$$

where \mathbf{k}_{in} and \mathbf{k}_{out} are the wavevectors of incident and diffracted e-beams, and \mathbf{G} is the reciprocal lattice vector of the surface. As an example, the reciprocal lattice vector of an ideal infinite two-dimensional rectangular lattice is an infinite array of rods spaced by $(\frac{2\pi m}{a}, \frac{2\pi n}{b})$ where \mathbf{a} and \mathbf{b} are the real space lattice constant and m, n are integers. A common method to construct the RHEED pattern is using an Ewald sphere, as shown in Fig. 2-2 a. The Ewald sphere is constructed using the incident beam's wavevector as the radius, and the intersection of the

surface reciprocal lattice rods and the Ewald sphere will fulfill the Laue condition and results in the diffraction pattern on the screen, as shown in Fig. 2-2 b.

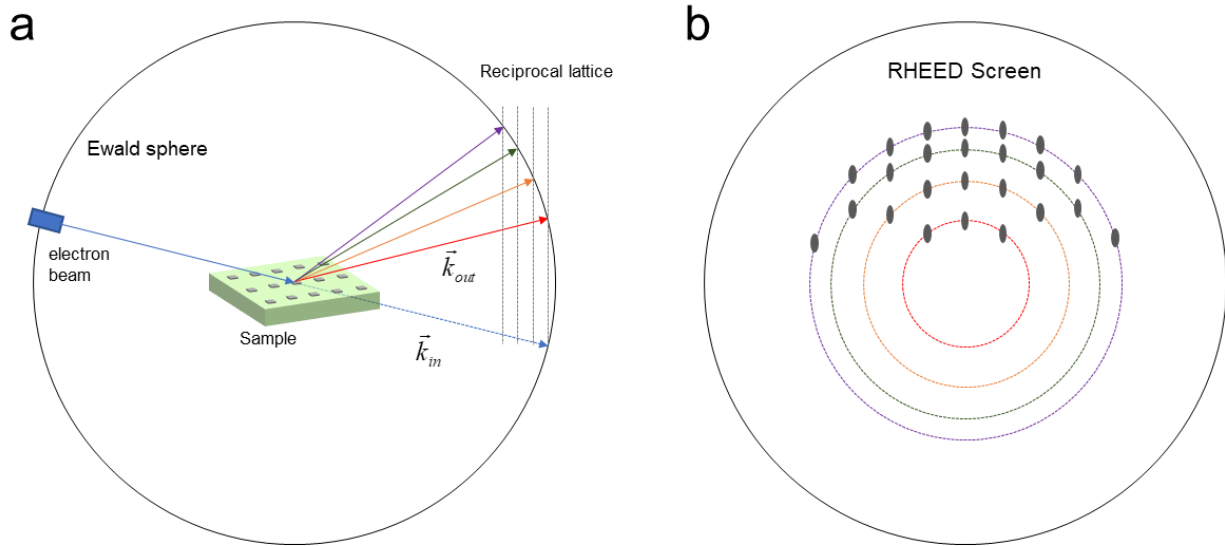


Figure 2- 2 Schematic of RHEED pattern formation. (a) Ewald sphere for the construction of RHEED pattern. The allowed diffraction beam must satisfy the condition $k_{out} - k_{in} = G$ which is the crystal's reciprocal lattice vector. (b) The RHEED pattern of an ideal 2D crystalline surface.

Fig. 2-3 shows the RHEED patterns of some typical surface crystal conditions . For a flat and infinite single crystalline surface (Fig. 2-3 a), its lattice vector in reciprocal space is an infinite array of rods and results in spots on the RHEED pattern. However, some finite size domains will usually appear on the surface (Fig. 2-3 b), so its reciprocal lattice rods will have finite radius, resulting in streaks on the RHEED pattern. Similarly, when the surface has multilevel steps or even 3D islands, the RHEED pattern will becomes modulated streaks or 3D spots (Fig. 2-3 c and d). When the crystal growth is in a lay-by-layer mode, RHEED can provide important growth rate information as indicated by an oscillation in its intensity, as shown in Fig. 2-3 e. In a layer-by-layer growth mode, the surface undergoes a serial of islands nucleation and expansion, and finally forms a new layer. During this process, there will also be a periodically

evolution of the surface roughness. The roughness increase as the islands nucleates and expands before it reached 50% coverage (1 to 3), and then decreased when it's gradually forming a 100% covered new layer (3 to 5). The RHEED spot intensity will also oscillated accordingly with the surface roughness, providing an accurate growth period information. The TI and MTIs in $(\text{Bi,Sb})_2\text{Te}_3$ family usually show this layer-by-layer growth mode, so this techniques plays an important role in our later analysis.

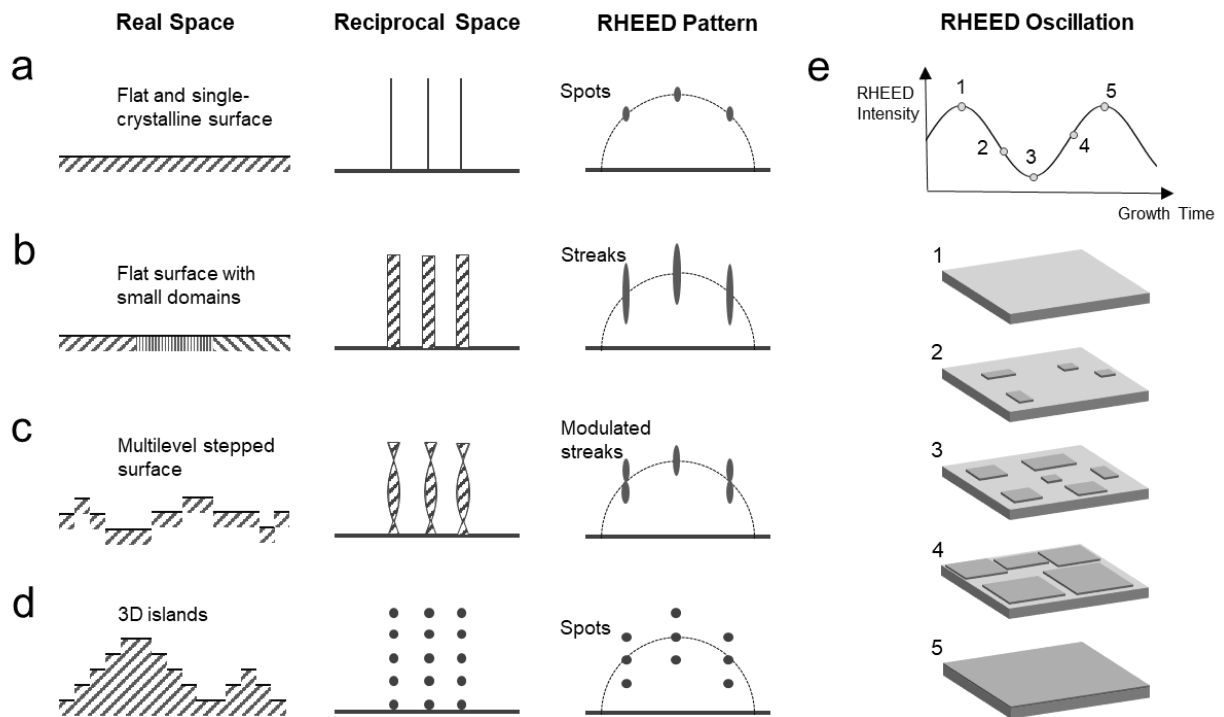


Figure 2- 3 RHEED patterns of some typical surfaces. The schematics of real space, reciprocal space, and RHEED pattern of (a) a flat and single-crystalline surface, (b) a flat surface with small domains, (c) multilevel stepped surfaces, and (d) 3D islands. (e) RHEED intensity oscillation during layer-by-layer growth mode, where smooth full-covered surfaces result in brighter patterns while rough partial-covered surfaces result in darker patterns.

2.2 MBE growth of TI and MTI

Since the theoretical proposal of topological insulators, various material systems have been explored including HgTe/ CdTe quantum well [5, 6], InAs/ GaSb bilayers [59], BiSb alloys [10, 11], and Bi_2Te_3 base compounds [12, 13, 60]. Among all the materials, the Bi_2Te_3 based tetradymite-type 3D TI is the most studied material system, due to its stable phase and readily mature growth method. This TI material family includes Bi_2Se_3 , Bi_2Te_3 , Sb_2Te_3 and the compound $(\text{Bi,Sb})_2\text{Te}_3$ (BST) which the addition degree of freedom to tune the fermi level by tuning Bi to Sb ratio. The TI and MTI materials in this dissertation will be focusing on this material family.

The crystal structure of the Bi_2Te_3 TI family is shown in Fig. 2-4. It has a layered structure, with each layer consists of five atomic layers so it's also known as quintuple layer (QL). Within each QL, the five atomic layers stacks in the order of Te-Bi-Te-Bi-Te and forms the covalent bonds, while between QLs, the two Te atomic layers are weakly coupled through Van der Waals force. The Bi_2Te_3 TI family has a rhombohedral crystal structure and shows a hexagonal symmetry in the (0001) plane. In this representation, the Bi_2Te_3 has a crystal lattice of $a=4.38 \text{ \AA}$ in the (0001) plane, and $c=30.49 \text{ \AA}$ along the c-axis where one QL has a thickness around 1 nm, and one unit cell consists of three QLs. The layered structural property of Bi_2Te_3 TI family makes them to form a layer-by-layer Van der Waals growth mode. This makes it possible to grow Bi_2Te_3 on various substrates with high tolerance of lattice mismatch [61] and enables precise thickness control down to one single QL by RHEED oscillations. To achieve epitaxial growth, we choose either (111) surface of diamond/ zinc blende structure or (0001) surface of hexagonal substrates. Therefore, the substrates we chose are GaAs (111) B, Si (111), $\alpha\text{-Al}_2\text{O}_3$ (0001) and mica.

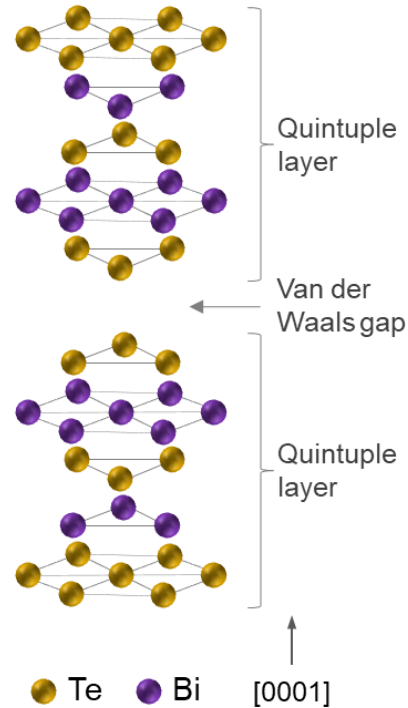

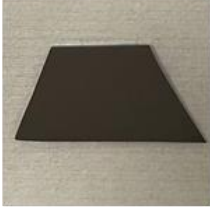





Figure 2- 4 Crystal structure of Bi_2Te_3 TI family.

The growth procedures of TI and MTI on various substrates are summarized in Table 2-1. To start with, some necessary substrates treatments outside the vacuum are needed to get a clean surface. Then, the clean substrates will be mounted onto the molybdenum-made substrate holder using indium glue at elevated temperature ($\sim 200\text{ }^\circ\text{C}$). This could provide a superior thermal contact between substrates and the holder, which ensures a fast temperature response and uniform temperature distribution. For some special applications that required low temperature process, In-Ga alloy may also be used since it's liquid form at room temperature. Then the substrate holder is transferred into the MBE chamber. Before the growth of TI, the thermal degassing of substrates is also needed to remove its surface contamination or native oxide. For example, the GaAs substrate needs a pre-annealing up to $580\text{ }^\circ\text{C}$ in Te rich environment, to remove its native oxide and induce surface reconstruction. Finally, the substrate was kept

between 160 °C and 230 °C, and Bi, Sb, and Te are co-evaporated for the growth of BST. For MTI growth, Cr was also co-evaporated to introduce magnetic doping.

Table 2-1 MBE growth procedure of TI and MTI on different substrates

GaAs (111)	Si (111)	α -Al ₂ O ₃ (0001)	mica
 <ul style="list-style-type: none"> Epi ready quality, no pretreatment 	 <ul style="list-style-type: none"> 1% HF clean until surface becomes hydrophobic 	 <ul style="list-style-type: none"> Ultrasonic clean in acetone, isopropyl alcohol (IPA) 	 <ul style="list-style-type: none"> Peel off top layer to get a clean surface
		<ul style="list-style-type: none"> Glue substrate onto holder using Indium or In-Ga alloy Transfer substrate holder into MBE chamber 	
<ul style="list-style-type: none"> 600 °C degas under Te flux until streaky GaAs RHEED pattern appear 	<ul style="list-style-type: none"> 700 °C degas until 7x7 surface reconstruction RHEED pattern appear 	<ul style="list-style-type: none"> Degas at 700 °C for 30 minutes 	<ul style="list-style-type: none"> Degas at 400 °C for 30 minutes
<p style="text-align: center;">Fix substrate temperature between 160 °C and 230 °C Co-evaporate Bi, Sb, Te, and Cr to grow Cr-BST</p>			

Especially, GaAs (111) B and α -Al₂O₃ (0001) are the most used substrates for TI and MTI growth. GaAs (111) B has a lattice constant of a=4 Å in the hexagonal representative, whose lattice mismatch is below 10% with BST. As shown in Fig. 2-5 a, the GaAs (111) B after pre-annealing shows a streaky RHEED patterns with shining Kikuchi lines. During the growth, the RHEED pattern of GaAs (111) B quickly evolves into the Cr-BST RHEED pattern as shown

in Fig. 2-5 b. The d-spacing between the first order RHEED lines is in inverse proportional to crystal lattice constant, and it shows that the d-spacing of Cr-BST is smaller than GaAs (111) B, which is consistent with a larger lattice constant of Cr-BST. Fig 2-5 c shows the AFM of a 6nm thick Cr-BST film, which shows a flat surface with roughness around only one QL.

One key factor affecting the Cr-BST growth quality is the GaAs (111) B pre-annealing process. During this process, Te molecular beam will be supplied to suppress the unwanted As atom escaping. An over-anneal issue may occur, where escaped As atoms leave pits on the substrates, due to insufficient Te flux, exceeding anneal temperature, or exceeding anneal time. The RHEED pattern of an over-annealed GaAs (111) B (Fig. 2-5 d) no longer show shining Kikuchi lines, and the Cr-BST tends to form 3D island growth indicated by 3D dots on the RHEED pattern as shown in Fig. 2-5 e. This issue can also be resolved by AFM. As shown in Fig. 2-5 f, the AFM image of as-grown 6nm thick Cr-BST film shows several pits, and a linecut indicates that the pits are as deep as 16 nm. For the MTI growth on α -Al₂O₃ (0001), it's free from this issue. The streaky RHEED patterns and a clear RHEED intensity oscillation in Fig. 2-5 g shows a high-quality layered growth. The XRD of as-grown Cr-BST films (Fig. 2-5 h) shows a good single crystal structure with the characteristic peaks in good agreement with previous reports [62].

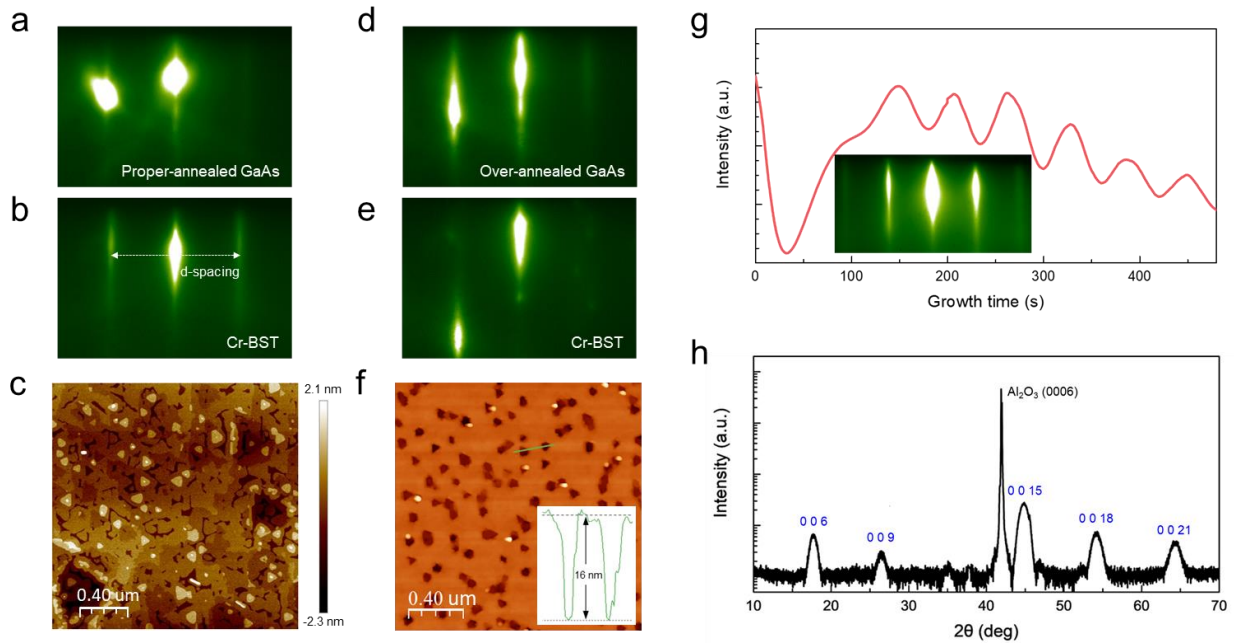


Figure 2- 5 Characterization of MTI growth. RHEED pattern of (a) properly-annealed GaAs (111) B substrates and (b) as-grown Cr-BST. (c) Its AFM image shows a flat surface with roughness only one single QL. RHEED pattern of (d) over-annealed GaAs (111) B substrates and (e) as-grown Cr-BST shows extra 3D growth patterns. (f) Its AFM image shows dense pits on the of the over-annealed GaAs substrates. (g) RHEED pattern, RHEED intensity oscillation and (h) XRD of MTI growth on the sapphire substrate.

2.3 Cryogenic magneto-transport measurement

The electrical and magnetic property of Cr-BST is characterized by cryogenic magneto-transport measurement. The measurements were conducted in a Quantum Design Physical Property Measurement System (PPMS) at UCLA. As shown in Fig. 2-6, the system consists of a liquid Helium Dewar, a He reliquifier for recycling evaporated He gas, a He gas cylinder, magnet and temperature controllers, and some external electrical measurement tools. The PPMS

system can apply a maximum magnetic field of 14 Tesla, and can reach a temperature range from 400 K down to 1.9 K. The PPMS system can also incorporate a dilution fridge unit, which has a separate loop of diluted He_3 and He_4 mixture. The dilution fridge insert can be directly inserted into the PPMS sample chamber and utilize the cooling power of PPMS to condense mixture. The sample loaded in the dilution insert can reach a base temperature as low as 50mK.

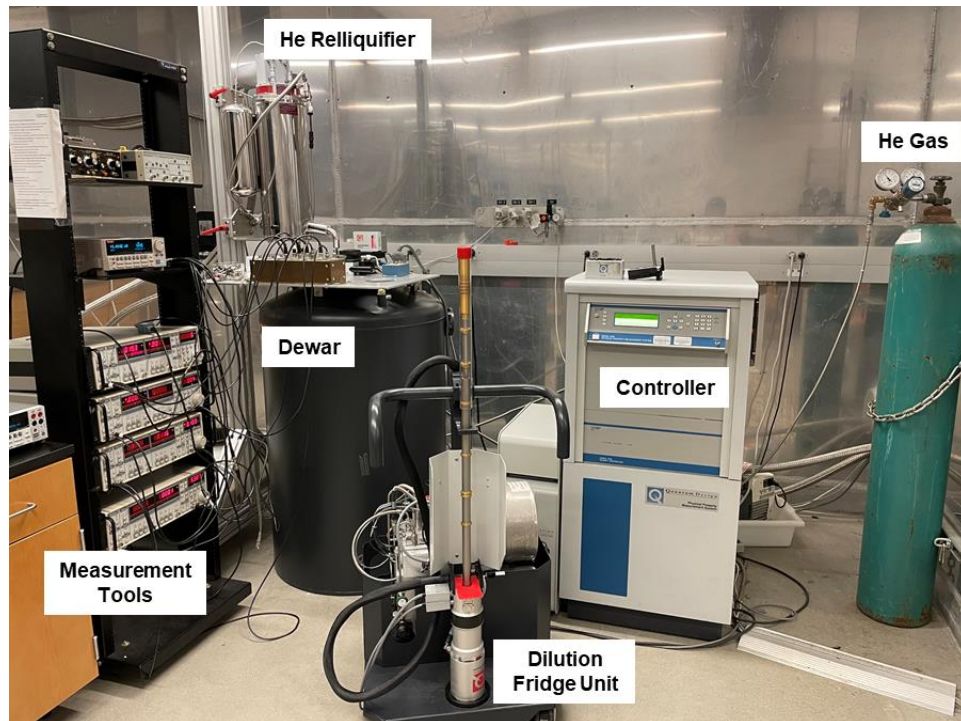


Figure 2- 6 PPMS system with and dilution fridge unit in Device Research Lab at UCLA.

The samples were patterned into millimeter size Hall bar devices ($L= 1$ mm, $W= 0.5$ mm) for magneto-transport measurement, by using a hard mask and dry etch method. The schematic of the Hall bar transport measurement setup is shown in Fig. 2-7. A low-frequency ($<100\text{Hz}$) AC current is applied into the source and drain channel (port 1, 4), and the longitudinal voltage V_{xx} (port 2, 3) and Hall voltage V_{xy} (port 6, 2) were measured by lock-in amplifiers.

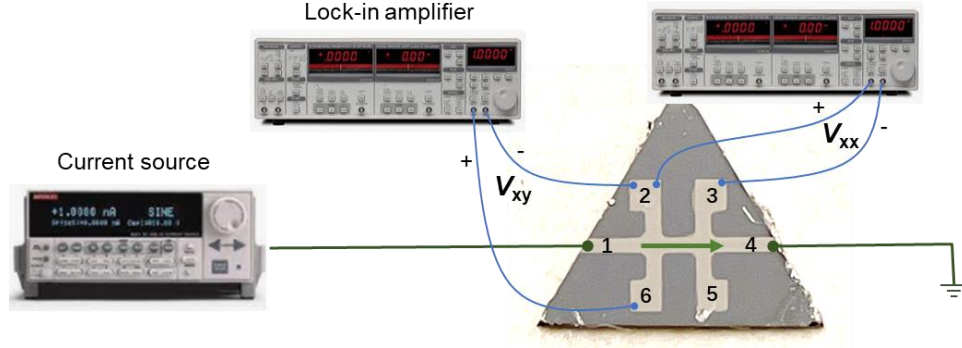


Figure 2- 7 Schematic of the Hall bar transport measurement setup.

The longitudinal sheet resistance and Hall resistance can be expressed by:

$$\rho_{xx} = \frac{V_{xx} W}{I L}, \quad \rho_{xy} = \frac{V_{xy}}{I} \quad (2 - 2)$$

and the conductivity after can be obtained from matrix conversion:

$$\sigma_{xx} = \frac{\rho_{xx}}{\rho_{xx}^2 + \rho_{xy}^2}, \quad \sigma_{xy} = \frac{\rho_{xy}}{\rho_{xx}^2 + \rho_{xy}^2} \quad (2 - 3)$$

In Eq. 2-3, ρ_{xx} , ρ_{xy} are in the unite of one resistance quanta $h/e^2 = 25812 \Omega$, and σ_{xx} , σ_{xy} are in the unit of one conductance quanta e^2/h . The measurements of interest are the dependence of ρ_{xx} and ρ_{xy} with temperature and magnetic field. The carrier density and mobility information could be directly extracted from ρ_{xx} and ρ_{xy} versus perpendicular magnetic field sweep. In some magnetic materials, when the temperature is below its magnetic critical temperature, the Hall resistance versus magnetic field will also presents an additional anomalous Hall effect (AHE) in addition to the linear ordinary Hall response. The AHE will result in an anomalous Hall resistance proportional to the perpendicular components of its magnetism, so the total Hall resistance can be expressed as:

$$\rho_{xy} = R_o B_z + R_A M_z \quad (2 - 4)$$

As a result, after extracting the linear ordinary Hall resistance or when the AHE contribution is dominant, the ρ_{xy} will effectively represents the perpendicular magnetization of the material. Some magnetic information such as Curie temperature T_c and coercivity field H_c can be easily known from the Hall bar transport measurement. One thing needs to be noticed is that, in the quantum anomalous Hall scenario that will extensively discussed in this dissertation, the quantized Hall resistance doesn't mean all material has a universal M_s along perpendicular direction. Instead, it is defined by the Chern number which arises out of topological properties of the material band structure. In QAH regime, the chiral edge quantum transport can be described by Landauer Büttiker formalism, which is also known as the scattering method for coherent transport. It can be expressed as:

$$I_i = \frac{e^2}{h} \sum_j (T_{ji}V_i - T_{ij}V_j) \quad (2 - 5)$$

where I_i is the current flowing from i^{th} contact into the sample, V_i is the voltage potential on the i^{th} contact, and T_{ij} represents the transmission probability from the i^{th} contact to the j^{th} contact.

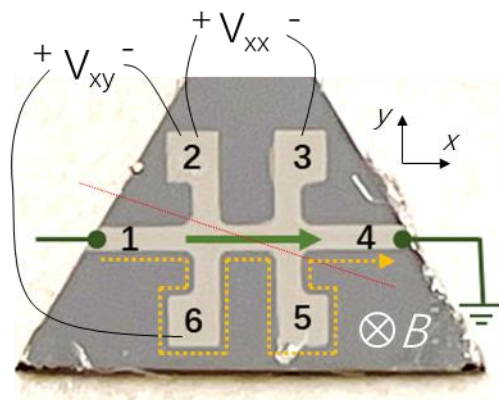


Figure 2- 8 Landauer Büttiker formalism on a Hall bar device.

Taking a Hall bar device as example, as shown in Fig. 2-8. It is straightforward to have $V_1 = V$, $V_4 = 0$, $I_2 = I_3 = I_5 = I_6 = 0$. Then considering the film was magnetized along -z direction, due to the chiral property of its edge state (shown in dashed yellow lines), we can get $T_{61} = T_{56} = T_{45} = 1$. As a result, we can get the voltage for all the pods as $V_1 = V_6 = V_5 = I(h/e^2)$ and $V_2 = V_3 = V_4 = 0$. Consequently, from the Hall bar measurement we will get R_{xy} equal to one resistance quanta and R_{xx} vanishing to zero.

2.4 Recipe development for QAH

In this section, the recipe development of Cr-BST for realization of quantum anomalous Hall effect will be discussed, where transport measurement will serve as an important feed back to the growth. We will stick to semi-insulating GaAs (111) B substrate for the recipe development, because its treatment method before growth is well-established and high-quality MTI growth can usually be achieved. In order to achieve QAH, high quality growth of single crystalline Cr-BST is a prerequisite, which can be determined by streaky RHEED patterns without any 3D dots similar to Fig. 2-5 b. The QAH effect is usually observed in a limited thickness range from 5nm to 10nm [48], so we need to precisely control the film thickness to be 6QL (~6nm) because it a higher possibility to observe QAH [63].

After a high quality 6QL TI and MTI growth can be achieved, the Bi to Sb ratio need to be proper adjusted so that the fermi level can locates in its bulk energy gap and near its Dirac point. Fig. 2-9 a shows the schematics of the position of E_F and Dirac point with different Bi to Sb ratio, ranging from pure Bi_2Te_3 to pure Sb_2Te_3 . For Bi_2Te_3 its E_F is buried in the bulk conduction band while Dirac point locates at the top of bulk valence band. With the increasing of

Sb concentration, the E_F gradually moves towards its valence band while the Dirac point moves up towards conduction band. This can be shown by a change from metallic behavior to semiconducting behavior and then back into metallic behavior with the increase of Sb concentration, as shown in Fig. 2-9 b. At certain range, E_F and Dirac point are close to each other and both locate within the bulk energy gap. At this range, the sample will have a highest resistivity as well as a lower carrier density as shown in Fig. 2-9 c.

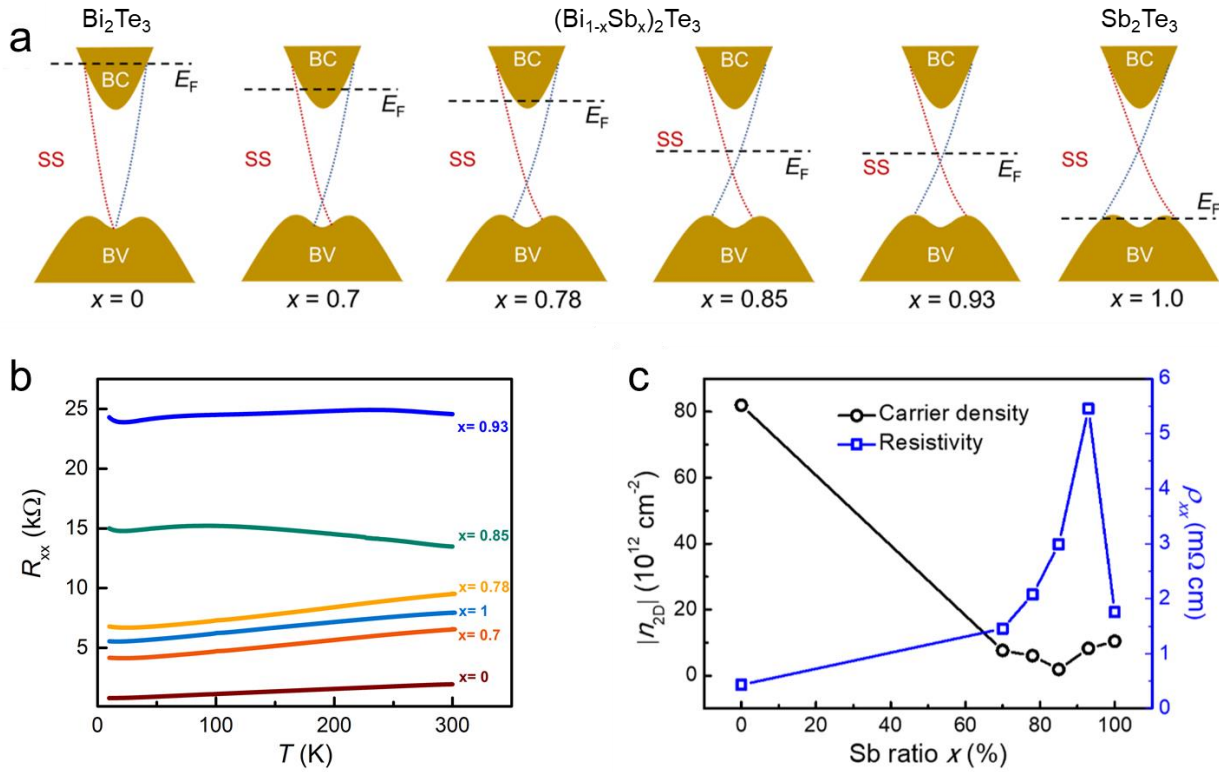


Figure 2- 9 Fermi level tuning by varying Bi to Sb ration. (a) Schematic of the Fermi level positions for different Sb ratios ($x = 0, 0.7, 0.78, 0.85, 0.93, 1.0$) of $(\text{Bi}_{1-x}\text{Sb}_x)_2\text{Te}_3$, which are estimated from the two-dimensional (2D) carrier density $|n_{2D}|$ and resistivity ρ_{xx} . (b) Temperature dependences of longitudinal resistance of the $(\text{Bi}_{1-x}\text{Sb}_x)_2\text{Te}_3$ with different compositions. (c) $|n_{2D}|$ and ρ_{xx} as a function of Sb ratios in $(\text{Bi}_{1-x}\text{Sb}_x)_2\text{Te}_3$.

After the rough optimization of Bi to Sb ratio, the Cr magnetic dopants are introduced introduce by co-evaporation, and its doping level needs to be tuned. The Cr concentration needs to be strong enough to introduce robust ferromagnetism and break the time-reversal-symmetry. On the contrary, too high Cr doping is not preferred as the Cr substitution of Bi and Sb will weaken the spin orbit coupling and likely destroy its topology. Fig 2-10 a show the Hall resistance hysteresis of samples with different Cr doping levels measured at 10 K. higher Cr doping can result in higher coercivity field and better perpendicular magnetic anisotropy (PMA). The Bi to Sb ratio and Cr doping concentration need to be further fine-tuned to achieve QAH quality film.

Even though all these conditions are optimized, the observation temperature of QAH effect is usually limited to sub-Kelvin range and requires dilution refrigerator to measure it, which is almost two orders of magnitude smaller than its ferromagnetic ordering temperature (~30K). Extensive effort in the community has been focused on understanding this discrepancy and enhancing the observation temperature of QAH effect. It is proposed that the low observation temperature of QAH effect might be due to its bulk conduction channel from valence band top [64, 65], and the non-uniform surface exchange gap of inhomogeneous Cr-doping [64]. Instead of growing 6 QL uniform doping MTI, modulation doping strategy can be applied to improve the sample quantization temperature [64, 66]. By increasing Cr doping level at surface to enhance surface exchange gap and reducing Cr doping level in the bulk layers to suppress bulk conduction through in-gap dopant energy state, the observation temperature of QAH effect can be slightly enhanced. Here, in addition to the Cr modulation doping, the Bi to Sb ratio of surface layer and bulk layers was also optimized individually.

Then the films were patterned into Hall bar devices and measured in PPMS. QAH films have some typical transport behaviors about 2K that can be easily distinguished from regular MTI films. During the field cooling from 300 K to 2K, the longitudinal resistance will behave as a semiconductor at higher temperature but become metallic at low temperature below its TC, due to the emergence of edge channel conduction (Fig. 2-10 b). The Hall resistance will be approaching the quantized value of one resistance quanta $h/e^2 = 25.812 \text{ k}\Omega$ as shown in Fig. 2-10 c where ρ_{xy} is almost 97% quantized at 2 K. If the sample was further cooled down to sub-Kelvin temperature, its ρ_{xx} will continue drops to zero and ρ_{xy} will quantized to h/e^2 , which is the QAH effect. The magneto-transport results in the quantized region will be discussed in more details in the rest of this dissertation.

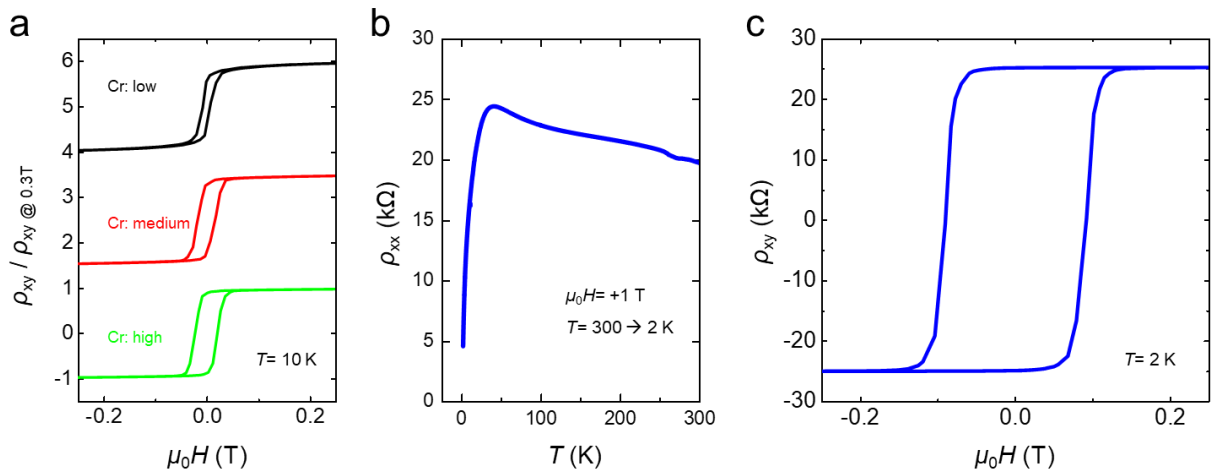


Figure 2- 10 Magnetic tuning by Cr doping. (a) the Hall resistance hysteresis of samples with different Cr doping levels at 10 K. (b) The longitudinal resistance versus temperature under +1T magnetic field and (c) Hall resistance versus magnetic field sweep at 2K of a proper optimized QAH quality sample.

2.6 Summary of chapter 2

In this chapter, we introduced the fundamentals of MBE and its in-situ RHEED characterization technique. The epitaxy of Bi_2Te_3 family TI materials on four different substrates are described. The unique layered structure of Bi_2Te_3 family enables a layer-by-layer Van der Waals epitaxy mode, making it possible to achieve high quality film on various substrates with high tolerance of lattice mismatch. We have also introduced the cryogenic magneto-transport measurement techniques such as PPMS and DR unit. The magneto-transport results of Hall bar devices will serve as important feedback for QAH recipe development. The QAH film can be achieved after fine-tuning of Bi to Sb ratio and Cr doping concentration, which has a signature of metallic longitudinal resistance and large Hall resistance at low temperature.

Chapter 3 Quantum anomalous Hall (QAH) effect and axion insulator

The quantum anomalous Hall (QAH) effect arises due to the combination of topologically nontrivial band structures and ferromagnetism-induced time-reversal symmetry breaking. Characterized by a quantized Hall resistance with vanishing longitudinal resistance at zero magnetic field, it was first observed experimentally in magnetically doped topological insulator (MTI) thin films, Cr- and V- doped $(\text{Bi,Sb})_2\text{Te}_3$ [47-50, 66, 67], and more recently observed in the intrinsic magnetic topological material MnBi_2Te_4 [51], twisted bilayer graphene [52], and $\text{MoTe}_2/\text{WSe}_2$ Moiré heterostructures [53]. Because of the dissipation-less edge conduction property, QAH insulator is a promising platform to design novel quantum devices, and it has a unique advantage over quantum Hall (QH) systems which require a large external magnetic field to drive two-dimensional electron gases into Landau quantization.

The axion insulator is another exotic topological phase that can be hosted in MTI. The axion has signatored axial electrodynamics, where the electric field and magnetic field are in parallel direction, defying the conventional Maxwell electrodynamics, in which electric field and magnetic field are orthogonal. The topological magnetoelectric (TME) effect, is a signature phenomenon derived from the axion electrodynamics, where the crossed induction of magnetization and electric polarization are expected to occur by applying external electric and magnetic fields, respectively. The TME effect can be described by the so called θ term show below, in addition to the ordinary Maxwell terms:

$$S_\theta = \frac{\theta e^2}{2\pi h} \int d^3x dt \vec{E} \cdot \vec{B} \quad (3 - 1)$$

where \vec{E} and \vec{B} are the electric and magnetic field, θ is a dimensionless parameter which denotes the axion field [68]. For a trivial insulator, $\theta = 0$, while for a TI, $\theta = \pi$. θ can take value of 0 or π for time-reversal symmetric systems. This θ term is also related to the axion electrodynamics in particle physics [68].

Indeed, the axion is also being studied by particle physicists as a building block of dark matter. It is intriguing to note that these ingenious structures give a possibility to study the counterpart of the physics of dark matter in solid states. A QAH sandwich structure, where two compositional different MTI layers with different coercivity are separated by an undoped TI layer, is predicted to host the axion insulator quantum phase [1]. The V- dopant has been shown to introduce ferromagnetism in BST and QAH effect has also be observed in V-BST [50]. The V-BST has a much larger coercivity than Cr-BST. Therefore, by asymmetrically doping Cr- and V- on the top/bottom surface while leave middle layers undoped, the axion insulator state can be realized by at certain magnetic field where top and bottom surface magnetization have the opposite direction. It is a promising platform for exploring the quantized topological magnetoelectric coupling and axion electrodynamics in condensed matter.

Up to now, the examination of the zero Hall conductance plateau ($\sigma_{xy} = 0$) was commonly applied as the direct evidence of axion insulator state [58, 69-71]. However, as discussed in Chapter 1.3, the QAH insulator in 2D limit (thickness $\leq 6nm$) can also have the zero Hall conductance plateau due to top and bottom surface hybridization effect [49, 72, 73]. Therefore, we carried out a systematic thickness dependent study, and detailed transport measurements, to understand the difference between QAH and axion insulator.

3.1 Dimension crossover from QAH to axion insulator

In such a Cr-BST/ BST/ V-BST sandwiched 3D TI system, the undoped TI layer in the middle, is essential to decouple the exchange coupling between top and bottom layers. Therefore, we carried out a systematic thickness dependent study by varying middle layer BST thickness. Cr-BST (3nm) / BST (t) / V-BST (3nm) sandwiched films were prepared by MBE, with $t = 0, 2, 4, 6, 8$ nm. In addition, a 6nm Cr-BST QAH insulator was prepared as a comparison. All the films were patterned into $40\mu\text{m} \times 20\mu\text{m}$ Hall bar devices by photolithography, and top electric gates were fabricated by exfoliated hexagonal boron nitride (h-BN). During the measurements, the gate voltage is set at $V_g=V_{g0}$ to optimize the sample's Fermi level position, and a low frequency AC current with 5nA amplitude was applied through the source and drain. Fig. 3-1 shows the magnetic field dependence of the longitudinal and Hall conductance of all the samples.

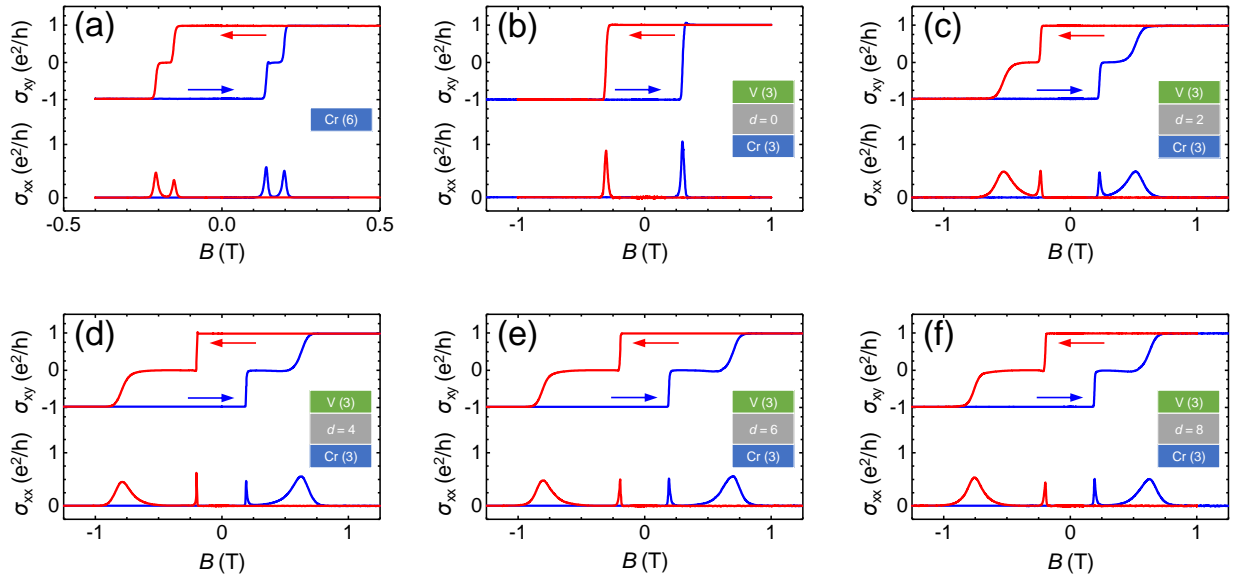


Figure 3- 1 Quantum anomalous Hall insulator and its sandwich heterostructures.

Longitudinal and Hall conductance of (a) 6 nm Cr-(Bi,Sb)₂Te₃ QAH insulator, sandwich

heterostructures of 3 nm V-(Bi,Sb)₂Te₃ and 3 nm Cr-(Bi,Sb)₂Te₃ separated by undoped (Bi,Sb)₂Te₃ with thickness of **(b)** 0 nm, **(c)** 2 nm, **(d)** 4 nm, **(e)** 6 nm, and **(f)** 8 nm.

As shown in Fig. 3-1 a, the regular 6nm Cr-BST QAH insulator shows a good quantization with $\sigma_{xy} = \pm e^2/h$ and $\sigma_{xx} = 0$ when fully magnetized, as well as a zero-Hall plateau ($\sigma_{xy} = 0$) near coercivity, which is a topological trivial normal insulator state [49, 72, 73]. For the BST (3nm) / V-BST (3nm) bilayer (Fig. 3-1 b), it also shows good QAH states by no zero-Hall plateau was observed. With the introduction of 2nm middle undoped BST layer (Fig. 3-1 c), the zero-Hall plateau starts to form, and with the increase of its thickness to 4nm (Fig. 3-1 d), 6nm (Fig. 3-1 e), and 8nm (Fig. 3-1 f), the zero-Hall plateau becomes more obvious and exists on a wider magnetic field range. This observation, where the signature zero-Hall plateau for axion insulator become more obvious as the system transits from a 2D QAH insulator into 3D regime, matches well with the theory that the axion insulator, in principle should be a three-dimensional topological insulator [1, 74].

3.2 Zero-Hall plateau in QAH and axion insulator

However, the zero-Hall plateau are not enough to serve as the direct evidence of axion insulator state, since some 2D QAH insulator can also have the zero Hall plateau (as shown in Fig. 3-1 a). Here we carried out the minor loops measurements to understand the different origins of $\sigma_{xy} = 0$ plateaus in 2D QAH insulator and 3D axion insulator. The minor magnetic hysteresis loop scan, where the cycling field is not enough to saturate the whole system, is usually applied to separate each individual ferromagnetic orders in a complex system. In our system, the minor loop scan starts at a saturated state ($\sigma_{xy} = \pm e^2/h$) and returns back when it reaches the zero-Hall

plateau middle state ($\sigma_{xy} = 0$). Moreover, multiple minor loops were studied, where each loop has a different returning point in the $\sigma_{xy} = 0$ plateau region.

Fig. 3-2 shows the minor loops of all the five samples with $\sigma_{xy} = 0$ plateaus, where the top panels show the minor loops starting from $\sigma_{xy} = e^2/h$ while bottom panels show the minor loops starting from $\sigma_{xy} = -e^2/h$. The minor loops with different colors have the different returning points in the plateau region, with blue color showing the returning point most “shallow” in the plateau, while red color showing the returning point going most “deep” into the plateau region. As shown in Fig. 3-2 a, the minor loops of the 2D QAH insulator don’t collapse at a single magnetic field when scanned back. On the contrary, for the axion insulators with 2nm (Fig. 3-2 b), 4nm (Fig. 3-2 c), 6nm (Fig. 3-2 d), and 8nm (Fig. 3-2 e) undoped BST middle layer, all minor loops can well collapse at the same magnetic field when scanned back.

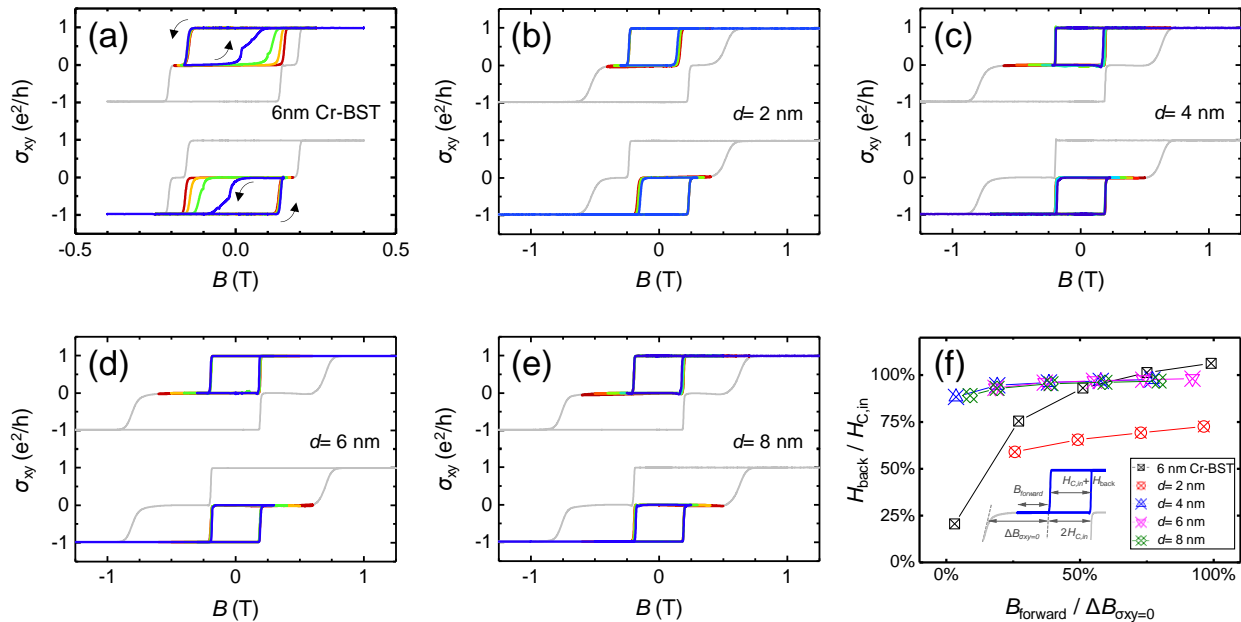


Figure 3- 2 Minor loop hysteresis of QAH insulator and axion insulators. Multiple minor loop hysteresis measurements of (a) 6 nm Cr-(Bi,Sb)₂Te₃ QAH insulator, sandwich heterostructures with undoped (Bi,Sb)₂Te₃ thickness of (b) 2 nm, (c) 4 nm, (d) 6 nm, and (e) 8

nm. **(f)** Summarized magnetization reversal ratios for minor loops stopped at different locations inside the zero σ_{xy} plateaus.

To quantitatively evaluate the degree of how minor loops merge together, we introduced two indicators. $B_{forward}/\Delta B_{\sigma_{xy}=0}$ where $\Delta B_{\sigma_{xy}=0}$ is the zero-Hall plateau width, describes how “deep” the returning point goes into the plateau region. In other words, the minor loops in blue color has smaller value of $B_{forward}/\Delta B_{\sigma_{xy}=0}$ while the ones in red color have largest value. Another indicator $H_{back}/H_{c,in}$ represents how much magnetization the minor loops have reversed, where $H_{c,in}$ is the coercivity field of the inner edge, and H_{back} is the field needed to reverse half of the magnetization back when scanned back. More precisely, $H_{c,in}$ and H_{back} were taken at $\sigma_{xy} = 0.5e^2/h$ for the top panels and $\sigma_{xy} = -0.5e^2/h$ for the bottom panels in Fig. 3-2. The summarized $H_{back}/H_{c,in}$ versus $B_{forward}/\Delta B_{\sigma_{xy}=0}$ are shown in Fig. 3-2 f. It is shown that, in 2D QAH (black curve), the y-axis shows strong dependence with x-axis, increasing from 20% to 100%. This means the sample only has one coercivity and different minor loops are at different multi-domain states during a continuous magnetic transition. In the other curves, y-axis shows almost no dependence on the x-axis, which means that axion insulators have two separate coercivities and different minor loops have the same magnetic profile. In other words, Cr-BST layer with smaller coercivity is switched while V-BST layer with larger coercivity is not, due to the middle undoped BST layer weakening their inter layer exchange interaction. Interestingly, unlike the other axion insulator samples, the y-axis of Cr-BST (3nm) / BST (2nm) / V-BST (3nm) sample shows a value of around 60-70%, which is far smaller than 100%. This might be due to the existence of an exchange bias effect between the Cr-BST layer and V-BST layer, possibly from the long-range RKKY magnetic interaction that has been discussed in Chapter 1.3. In conclusion, we show that an undoped BST middle layer with thickness ≥ 2 nm is essential to

separate the top and bottom ferromagnetism and to realized axion insulator state. We also show that the minor loops serve as an effectively method to distinguish the different origins of zero-Hall plateaus in 2D QAH insulator and 3D axion insulator.

3.3 Temperature scaling behaviors

In addition, we carried out the temperature dependent measurements. Fig. 3-3 shows the magnetic field dependent Hall conductance σ_{xy} of all the devices measured at various temperature ranging from 100 mK to 1 K. The zero-Hall plateau width for all samples were further summarized in Fig. 3-4 g. It is shown that, the zero-Hall plateau becomes less obvious with increasing temperature, and the zero-Hall plateau in axion insulator can survive in a larger temperature range than in QAH insulator. The conductivity tensor flow diagrams were constructed in Fig. 3-4 (a-f), which show the evolution of σ_{xx} versus σ_{xy} upon magnetic field sweeps at various temperatures. The samples with $\sigma_{xy} = 0$ plateaus show two semi-circle behaviors centered at $(\sigma_{xy}, \sigma_{xx}) = (\pm 0.5 e^2/h, 0)$ with a radius of $0.5 e^2/h$, While the Cr-BST (3nm) / V-BST (3nm) bilayer sample shows one larger semi-circle centered at (0, 0) with a radius of e^2/h .

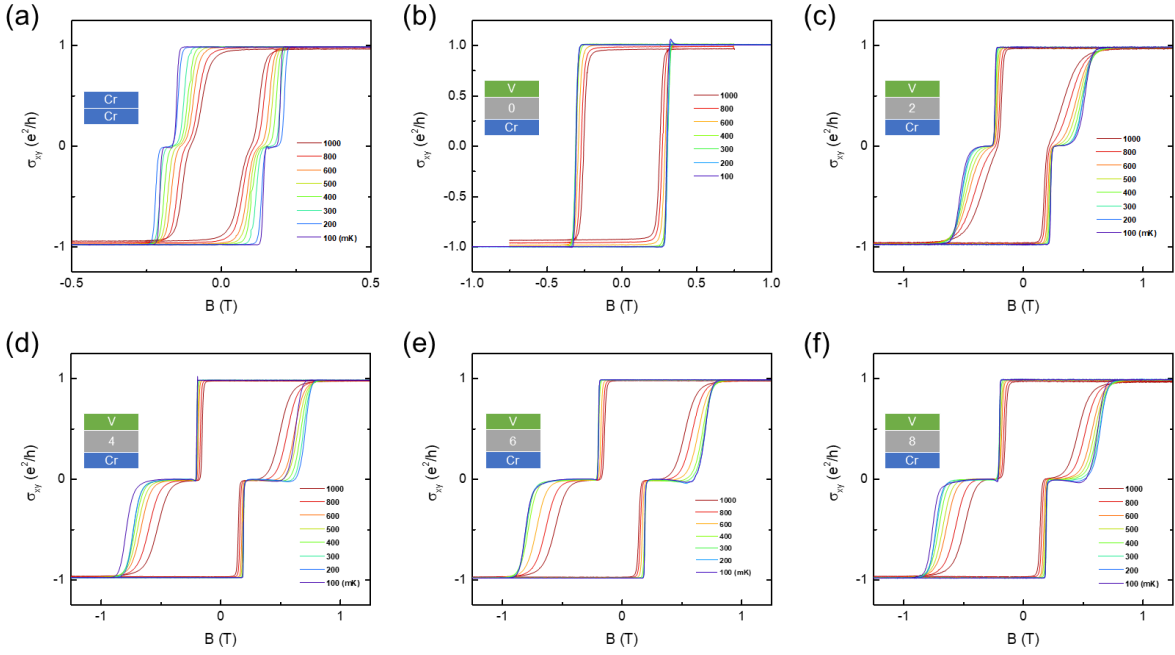


Figure 3- 3 Magnetic field dependence of σ_{xy} at various temperatures. (a) 6nm Cr-(Bi,Sb)₂Te₃ QAH insulator, axion insulators with various middle undoped (Bi,Sb)₂Te₃ layer thickness of (b) 0nm, (c) 2nm, (d) 4nm, (e) 6nm, and (f) 8nm.

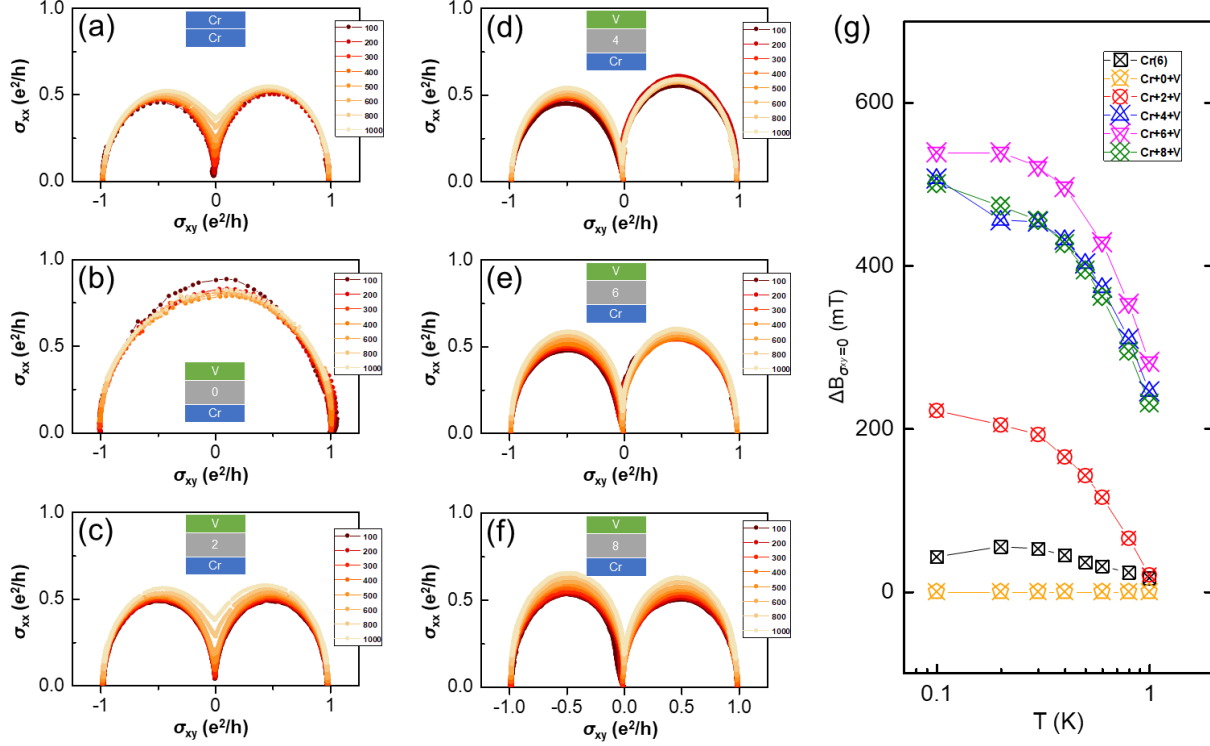


Figure 3- 4 Conductivity tensor flow diagram at various temperatures. (a) 6nm Cr-(Bi,Sb)₂Te₃ QAH insulator, axion insulators with various middle undoped (Bi,Sb)₂Te₃ layer thickness of (b) 0nm, (c) 2nm, (d) 4nm, (e) 6nm, and (f) 8nm. (g) The summarized temperature dependence of zero Hall plateau width in all samples.

To further understand the different physics related to the zero Hall plateau in QAH insulator and in axion insulator, we then conducted the scaling analysis of the quantum phase transition between $\sigma_{xy} = 0$ plateaus and $\sigma_{xy} = \pm e^2/h$ plateaus. The plateau-to-plateau transition in σ_{xy} is accompanied by a field-driven metal-insulator transition. Unlike in the QHE where the plateau-to-plateau transition and the metal-insulator transition occur independently at different filling factors, these two transitions occur simultaneously in QAH transition. The maximum slope of the σ_{xy} trace $(\partial\sigma_{xy}/\partial B)_{max}$ between the $\sigma_{xy} = \pm e^2/h$ plateaus and the $\sigma_{xy} = 0$ plateau is extracted from Fig. 3-3, and plotted as a function of temperature in Fig. 3-5, where the blue dots

describe the $\sigma_{xy} = 0$ to $\sigma_{xy} = + e^2/h$ transition and red dots describe the $\sigma_{xy} = 0$ to $\sigma_{xy} = - e^2/h$ transition. It is found that $(\partial\sigma_{xy}/\partial B)_{max}$ decrease with the increasing temperature. As a result of the critical behavior of the quantum phase transition, a linear dependence of $(\partial\sigma_{xy}/\partial B)_{max}$ on the temperature T is found in the log-log plot, consistent with the theoretically predicted power-law relationship [72]: $(\partial\sigma_{xy}/\partial B)_{max} \propto T^{-\kappa}$.

The critical component κ was then extracted by linear fitting of the log-log plot. We find $\kappa = 0.6$ for 6nm Cr-BST QAH insulator (Fig. 3-5 a), which is in consistence with previously reported κ value of 0.61 by [75] and 0.62 by [76] in QAH system. For the axion insulators with undoped BST middle layer thickness of 2nm, 4nm, 6nm, and 8nm, we find $\kappa = 0.45, 0.41, 0.39,$ and 0.38 respectively (Fig. 3-5 b-e). This is also in consistence with previously reported κ value of 0.47 in 8nm MnBi_2Te_4 axion insulator [77], and 0.38 in Cr-BST (3nm) / BST (5nm) / V-BST (3nm) axion insulator [78]. The temperature scaling exponent κ versus middle layer BST thickness was summarized in Fig. 3-5 f. The distinct difference of the κ value in the 6nm Cr-BST QAH insulator and Cr-BST (3nm) / BST ($t \geq 2\text{nm}$) / V-BST (3nm) axion insulator samples, indicates the different physical types of the two quantum phase transitions: in the QAH insulator it represents the phase transition between Chern insulator state and topologically trivial insulator state, while in axion insulators it corresponds to the phase transition between Chern insulator state and topologically nontrivial axion insulator state. For axion insulators, the κ values are pretty close to that of conventional quantum Hall plateau-to-plateau phase transitions ($\kappa \sim 0.42$ [79]), indicating that the Chern insulator to axion insulator phase transition may share the same universality class with quantum Hall phase transitions. The dereasing trend of the κ value with the increasing thickness, also indicates a dimension crossover from a 2D QAH insulator into 3D axion insulator.

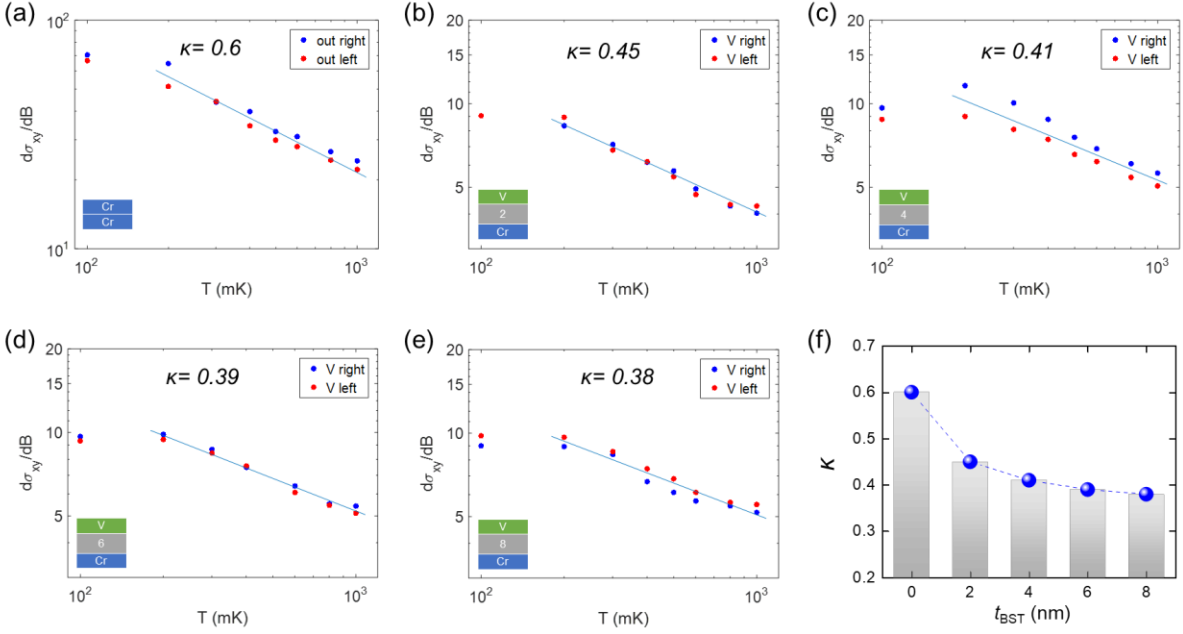


Figure 3- 5 Temperature scaling behaviors of the plateau-to-plateau transition. Temperature dependence of $(\partial\sigma_{xy}/\partial B)_{max}$ extracted from Fig. 3-15 of (a) 6nm QAH insulator, axion insulators with various middle undoped BST layer thickness of (b) 2nm, (c) 4nm, (d) 6nm, and (e) 8nm. (f) The summarized temperature scaling exponent κ versus middle layer BST thickness.

3.4 Summary of chapter 3

In this work, we carried out a systematic thickness dependent study on MTI / TI / MTI sandwiched structures. By varying undoped BST middle layer thickness we observed a dimension crossover between 2D QAH and 3D axion insulators. We emphasized that the zero Hall conductance plateau ($\sigma_{xy} = 0$) was not adequate evidence for determine axion insulator state, because it can also be seen in 2D QAH insulators. We carried out detailed multiple minor loops scans observed distinct behaviors of QAH insulator and axion insulators, which may serve as a

powerful method to distinguish the $\sigma_{xy} = 0$ plateaus of the two. Finally, we did the temperature scaling analysis to study the critical behavior of the σ_{xy} plateau-to-plateau phase transitions. The different critical component κ values in QAH insulators and axion insulator, again indicates the different universality classes of the two quantum phase transitions.

Chapter 4 QAH insulator and antiferromagnetic heterostructures

As mentioned in Chapter 1.3, there are two approaches to introduce magnetism into 3D TIs. While introducing magnetic dopants during the growth is an effective way to introduce ferromagnetism in TI, extensive efforts have been also devoted to proximity coupling TI or MTI materials to other strongly magnetically ordered compounds to engineer the time-reversal symmetry breaking in topological surface states. Proximity coupling to more uniform or stronger magnetic materials, such as $\text{Y}_3\text{Fe}_5\text{O}_{12}$ (YIG) [23, 24, 80, 81], $\text{Tm}_3\text{Fe}_5\text{O}_{12}$ (TIG) [25], EuS [26-28, 82], $\text{Cr}_2\text{Ge}_2\text{Te}_6$ [29, 30], CrSb [32], CrSe [31] etc. has been employed to introduce ferromagnetism into otherwise nonmagnetic TIs and to enhance the Curie temperature of MTI films. Moreover, the proximity effect through the interface also implements exchange coupling as an additional degree of freedom through which the topological surface states can be manipulated. Followed by Chapter 2 where we studied MTI film itself and its sandwich structures, in this Chapter we will focus on the heterostructures of MTI and other magnetic materials.

While the successful integration of topological and (anti)ferromagnetic layers has been demonstrated, direct manipulation of the quantized states through exchange interactions remains elusive. Two main challenges are causing this difficulty. First, this (anti)ferromagnetic layer needs to be highly insulating to avoid current shunting effect. Second, the critical growth requirements for achieving the QAHE set hard limits to the crystal structure and quality of the (anti)ferrimagnetic material candidates.

4.1 Cr-BST/ Cr_2O_3 heterostructures

An ideal candidate fulfilling the above two requirements is Cr_2O_3 , which is an antiferromagnetic insulator with a Néel temperature near 300 K. On its own, Cr_2O_3 is of interest as a magnetoelectric material with potential applications in electrical control of either AFM domains or adjacent ferromagnetic (FM) layers through exchange coupling [83-86]. As shown in Fig. 4-1 a, Cr_2O_3 has a hexagonal crystal structure with a lattice constant $a=0.496$ nm, and its Cr spins are generally aligned parallel or antiparallel to $[0001]$ crystal direction, resulting in a robust AFM order along its c-axis. This crystal structure makes it a suitable substrate for the growth of high-quality MTI [64, 87].

The Cr_2O_3 films used in this study were deposited by either MBE or sputtering on $\text{Al}_2\text{O}_3(0001)$ substrates, and subsequent MTI growth were performed in a separate MBE chamber. By carefully tuning the parameters, we successfully achieved high-quality MTI growth on Cr_2O_3 . As shown in Fig. 4-1b, a clear boundary across the MTI/ Cr_2O_3 interface and the well-defined van der Waals structure of the MTI are observed. Remarkably, we are able to observe QAH state in MTI/ Cr_2O_3 (sample 1), as shown in Fig 4-1c, where the Hall resistivity reaches the quantized value of h/e^2 when sample is cooled down to 20 mK.

The exchange coupling between the two materials is investigated using field-cooling-dependent magnetometry. It shows an absence of exchange bias when the sample (sample 1) is field-cooled under an out-of-plane magnetic field (Fig 4-1d), while a clear positive exchange bias can be observed in a non-quantized sample (sample 2) (Fig 4-1e). The exchange bias field for both the QAHI/ Cr_2O_3 and the non-quantized MTI/ Cr_2O_3 are extracted and presented in Fig 4-1f. Apart from our study, ref [87] has also reported exchange bias MTI/ Cr_2O_3 heterostructure. While the existence of exchange bias shows strong interfacial interaction between the antiferromagnetic order of the Cr_2O_3 and the magnetic topological insulator, it has never been simultaneously

observed with the existence of the QAH state [64].

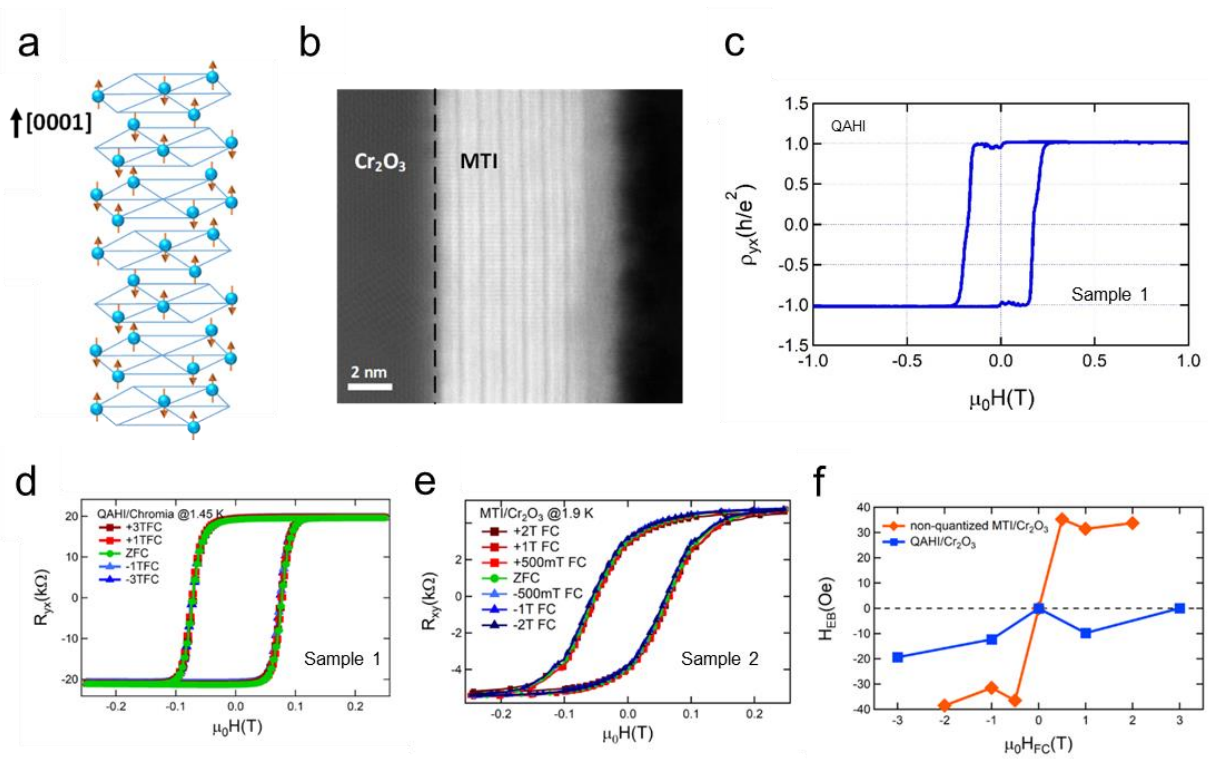


Figure 4- 1 QAH and exchange bias in Cr-BST/Cr₂O₃ heterostructure. (a) Crystal and spin structure of antiferromagnet Cr₂O₃ (only Cr atoms are shown). Cr atoms show a buckled arrangement. (b) HAADF-STEM of the MTI/ Cr₂O₃ heterostructure. (c) Quantized Hall resistance of MTI/Cr₂O₃ heterostructure (sample 1) seen at 20 mK. (d) Hysteresis loop at 1.45 K of sample 1 after different field cooling conditions, no exchange bias shift was observed in this sample. (e) Hysteresis loops of non-quantized MTI/Cr₂O₃ heterostructure (sample 2) after different magnetic field cooling shows a clear positive exchange bias. (f) comparison of the exchange bias magnitudes of QAHI/Cr₂O₃ and non-quantized MTI/Cr₂O₃ structures. Adopted from Ref. [64].

4.2 Cr-BST/Al-Cr₂O₃ heterostructures

While Cr_2O_3 is promising for low energy spintronic devices, the single domain state necessary for practical applications is challenging to achieve in AFM devices. This issue may be resolved through the introduction of nonmagnetic Al dopants into the Cr_2O_3 thin film during the growth, which yields a ferrimagnetic-like moment also known as a parasitic magnetization. This emergent magnetization has been attributed to the preferential occupation of Al on one of the two Cr sublattices [77, 88]. As illustrated in Fig. 4-2a, the Cr spins in Cr_2O_3 align parallel or antiparallel to [0001] forming a Néel vector along the c -axis, while the introduction of Al dopants breaks the symmetry of the two AFM sublattices. This unique parasitic enables deterministic control of the AFM domain structure and strengthens exchange-coupling with neighboring layers while preserving exciting properties, such as magnetoelectricity, from the parent compound.

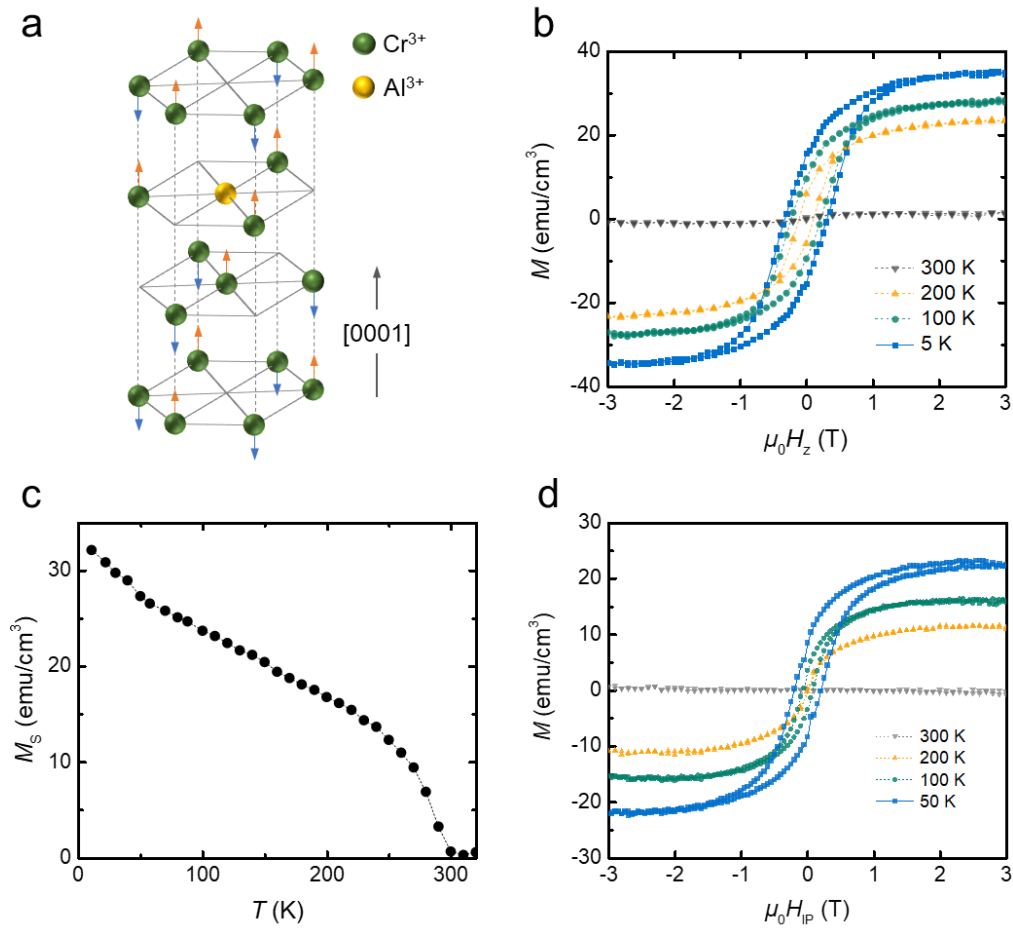


Figure 4- 2 Atomic structure and magnetic property of Al-doped Cr₂O₃. (a) Atomic and magnetic structure of Al-doped Cr₂O₃. Oxygen atoms are omitted for simplicity. Al³⁺ substitution of Cr³⁺ change the AFM Cr₂O₃ into a ferrimagnetic-like magnetic structure. (b) M-H_z profile of 50 nm Al-Cr₂O₃ substrate showing hysteresis loops below 300 K. A linear, diamagnetic background associated with the Al₂O₃ substrate has been subtracted from all presented curves. (c) Temperature dependence of saturated magnetic moment of 50 nm Al-Cr₂O₃ substrate measured with an out-of-plane field of +2 T. (d) The in-plane M-H SQUID characterization.

The 50 nm thick 5% Al-doped Cr₂O₃ was deposited on α-Al₂O₃ (0001) substrates by magnetron sputtering, and its magnetic properties were characterized using a superconducting

quantum interference device (SQUID) magnetometer. Fig. 4-2b shows the out-of-plane magnetization profile of the 5% Al-doped Cr_2O_3 measured at multiple temperatures. Clear hysteresis loops were observed, consistent with the expected ferrimagnetic-like dopant-induced parasitic magnetization. The non-square shape of the out-of-plane hysteresis, combined with the observation of hysteresis loops under the in-plane field with a lower saturation magnetization (Fig. 4-2d), indicates a weak perpendicular magnetic anisotropy (PMA). However, a strong perpendicular exchange coupling can still be achieved in this bilayer system. The temperature evolution of the saturated magnetization in Fig. 4-2c indicates a critical temperature near 300 K, which is consistent with the Néel temperature (T_N) of 307 K [86] in pristine Cr_2O_3 .

To fabricate the Al- Cr_2O_3 /MTI bilayers presented in this study, Cr doped $(\text{Bi,Sb})_2\text{Te}_3$ (CBST) layers were consequently grown on 50 nm thick 5% Al-doped Cr_2O_3 using molecular beam epitaxy (MBE). CBST layers were grown with a thickness of 6 quintuple layer (QL) for transport studies, while thicker films (20 QL) were prepared for scanning transmission electron microscopy (STEM) characterization and polarized neutron reflectometry (PNR) studies. Both the sputtered Al- Cr_2O_3 and MBE grown CBST showed good single-crystalline quality, as indicated by the streaky reflection high-energy electron diffraction (RHEED) patterns both before and after the epitaxy of CBST (Fig. 4-3a). An atomically sharp interface between Al_2O_3 and Al- Cr_2O_3 , as well as the sharp interface to CBST layer can be seen from the high-angle annular dark field (HAADF) STEM in Fig. 4-3b and Fig. 4-3c, respectively.

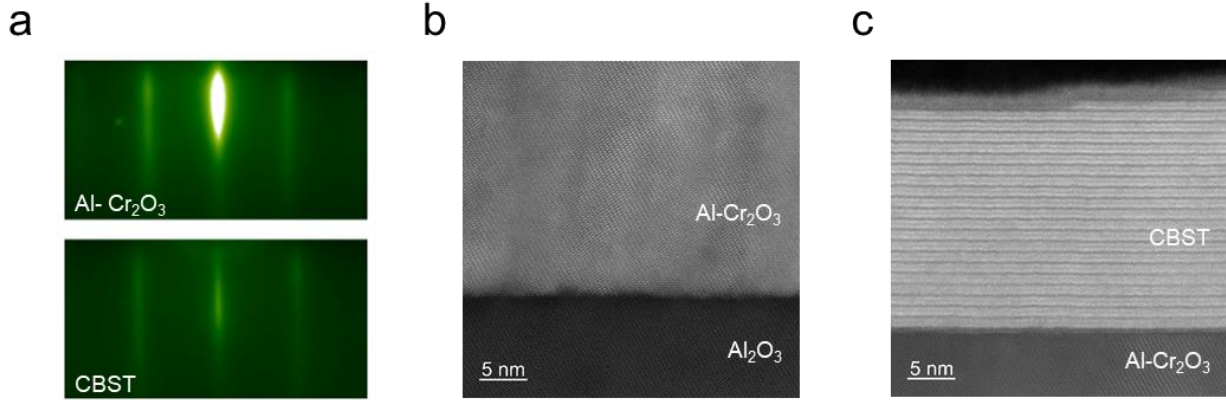


Figure 4- 3 High quality Cr doped BST grown by molecular beam epitaxy on Al-doped Cr₂O₃ (0001). a. RHEED pattern of the Al-Cr₂O₃ substrates and MBE grown CBST on top along <11-20> direction. b. HAADF-STEM of the Al₂O₃/Al-Cr₂O₃ interface. c. HAADF-STEM of the Al-Cr₂O₃/CBST interface.

4.3 Interfacial coupling in Cr-BST/Al-Cr₂O₃ probed by PNR

To probe the interfacial coupling between the Al-doped Cr₂O₃ and CBST, we performed PNR measurements on a 20 QL CBST grown on a 50 nm Al-doped Cr₂O₃. PNR gives a measure of the depth-dependent magnetization of these bilayers. Specular reflectometry (\vec{Q} perpendicular to the surface) is sensitive to in-plane moments only, so measurements were performed with an in-plane applied field, at a base temperature of 6 K. The spin asymmetries extracted from these measurements ($SA = \frac{R^{++}-R^{--}}{R^{++}+R^{--}}$) as well as the best-fit nuclear and magnetic profiles are shown in Fig. 4-4.

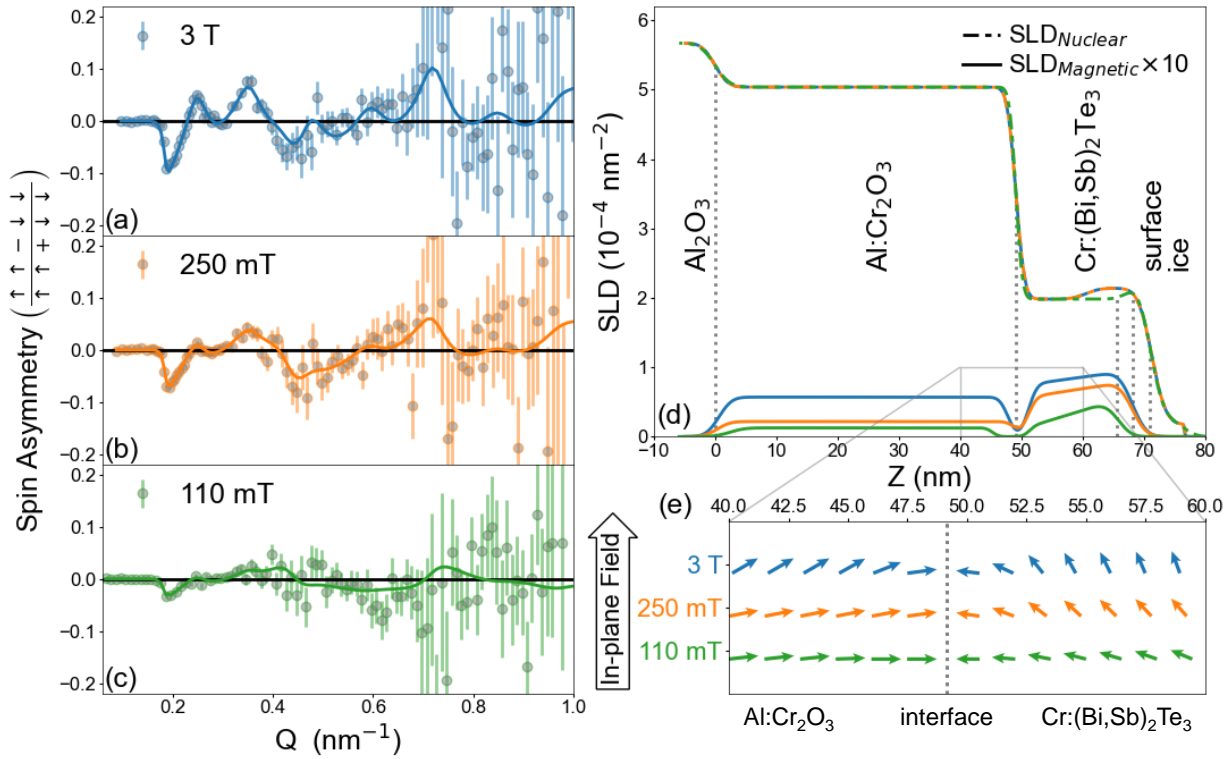


Figure 4- 4 Interfacial coupling between Al-Cr₂O₃ and CBST layers probed by PNR. a-c. Spin asymmetry of an Al-Cr₂O₃/CBST bilayer measured by polarized neutron reflectometry with applied in-plane magnetic fields of a. 3 T, b. 250 mT, and c. 110 mT. Solid lines show the best fits, which are generated by d. nuclear and in-plane magnetic depth-profile models. Due to aging, surface oxidation and adsorption varied between subsequent measurements. e. Possible orientation and relative magnitude of the net magnetization near the interface, deduced from (d), the in-plane magnetic scattering length density (SLD), and magnetometry results. This schematic assumes that the Al-Cr₂O₃ sublattices rotate together and does not illustrate the effect of domains. All error bars represent ± 1 standard deviation.

The best fit model indicates a region of zero in-plane magnetization at the interface between the CBST and Al-Cr₂O₃, a feature which persists under in-plane fields as large as 3 T. An absence of interfacial magnetization is not uncommon in multilayer magnetic heterostructures,

and typically indicates the presence of a magnetic dead layer. However, the observation of a robust and repeatable exchange biasing effect in these films (as will be discussed below) is inconsistent with the presence of a conventional dead layer at the interface. Rather, we propose that a strong exchange coupling between the CBST and Al-Cr₂O₃ surface spins pins the interfacial magnetization along the film normal. This is consistent with previous work [83, 89], in which the well-known Cr₂O₃ surface reconstruction fixes interfacial spins along the out-of-plane direction, yielding the pinning of the interfacial CBST moments along the film normal direction. Based on previous works [64, 87], we assume antiparallel alignment across the interface.

Additionally, the best model is in which the magnetic moments within the CBST layer gradually cant from an out-of-plane orientation at the interface towards the in-plane direction at the top surface of the film. A schematic of the moment orientation is shown in Fig. 4-4e. The canting of moments in the CBST layer, up to a maximum of 31 emu/cc (1 emu/cc = 1 kA/m) in-plane at 3 T, becomes more gradual as the field decreases, indicating strong exchange coupling between Cr moments within the CBST; however, this gradual moment canting is not present in the Al-Cr₂O₃ layer, which exhibits a uniform increase in magnetization with increasing field. This matches the observation that Al-Cr₂O₃ is magnetically harder than CBST. Further, the maximum in-plane magnetization at 7 K and 3 T in-plane of 20 emu/cc within the Al-Cr₂O₃ extracted from the PNR result matches the suppressed saturation magnetization of the in-plane hysteresis behavior measured using SQUID (Fig. 4-2b). We conclude, therefore, that some fraction of the Al-Cr₂O₃ spins remain pinned along the film normal at all fields.

4.4 Exchange-biased QAH effect

Having measured the vertical magnetization profile in Al-Cr₂O₃/CBST bilayers, we carried out transport measurements to show the exchange-biased QAH effect in these heterostructures. The films were patterned into Hall-bar devices with a geometry of 1 mm by 0.5 mm, as shown in Fig. 4-5c inset, using a hard mask and dry etching method. The samples were cooled from 300 K to 50 mK with a +1 T perpendicular magnetic field applied. Fig. 4-5a shows a vanishing longitudinal resistance ρ_{xx} and quantized Hall resistance ρ_{xy} at cryogenic temperature, confirming these films do indeed display the typical signatures of the QAH effect. For further confirmation, conductivity tensor components were computed using the relations $\sigma_{xx} = \rho_{xx} / (\rho_{xx}^2 + \rho_{xy}^2)$ and $\sigma_{xy} = \rho_{xy} / (\rho_{xx}^2 + \rho_{xy}^2)$, indicating perfect quantization (Fig. 4-5b). The flow diagram in Fig. 4-5c shows the evolution of σ_{xx} versus σ_{xy} upon a magnetic field sweep between ± 0.2 T at the base temperature of 50 mK. It showed the transition between the two quantized Chern insulator states with Chern number $c = \pm 1$, $(\sigma_{xy}, \sigma_{xx}) = (c, 0)$, and an intermediate trivial insulator state, $(\sigma_{xy}, \sigma_{xx}) \rightarrow (0, 0)$, which is observed in QAH insulators with thickness $t \leq 6$ QL due to a competition between the magnetic exchange gap and surface hybridization gap [49, 72, 73], as discussed in Chapter 1.3.

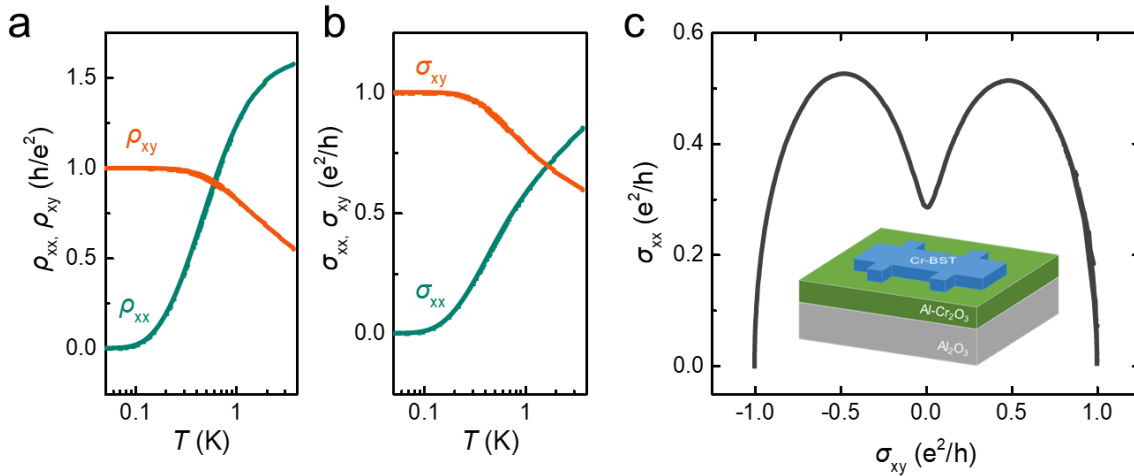


Figure 4- 5 Observation of quantum anomalous Hall effect in Al-Cr₂O₃/CBST

heterostructure. a. Temperature dependences of longitudinal resistivity ρ_{xx} and Hall resistivity ρ_{xy} under 1 T field, where ρ_{xx} vanishes and ρ_{xy} approaches the quantized value of h/e^2 with decreasing temperature. b. Temperature dependences of σ_{xx} and σ_{xy} converted from ρ_{xx} and ρ_{xy} . c. Evolution of the σ_{xx} versus σ_{xy} when scanning the magnetic field at 50mK.

The sample was then subjected to a small magnetic field sweep between ± 0.2 T. The field sweep range was larger than the coercivity of CBST but smaller than that of Al-Cr₂O₃, such that the magnetization of the latter remained intact during the sweep. The sample showed an exchange-biased quantum anomalous Hall effect as evidenced by a shift of the coercivity field in both ρ_{xx} (Fig. 4-6a) and ρ_{xy} (Fig. 4-6b), under different Al-Cr₂O₃ magnetization initialization status. The exchange bias has a magnitude of around $2\mu_0 H_{eb} \approx 16$ mT, and a slightly asymmetric behavior of ρ_{xx} , which fully reverses, could be due to different spin texture at the Al-Cr₂O₃ and CBST interface under different field training conditions. Remarkably, the exchange bias was observed simultaneously with the QAH effect, showing that the presence of the exchange bias from the Al-Cr₂O₃ layer could effectively manipulate the QAH state in CBST.

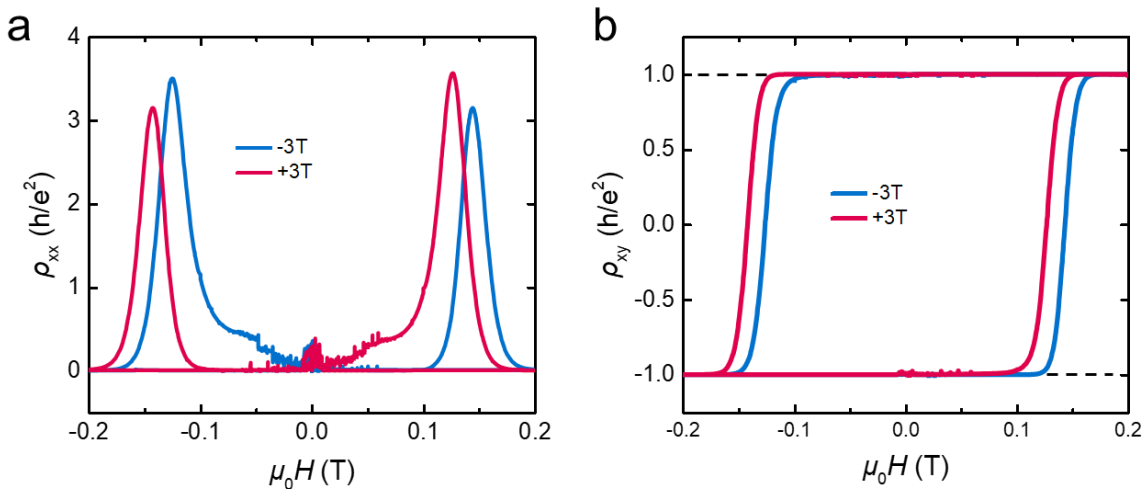


Figure 4- 6 Exchange-biased quantum anomalous Hall effect. Magnetic field dependences of (a) ρ_{xx} and (b) ρ_{xy} after training the sample using -3 T and +3 T to polarize the Al-Cr₂O₃ magnetization. The magnetic field was swept between ± 0.2 T and the data was taken at 50 mK.

4.5 Exchange-bias controlled by field training

We would like to emphasize that, the exchange-biased QAH effect could be controlled by a novel field-training (FT) approach, rather than traditional field cooling (FC) method. Field cooling is usually used to define the Néel vector of AFM materials, by applying a magnetic field and cooling through the Néel temperature. In Al-Cr₂O₃, the introduction of Al dopants breaks the symmetry of the two AFM sublattices and produces a nonzero net magnetization as indicated in the SQUID and PNR experiments. While an external magnetic field cannot couple to a perfectly compensated AFM order parameter, it can be used to switch the ferrimagnetic-like magnetic order in Al-Cr₂O₃. The use of Al-Cr₂O₃ thus has a significant advantage over its undoped counterpart Cr₂O₃ as the sign of any exchange bias may be changed through the application of an external magnetic field alone, without requiring the system be raised above its Néel temperature T_N .

To demonstrate this advantage, we show that the magnetism in Al-Cr₂O₃, and consequently the sign of the interfacial exchange bias, may be initialized using both field training and traditional field cooling methods. For field cooling, the sample was subjected to ± 3 T fields while cooling down from 330 K to 2 K. For field training, the sample was treated to ± 3 T and ± 9 T fields after it cooled down to 2 K. In all Al-Cr₂O₃ initialization scenarios, small magnetic field sweeps between ± 0.2 T were then performed at 2 K. As shown in Fig. 4-7a, after +3 T

field cooling, +3 T or +9 T field training, the device displays exactly the same behavior, and presents a pronounced exchange bias compared to the similar field cooling or field training process using a negative field, indicating that field training and field cooling are equally effective methods for establishing exchange bias in this system.

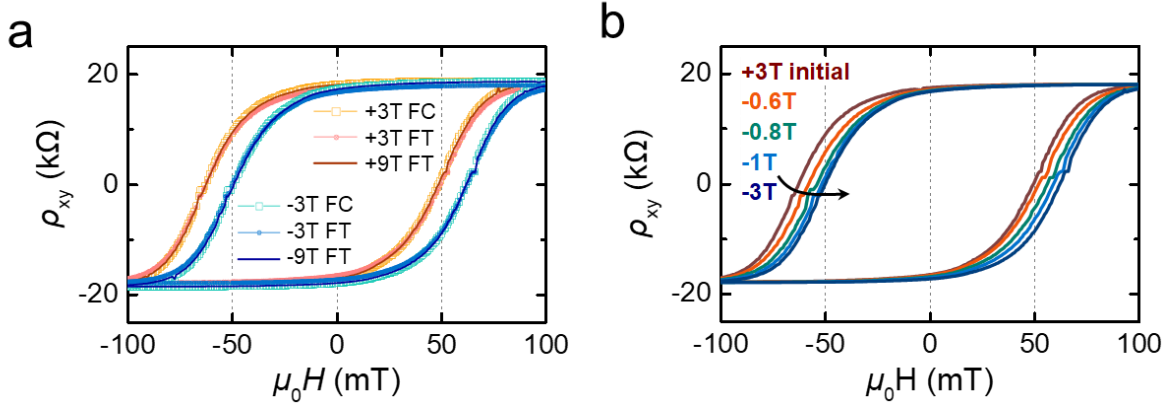


Figure 4- 7 Exchange bias manipulated by field-training of Al-Cr₂O₃. a. Small field sweep (± 0.2 T) of ρ_{xy} at $T = 2$ K, after treating the sample with ± 3 T, ± 9 T field training (FT) and ± 3 T field-cooling (FC) processes. b. Small field sweep (± 0.2 T) of ρ_{xy} at $T = 2$ K, after sample treated with various training field. +3 T field is applied to initialize the magnetization of Al-Cr₂O₃ before each field-training and loop scan.

The exchange bias was shown to be directly related to Al-Cr₂O₃ magnetization from the dependence of exchange bias on the externally applied training field. Before each small field sweep (± 0.2 T), a negative exchange bias was set using a +3 T field, and the sample was subsequently subjected to a training field of opposing sign $-\mu_0 H_{train}$ (Fig. 4-7b). The magnitude of this training field was varied between 0.2 T and 3 T, resulting in a gradual switching of Al-Cr₂O₃ magnetization. Shown in Fig. 4-7b is that the anomalous Hall loop of CBST gradually shifts to the positive direction and finally saturates with increasing training field, indicating a

sign change in the exchange bias. In this measurement series, zero exchange bias occurs with a training field of 0.7 T, whereas the value of the exchange bias saturates with training fields of approximately 1 T. These values correlate approximately with the coercivity and switching fields of Al-Cr₂O₃ obtained from the SQUID data in Fig. 4-2a.

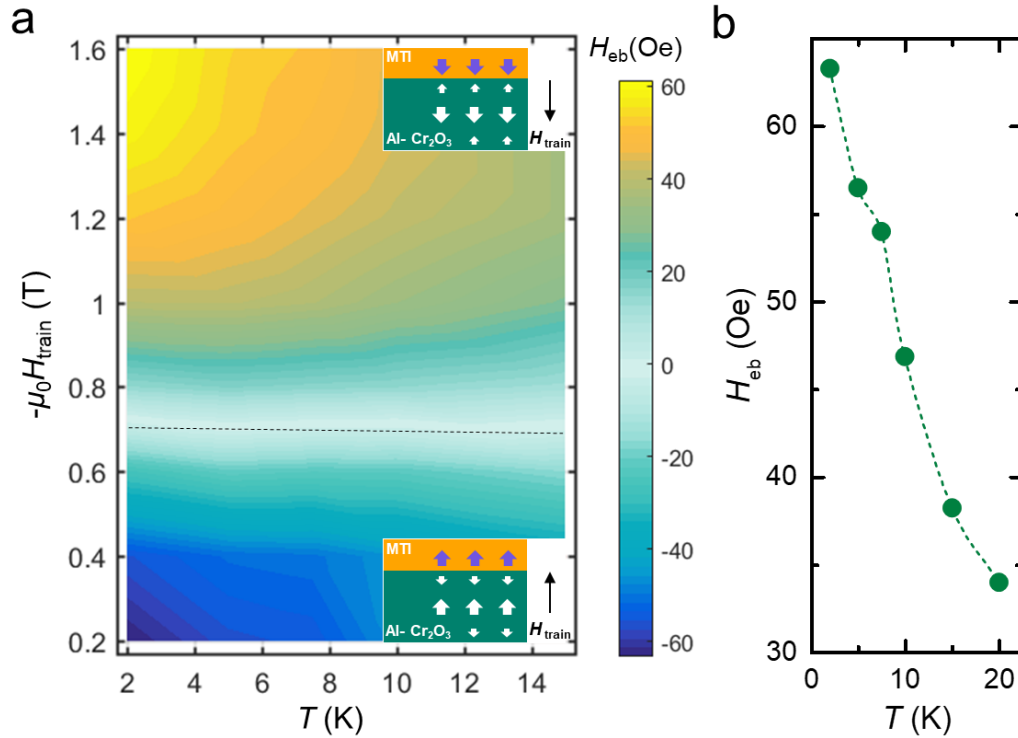


Figure 4- 8 Exchange bias manipulated by field-training of Al-Cr₂O₃. a. Mapping of the training field dependent exchange bias H_{eb} at different temperatures. The gradual switching of H_{eb} with increasing training field corresponds to the switching of the Al-Cr₂O₃ magnetization. b. Summarized temperature dependence of H_{eb} . The same device that has been described in Fig. 4-5 is studied for this measurement.

The same measurement was performed at different temperatures, and the exchange bias as a function of training field magnitude was obtained and shown in the color plot in Fig. 4-8a. The inset schematically illustrated the different signs of exchange bias under different training

fields due to the antiparallel alignment of the CBST and Al-Cr₂O₃ surface spins. The temperature dependence of $|H_{eb}|$ is summarized in Fig. 4-8b, where the exchange bias magnitude decreases with increasing temperature and vanishes when the temperature reaches above the Curie temperature (≈ 30 K) of CBST thin film. This observation, combined with the absence of magnetic proximity effects in an undoped BST and Al-Cr₂O₃ heterostructure (Fig. 4-9), indicates the exchange bias is most likely due to the dipolar interaction of Cr atoms between Al-Cr₂O₃ and CBST.

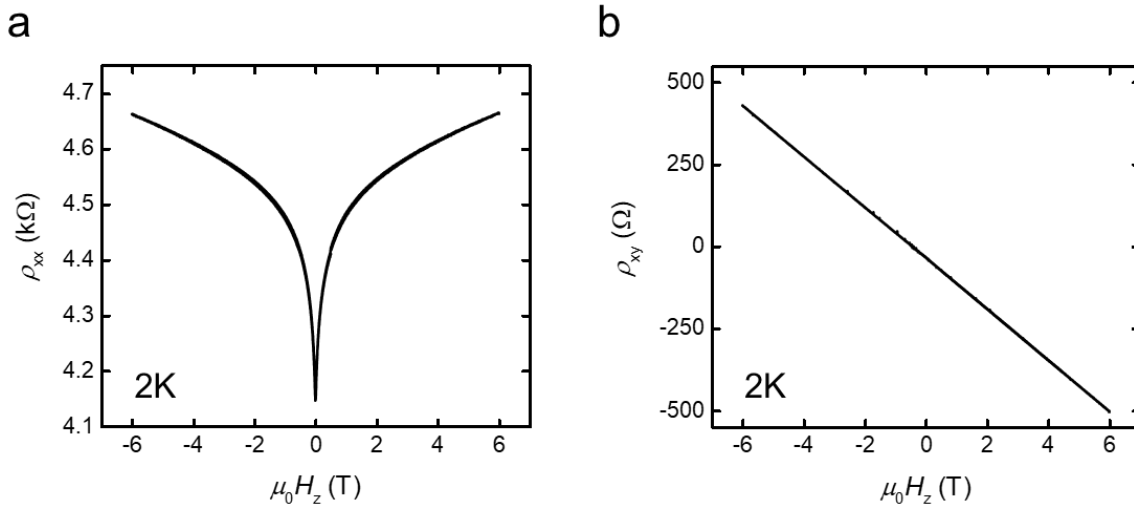


Figure 4- 9 Transport result of 6 nm undoped BST grown on Al-Cr₂O₃. (a) longitudinal resistance and (b) Hall resistance. The absence of a magnetic response within the conductive layer of BST indicates the absence of magnetic proximity effects between BST and Al-Cr₂O₃.

4.6 Summary of chapter 4

To summarize, we demonstrate high quality MBE growth of CBST on an uncompensated AFM insulator substrate (Al-Cr₂O₃). PNR measurements reveal a vanishing in-plane

magnetization at the Al-Cr₂O₃ and CBST interface, which, when taken together with the transport measurements, indicates a strong exchange coupling between the two magnetic layers pinning the moments at the interface to point out-of-plane. Interestingly, while earlier studies on undoped Cr₂O₃/MTI heterostructures reported that exchange bias and the QAHE were never observed simultaneously, the strong exchange coupling in Al-Cr₂O₃/CBST results in the ability to exchange bias the quantum anomalous Hall effect. We further demonstrate that the magnitude and sign of the exchange bias can be effectively controlled using a field training process to set the magnetization of the Al-Cr₂O₃ layer, so that it is possible to directly manipulate the exchange bias without the heating and cooling cycles needed in traditional field cool process. Thus, we can magnetically tune both the magnetic and topological properties of the MTI. This work successfully demonstrates the manipulation of QAH states by an adjacent magnetic layer through exchange coupling, which provides an additional degree of freedom through which the topological surface states can be manipulated. Our findings highlight the rich tuning possibilities in topological and AFM heterostructures, and this approach can also be used to understand and manipulate other emerging topological quantum phases such as axion insulator states [58, 69, 70] and high-Chern number QAH states [90].

Chapter 5 QAH insulator and superconductor heterostructures

Now in Chapter 4 we have discussed about heterostructures of QAH insulator and other magnetic materials. In this chapter, we will focus on heterostructures of QAH insulator and superconductors. QAH insulator when coupled with s-wave superconductor, is predicted to host chiral Majorana fermions. As a result, the QAH insulator and superconductor heterostructures have aroused wide research interests recently. Proposed by Ettore Majorana in 1937 [91], Majorana fermion was originally a hypothetic particle in high energy physics, which is an elementary spin-1/2 particle with its anti-particle being itself. The Majorana fermions obey non-Abelian statistics and can be potentially used to form topological qubits for fault-tolerant topological quantum computation [92-94]. The mysterious disappearance of Ettore Majorana in 1938 led to a long way to find evidence of its emergence in the following decades until today. In condensed-matter systems, the quasi-particles of Majorana fermions are predicted to exist in topological superconductors (TSCs) [3, 95, 96]. TSCs are predicted to appear in various systems such as $\nu = 5/2$ fractional quantum Hall system [97], spinless $p_x + ip_y$ superconductors [92, 98], strong spin-orbit-coupled semiconductor-superconductor heterostructures [99-104], topological insulator-superconductor heterostructures [99, 105, 106], etc. These proposals are mainly focusing on probing the Majorana zero mode, a zero-dimensional version of the Majorana fermion that exists strictly at zero energy.

Recently, a theoretical work predicted chiral Majorana edge modes (CMEMs), the one-dimensional version of the Majorana fermion, can exist when a quantum anomalous Hall (QAH) insulator is coupled to superconductors [107]. This chiral TSC in two dimensions will have a pairing gap in the bulk and odd number of gapless chiral Majorana fermion (CMF) modes at the edge. Followed by this proposal, a recent experimental work reported a half-quantized plateau in

the two-terminal conductance in a QAH-Nb bilayer and interpreted it as a distinct signature of the CMEMs [108]. However, a more recent study repeated the similar measurements, but got different results and argue an absence of evidence for CMEMs in QAH-Nb devices [109]. In this works, we studied the similar QAH-Nb devices, as well as QAH-normal metal devices, aiming to provide a better understanding of the transport behaviors of the QAH devices.

5.1 Chiral Majorana Fermion in hybrid QAH-SC bilayers

The proposed hybrid QAH-superconductor device for detecting CMZMs by Wang *et al.* [107] is shown in Fig. 5-1a. In this structure, the magnetic topological insulator (MTI) Cr-doped $(\text{Bi,Sb})_2\text{Te}_3$ is a platform to provide the QAH effect, while an s-wave superconductor Nb could act as a superconductivity reservoir to induce a superconducting gap into the middle mesa of the QAH insulator. The calculated phase diagram of the meddle region II is shown in Fig. 5-1b, where the x -axis λ is the exchange field along z axis induced by the ferromagnetism and can be changed during the magnetization reversal process in MTI, and the y -axis Δ is the magnitude of pairing gaps on the MTI top and bottom surface states, and \mathcal{N} is the Bogoliubov-de Gennes (BdG) Chern number. It is shown that, when superconducting proximity effect is sufficiently strong, region II will experience a series phase changing where BdG Chern number $\mathcal{N} = -2 \rightarrow -1 \rightarrow 0 \rightarrow 1 \rightarrow 2$ as the exchange field λ changes with magnetic hysteresis loop. The BdG Chern number \mathcal{N} of CMEMs has the relationship of $\mathcal{N} = 2C$ with the Chen number C of QAH, so $\mathcal{N} = \pm 2$ phases are actually the $C = \pm 1$ QAH phases, and $\mathcal{N} = 0$ phase is the $C = 0$ NI phase. Importantly, the $\mathcal{N} = \pm 1$ TSC states emerges near the transition between the QAH and NI phases and can result in a distinct edge transport signature in the two terminal conductance (Fig. 5-1c). It is shown that, with the change of magnetic field, σ_{12} exhibits plateaus quantized at e^2/h and 0

when region II is in $\mathcal{N} = \pm 2$ (QAH) and $\mathcal{N} = 0$ (NI) states. In addition, an intermediate half quantized plateau at $e^2/2h$ could occur near the coercivity, which is a unique signature of the $\mathcal{N} = \pm 1$ TSC in region II.

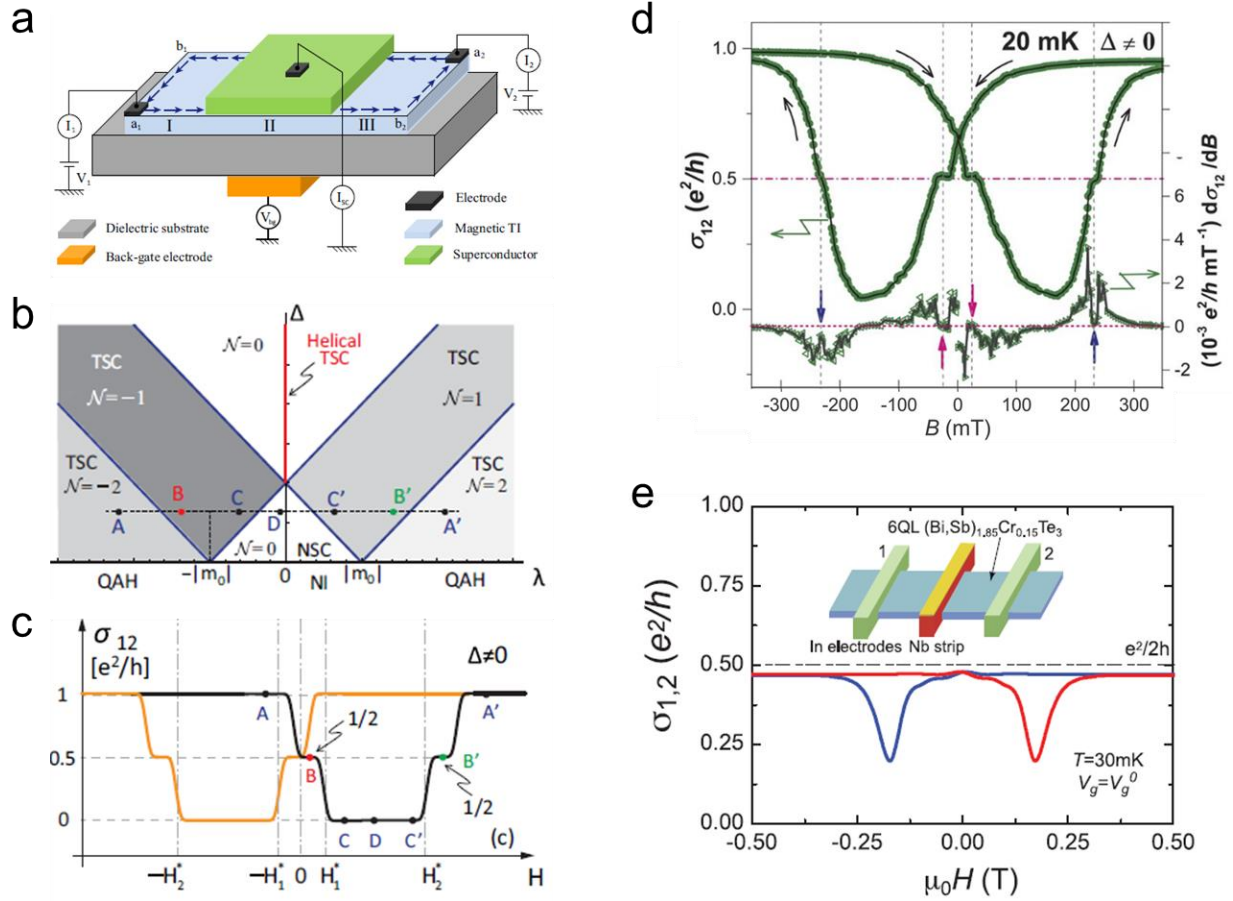


Figure 5- 1 Theoretical proposal and current experiment status for detecting CMF in hybrid QAH-SC bilayers. (a) Proposed hybrid QAH-SC device for detecting CMF, (b) phase diagram and (c) expected transport signature of CMF, adopted from [107]. (d) Experimentally measured σ_{12} as a function of the magnetic field in QAH-Nb devices claimed the existence of CMF, reported by [108]. (e) σ_{12} as a function of the magnetic field in QAH-Nb devices measured by another team raised a controversy, reported by [109].

Followed by this theoretical proposal, He *et al.* [108] fabricated QAH-SC hybrid heterostructure using MBE grown 6 QL Cr-doped $(\text{Bi,Sb})_2\text{Te}_3$ and sputtered 200nm Nb. By tracing the longitudinal conductance (σ_{12}) across this QAH-TSC-QAH junction under a perpendicular magnetic field, the signature $\sigma_{12} = e^2/2h$ plateaus were observed as shown in Fig. 5-1d. However, in a more recent work [109], where the similar devices were fabricated and similar measurements were performed, the transport results showed the absence of these CMZM signatures. Instead, as shown in Fig. 5-1e, the σ_{12} is always quantized to $e^2/2h$, independent of the external magnetic field, which was attributed to an “electrical short” by the superconductor across the QAH insulator. In other words, the total resistance is the series of two separate QAH regions, each with resistance of h/e^2 , resulting a total conductance of $e^2/2h$.

5.2 QAH-SC and QAH-normal metal devices

To explore the origins about the above experimental discrepancy, more detailed studies are needed to understand the transport properties of QAH insulator. Here, we fabricated QAH-Nb hybrid devices using similar method as [108]. The process steps and a device image are shown in Fig. 5-2a. Starting with MBE grown 6 QL Cr-BST QAH insulator film, 0.5 mm by 0.5 mm Hall bars are fabricated by hard mask and dry etch, then a 100 nm thick Nb strip was deposited by magnetron sputtering with shadow mask made from aluminum foil covering on top of QAH Hall bars. Fig. 5-2b shows a schematic resistance measurement setup, where R_{xx} , R_{xy} are measured from the QAH Hall bar on the left, and R_{12} , R_{13} , R_{32} are measured with the Nb bar crossing QAH on the right side. The black arrows indicate the current flow direction. Superconductor Nb quality is characterized on a separate film using four terminal resistance measurements. Fig. 5-2 c-e show the characterization of superconductor Nb film by four terminal

resistance measurements, on a separate film during the same sputtering process. The temperature dependence of resistance (Fig. 5-2 c) shows a superconducting behavior, and the R - T curve under various out-of-plane magnetic field (Fig. 5-2 d) shows a critical temperature $T_c \sim 8.3$ K. The magnetic field dependence at various temperature shows an upper critical field $H_{c2} \sim 4.3$ T at 2K.

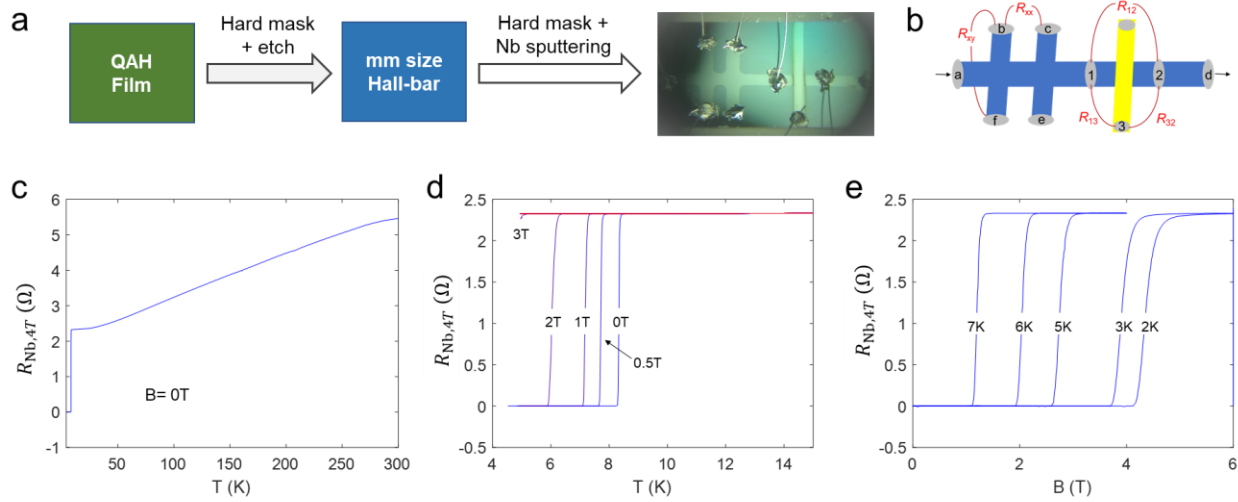


Figure 5- 2 Device fabrication and resistance characterization of superconductor Nb. (a) The process flow to fabricated QAH-SC hybrid devices and an image of a real device. (b) The schematic of the device and resistance measurement setup, where the QAH quality is characterized by the Hall bar structure on the left side. Superconductor Nb quality is characterized using four terminal resistance measurements. (c, d) The R - T curve reveals $T_c \sim 8.3$ K at zero magnetic field. (e) Magnetic field dependence of R at various temperature shows $H_{c2} \sim 4.3$ T at 2K.

To better address the possible non-Majorana trivial interpretations of the $\sigma_{12} = 0.5 e^2/h$ plateaus, theoretically discussed in [110, 111], we have also fabricated the QAH-normal metal (NM) hybrid devices by replacing superconductor Nb with Ir, Ti, Mo, and Au with 100 nm thickness. In total, 56 QAH-Nb devices, 14 QAH-Ir devices, 2 QAH-Ti devices and 2 QAH-Mo

devices were made by magnetron sputtering, while 2 QAH-Au devices were made by e-beam evaporator. The devices were first screened at $T=2\text{K}$ in PPMS to characterize the QAH film quality after sputtering process, and then measured at sub-Kelvin region in dilution refrigerators.

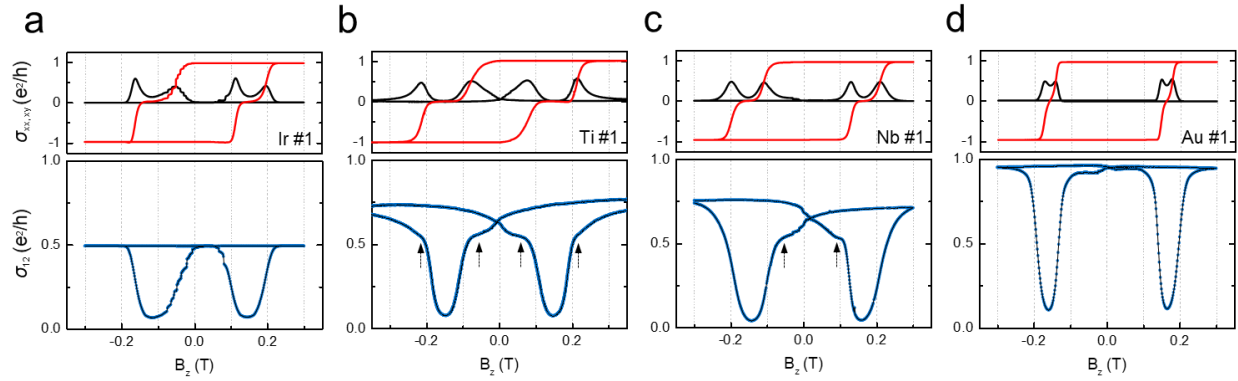


Figure 5- 3 Transport results of quantum anomalous Hall insulator with various metal bars. Longitudinal conductivity σ_{xx} , Hall conductivity σ_{xy} , and longitudinal conductivity σ_{12} ($\sigma_{12} = 1/R_{12}$) of QAH across (a) Ir bar (device Ir #1), (b) Ti bar (device Ti #1), (c) superconducting Nb bar (device Nb #1), and (d) Au bar (device Au #1). All data is taken at $T=50\text{ mK}$.

The transport results of the QAH-Ir, QAH-Ti, QAH-Nb, and QAH-Au devices are shown in Fig. 5-3 a-d, respectively. The perpendicular magnetic field dependence of longitudinal and Hall resistance ρ_{xx} , ρ_{xy} are measured on the QAH Hall bar, and the converted into conductance σ_{xx}, σ_{xy} through the tensor matrix $\sigma_{xx} = \rho_{xx} / (\rho_{xx}^2 + \rho_{xy}^2)$ and $\sigma_{xy} = \rho_{xy} / (\rho_{xx}^2 + \rho_{xy}^2)$ relations. It is shown that, the QAH film remains high quality indicated by σ_{xy} plateaus well quantized at $\pm e^2/h$ and 0, corresponding to the $\mathcal{N} = 2C = \pm 2$ (QAH) and $\mathcal{N} = 0$ (NI) states. The channel conductance σ_{12} of QAH across SC or NM bars is directly converted from channel resistance by $\sigma_{12} = 1/R_{12}$ where R_{12} is in the unit of resistance quanta h/e^2 . For the QAH-Ir hybride device (Fig. 5-3 a), σ_{12} is always quantized at $e^2/2h$ and cannot exceed this value, which is similar to the results reported by [109]. For the QAH-Ti (Fig. 5-3 b) and QAH-Nb (Fig. 5-3 c) devices, the σ_{12}

can get greater than $e^2/2h$ in the QAH phase, and surprisingly the $e^2/2h$ plateaus can be observed near the coercivity in the QAH to NI transition regions as indicated by black arrows, similar to the results reported by [108]. Importantly, these $e^2/2h$ plateaus exist both superconductor Nb devices and normal metal Ti devices, which indicates the observation of half conductance plateau may not related to superconductivity. In addition, QAH-Mo devices also shows the similar results to QAH-Ti devices but are not presented here in order to have a more clear comparison among different cases in Fig. 3-9. For the QAH-Au devices (Fig. 5-3 d), σ_{12} can also exceed $e^2/2h$ and almost quantized at e^2/h , but no half conductance plateau were observed near the magnetic transition. This behavior, is actually similar to the two-terminal conductance of a bare QAH film.

5.3 Possible non-Majorana origins of the $1/2$ conductance plateau

The existence of half conductance in non-superconducting normal metal Ti devices, indicates that possible non-Majorana origins might be playing a role. To better understand this, more detailed measurements were carried out on the QAH-Ti devices. Three measurements configurations were studied, as shown in Fig. 5-4 a, with pad 1 and 2 being indium contacts, pad 3 being the Ti bar and the black arrows indicating current flow directions. In the first and second configurations, three terminal resistances are measured, noted as 3-point R_{13} , 3-point R_{32} , respectively. In the third configuration, similar to Fig. 5-2 b, current is applied through the source and drain outside the shown region so four terminal resistances are measured, noted as 4-point R_{13} , R_{32} , R_{12} . The magnetic field dependent 3-point R_{13} (Fig. 5-4 b) and 3-point R_{32} (Fig. 5-4 c) show the same behavior, well quantized at one resistance quanta h/e^2 , which is a typical behavior of a QAH section.

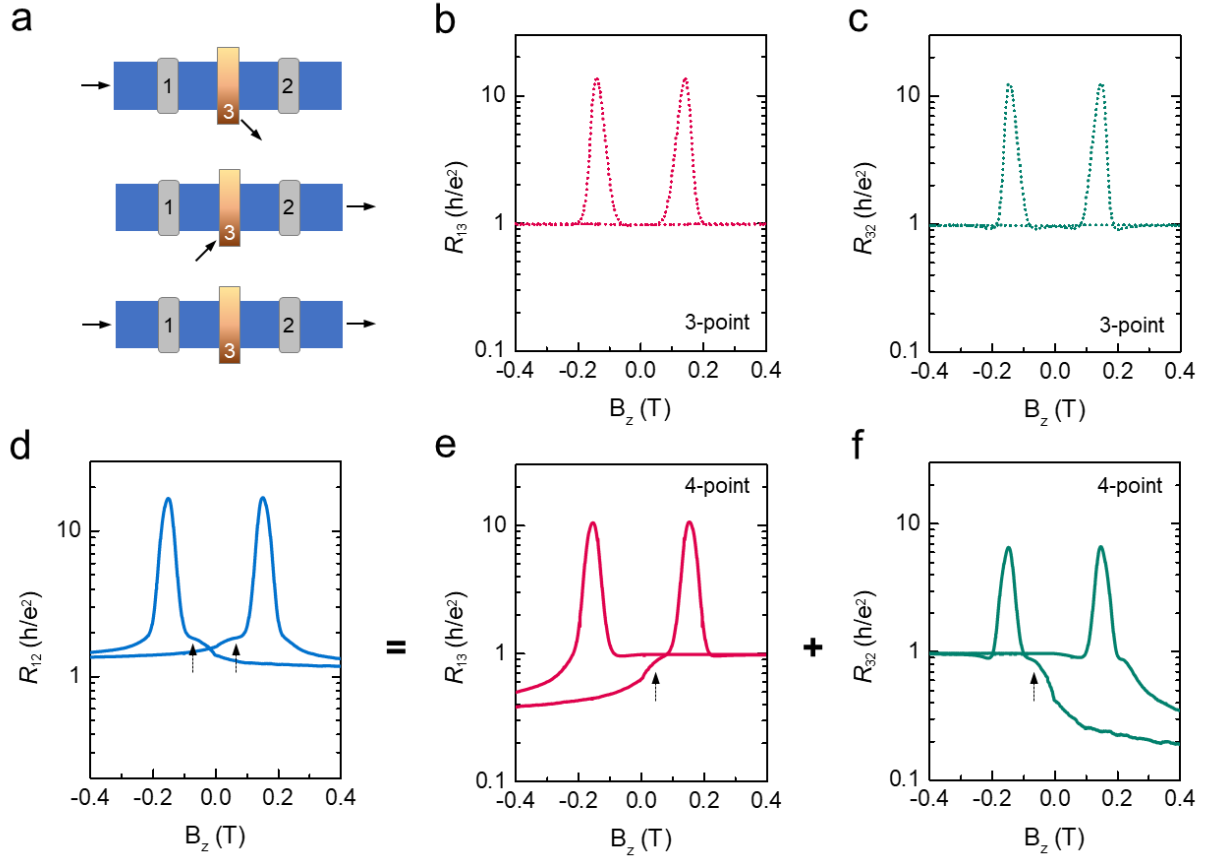


Figure 5- 4 Half-integer longitudinal conductance plateau in QAH with normal metal Ti bar. a. schematic of three-point resistance measurement and four-point resistance measurement, where the arrow stands for current flow direction. b, c. three-point resistance of R_{13} and R_{32} show symmetric field dependence with quantized value of h/e^2 . d. longitudinal resistance R_{12} across Ti bar, where the resistance hump marked by black arrow correspond to half-integer σ_{12} plateau. e, f. four-point resistance of R_{13} and R_{32} show asymmetric field dependence with humps labeled by black arrows. All data is taken at 50mK from device Ti #1.

In the four terminal measurements, however, both 4-point R_{13} (Fig. 5-4 e) and 4-point R_{32} (Fig. 5-4 f) show an asymmetric behavior, with different polarities. The 4-point R_{12} in Fig. 5-4 d equals to the sum of 4-point R_{13} and 4-point R_{32} , and is the row data from which σ_{12} in Fig. 5-3 b

is converted. Ideally, all the 4-point R_{13} , R_{32} , R_{12} should be symmetric with magnetic field, if all the three pads are in good contact with QAH film. The total contact resistance in the QAH regime can be expressed as $R_C = R_{C,upper} + R_{metal} + R_{C,lower}$ where $R_{C,upper}$ and $R_{C,lower}$ are the contact resistance between metal bar and upper or lower QAH edge channel, and R_{metal} is the resistance of the metal bar itself. “Good contact”, in other words, means the pads are able to electrically short the upper and lower edge channels (i.e. contact resistance $R_c \ll h/e^2$) to form an equal potential region. Judging from the symmetry of 4-point R_{13} , R_{32} , and R_{12} , it can be concluded that indium pads 1 and 2 are in “good contact” with QAH while Ti pad 3 is not (see later discussion). In addition, by comparing Fig. 5-4 d with Fig. 5-3 b, the half conductance plateau actually comes from the resistance “plateaus” in Fig. 5-4, indicated by black arrows. The resistance “plateaus” in 4-point R_{12} are further found to be the sum of two separate “plateaus” in 4-point R_{13} and R_{32} , near the magnetization transition region, indicated by the black arrows.

The different transport results can be explained by the different contact resistance conditions between metal bars to QAH insulator, as illustrated in Fig. 5-5. According to the Landauer Büttiker formula that previously discussed in Chapter 2.3, the conductance of a quasi-1D system is related to the reflection coefficient R in the form of [112]:

$$\sigma = \frac{e^2}{h} \frac{1-R}{R} \quad (5-1)$$

First, as shown in Fig. 5-5 a, when the metal bar (pad 3) is in good contact ($R_c \ll h/e^2$) with QAH insulator, the reflection coefficient R can be approximated to be 50% when the dissipationless chiral edge channel meets the metal bar. As a result, the electric potential distribution can be obtained, and the equal potential zones are separated by black dashed lines in Fig. 5-5 a. Here, only the scenario that QAH insulator is fully magnetized along $+z$ direction is

shown. Accordingly, for the R_{12} or σ_{12} measurements, the signal would be from the series connected two QAH sections, and the corresponding signature of σ_{12} matches well with the results of QAH-Ir device Ir #1, as shown in Fig. 5-5 b (adopted from Fig. 5-3 a for better comparison). Second, as shown in Fig. 5-5 c, when the metal bar is in bad contact ($R_c \gg h/e^2$) with QAH insulator, the reflection coefficient R would be close to 0. In other words, the edge channel will not “see” the metal bar. As a result, the σ_{12} signal would be from the one bare QAH section, and this matches well with the results of QAH-Au device Au #1, as shown in Fig. 5-5 d (adopted from Fig. 5-3 d).

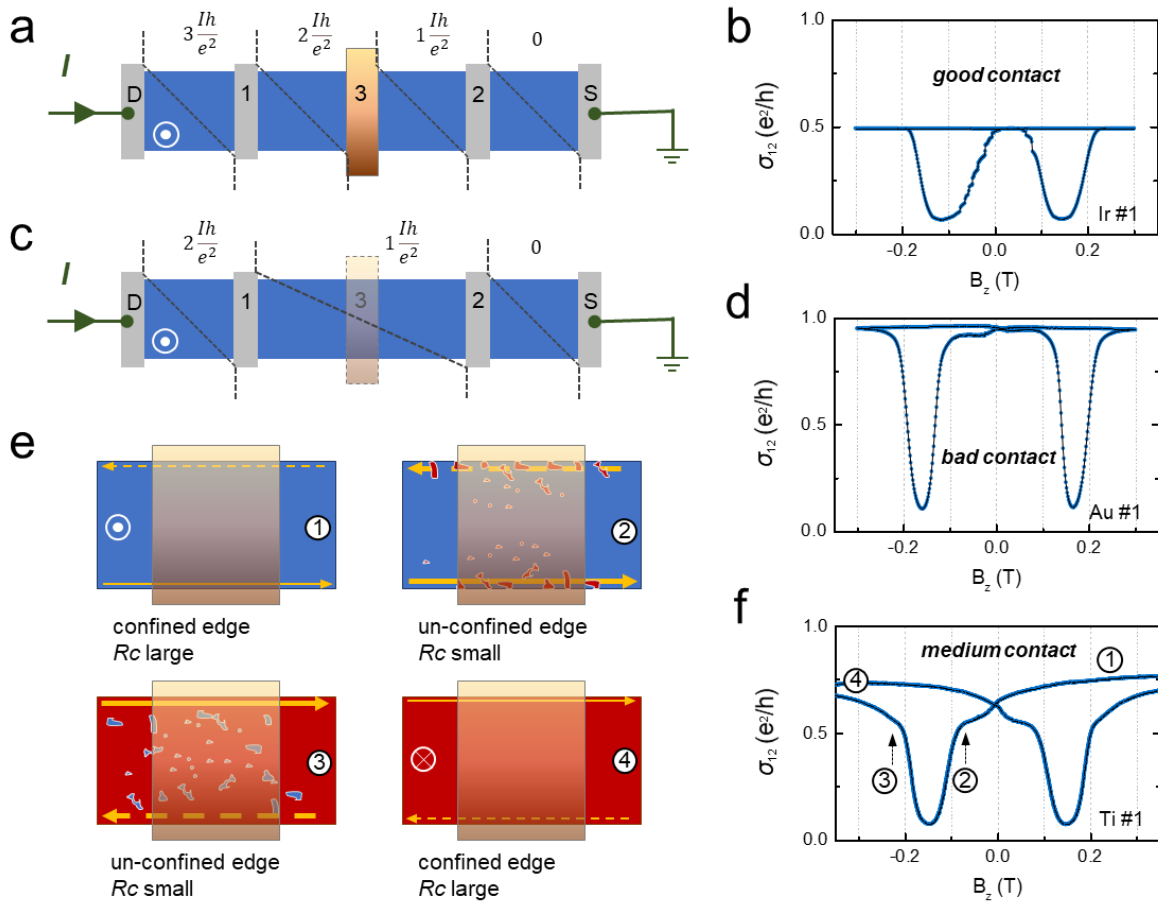


Figure 5- 5 Explanation of Half-integer longitudinal conductance plateau by contact resistance condition. (a) The schematic of potential distribution when the metal bar is in good

contact (contact resistance $R_c \ll h/e^2$) with QAH insulator from Landauer Büttiker theory, and (b) the corresponding signature of σ_{12} for device Ir #1. (c) The schematic of potential distribution when the metal bar is in bad contact ($R_c \gg h/e^2$) with QAH insulator, and (d) the corresponding signature of σ_{12} for device Au #1. (e) The schematic of the evolution of contact resistance with magnetic field sweeping when the metal bar is in medium contact with QAH insulator and (f) the corresponding signature of σ_{12} for device Ti #1.

Fig. 5-5 e shows the third case, where the metal bar is in medium contact (R_c comparable to h/e^2) with QAH insulator, and R_c varies depending on the magnetization hysteresis. Three assumptions are made in the following analysis: 1. The quality of QAH insulator underneath metal bars (pad 3) are not as good as the QAH film in outer regions, as the sputtering process may introduce defects and damages. 2. At the beginning of magnetization switching of Cr-BST, the reversed domains tend to generate at the defect pinning centers and sample edges. 3. The total contact resistance between 1D chiral edge channels and metal bars decreases, with the increase of effective edge channel numbers or width. The four sub-figures in Fig. 5-5 e represent four steps during a magnetization switching from $+z$ to $-z$, which are also labeled in the corresponding σ_{12} results of QAH-Ti device Ti #1 in Fig. 5-5 f (adopted from Fig. 5-3 b).

In step 1, where Cr-BST is fully magnetized along $+z$, the whole sample is in a single domain state thus the chiral edge channels are confined near the sample edge, causing the R_c relatively large ($R \rightarrow 0$ in equation 5-1). As a result, σ_{12} can exceed $e^2/2h$ and approach to e^2/h , similar to the second case mentioned in Fig. 5-5 c. In step 2, at the beginning of magnetization reversal, reversed magnetic domains start to appear and mostly in the region beneath metal bars. Those domain walls near the sample edge act as additional edge channels contributing to the conduction, thus causing the R_c relatively smaller ($R \rightarrow 0.5$ in equation 5-1). Considering the

first assumption made, the system can be viewed as two QAH in series at this narrow magnetic field window. As a result, σ_{12} tend to have a plateau at $e^2/2h$, similar to the first case mentioned in Fig. 5-5 a. As the magnetic field sweep entered the coercivity field, located between step 2 and 3, the whole sample turns into a normal insulator state, causing σ_{12} close to 0. In step 3, at the end of magnetization reversal, the QAH film outside metal bars almost finished magnetic reversal, while in the region beneath metal bars some original magnetic domains are still pinned by defects. The additional domain walls add to the total contact areas between edge channels and metal bar, causing the R_c relatively smaller. Similar to step 2, a half conductance plateau was generated. Experimentally, the half conductance plateau at step 2 is usually easier to be observed than step 3 [108]. This is because the opposite magnetic domains in step 2 (the beginning of reversal) are more gathered near the sample edge, while in step 3 (the end of reversal) they are not. Only the magnetic domain walls near the edge are able to contribute to the current conduction, thus affecting R_c . In step 4, the whole sample finished the reversal process and fully magnetized along $-z$. Similar to step 1, σ_{12} will exceed $e^2/2h$ and approach to e^2/h . As a result, we conclude that the $1/2$ conductance plateau may be a result of magnetic field dependent “medium” contact condition, rather than TSC origins, and this intern channel conduction path may be from directly electrical short, or the percolation effect thorough the magnetic domain walls [110, 111].

5.4 Ultra-wide $1/2$ conductance plateau in another device

In addition, we would like to report the observation of an ultra-wide conductance plateau perfectly quantized at $e^2/2h$ in another QAH-Nb hybrid device (noted as Nb #2). The magnetic field dependence of R_{12} , R_{xy} , and σ_{12} measured at various temperatures (base $T= 50$ mK) are shown in Fig. 5-6 a, b, c, respectively. The device shows good QAH quality since the R_{xy} is well

quantized at h/e^2 ($\approx 25.812 \text{ k}\Omega$) in Fig. 5-6 b. Surprisingly, an ultra-wide resistance plateau at $2h/e^2$ (Fig. 5-6 a) and thus conductance plateau at $e^2/2h$ (Fig. 5-6 b) were observed. This feature exists in a wide temperature range up to 600 mK. Uniquely, this σ_{12} plateau was precisely quantized at $e^2/2h$, even though it was not well quantized at e^2/h ($\approx 0.9 e^2/h$) in the fully magnetized regions. However, the plateaus were only observed in the inner edge of magnetic hysteresis. The large magnetic field dependence of σ_{12} was further investigated, as shown in Fig. 5-6 d. A gradual decrease of σ_{12} with large magnetic field was observed, which is similar to the large field result reported in [108]. However, it is not sure whether this behavior is related to the suppression of superconductivity under high magnetic field, because intuitively a rather “sudden” change should be expected when reaching H_{c2} .

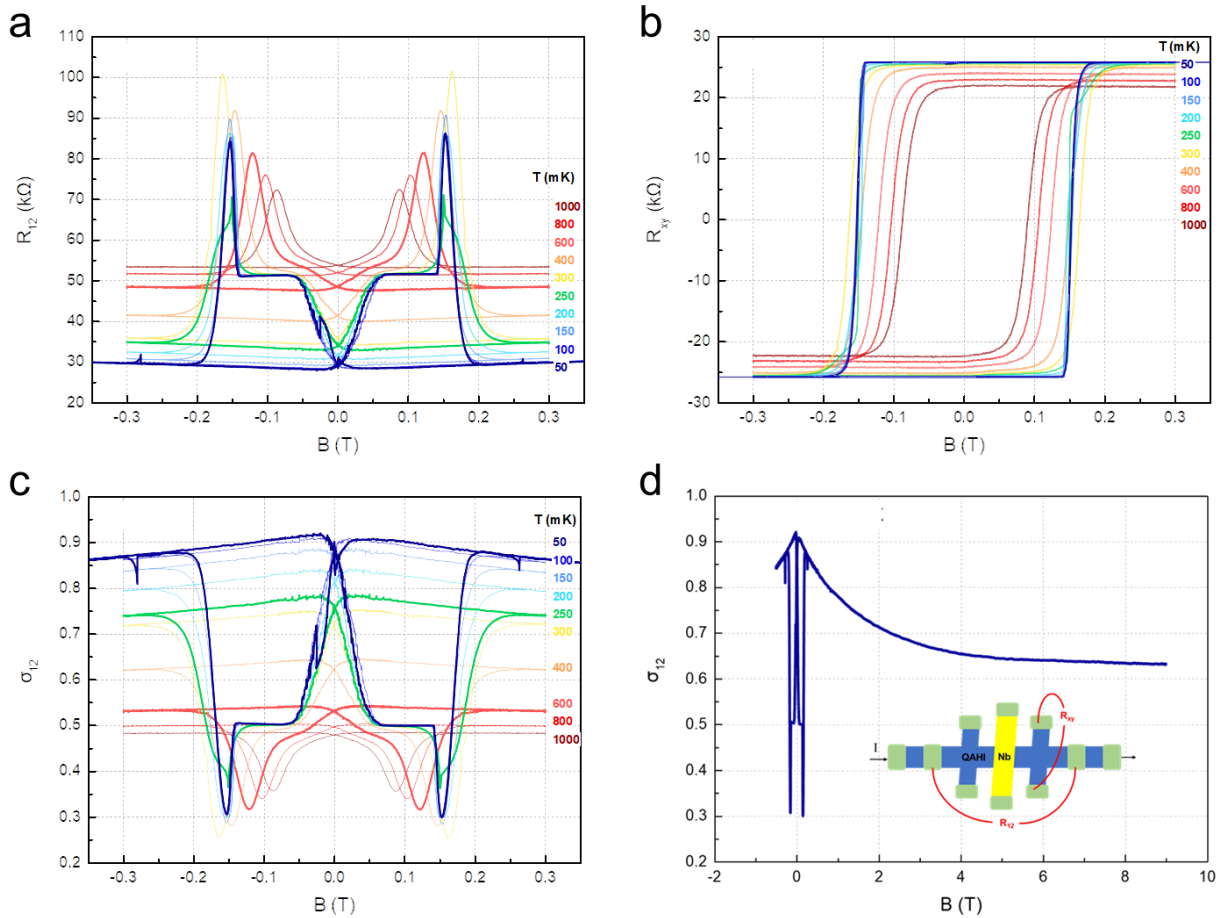


Figure 5- 6 Another QAH-superconductor device Nb #2 shows an ultra-wide $\frac{1}{2}$ conductance plateau. (a) The magnetic field dependence of QAH resistance R_{12} across Nb bar and (b) Hall resistance R_{xy} at various temperatures. (c) The σ_{12} ($1/ R_{12}$) as a function of the magnetic field shows an ultra-wide conductance plateau located perfectly at $0.5 e^2/h$. (d) The σ_{12} as a function of high external magnetic field.

This unique result, being much different from the previously discussed ones, may not be applied to the trivial explanation discussed in Fig. 5-5. Yet this result was only observed in one device (Nb #2) and couldn't be reproduced in all the other devices. Therefore, further explorations are needed to address the details of material characteristics, interface, and detection methods, before a conclusive claim or exclusion of CMEMs should be made.

5.5 Summary of chapter 5

In this work, we carried out detailed transport study of QAH hybrid devices with superconductor Nb, normal metal Ir, Ti, Mo, and Au. Three different kinds of transport results were observed, and especially a half quantization conductance plateau, which is a signature of CMEM, was also observed in QAH-normal metal devices. Possible trivial non-Majorana explanations of the half conductance plateau are provided, where a magnetic field dependent “medium” contact condition between metal bar and QAH insulator may play a role. Finally, another QAH-SC device expressed an unique ultra-wide half conductance plateau, which may not originate from the trivial contact explanations. So far, the fabrication of a proper proximity-induced TSC remains a challenge. Therefore, the details of material characteristics, interface, and

detection methods need to be explored in details. More studies are required to fully understand this system, before a drawing conclusive claim or exclusion of CMEMs.

Chapter 6 Collaborative works

In this Chapter, two collaborative works will be introduced. In the first work, aiming to understand the inter-channel scattering and address the possible percolation effect in QAH, we fabricated and carried out a size dependent study on mesoscopic scale QAH devices with sub-micron channel width that is comparable to magnetic domain size. In the second work, enabled by the successful growth of QAH insulator on mica substrate, dual-gate QAH devices were fabricated using the exfoliation and transfer techniques that are commonly used for 2D materials. A topological phase transition induced by electric field was further observed. In addition, the combination of QAH material and techniques used for 2D materials, brings lots of new research opportunities to couple QAH with other interesting 2D materials such as 2D superconductors.

6.1 Size dependence of QAH in mesoscopic scale

Since the discovery of QAH effect, extensive efforts have been taken to understand the dissipation-less chiral edge states. Non-local transport measurements [48, 113, 114] have been carried out to prove the dissipation-less chiral transport property of sample edge and magnetic domain wall, and current breakdown measurements [115] were also reported to understand the dissipation channel of QAH insulator. However, these studies were focusing on macroscopic QAH devices where the chiral edge modes are simply treated as a perfect 1D conductor. To better understand the chiral edge state and possible dissipation channel in QAH, key questions such as the physical location and width of the chiral edge channel need to be addressed.

For potential scalable manufacturing of quantum devices, Cr-doped $(\text{Bi, Sb})_2\text{Te}_3$ stands out as the most suitable platform among available QAH candidates because of its matured

massive production route through molecular beam epitaxy (MBE). However, so far, the experimental efforts have been focusing on macroscopic QAH devices where the chiral edge modes are simply treated as a perfect 1D conductor at the physical boundary of the QAH mesa. The understanding of some key questions such as, where the chiral edge states are physically located, and how wide the chiral edge channel is, remains elusive.

Although the chiral edge conduction channel has been directly visualized through microwave scanning microscopy [116], the several μm wide conductive edge should not be interpreted as the edge channel width but most likely limited by the resolution of the instrumentation. Thus, a comprehensive understanding of mesoscopic transport in sub-micron QAH devices is required to address these questions. In this work, we report a comprehensive investigation of the transport behavior of QAH devices with various channel width from $500 \mu\text{m}$ down to 600 nm . The size-dependence of QAH and geometrical size limit above which the QAH effect can survive will be discussed.

6.1.1 QAH down to sub-micron size

The QAH insulator films are 6 QL $\text{Cr}_{0.12}(\text{Bi}_{0.26}\text{Sb}_{0.62})_2\text{Te}_3$ grown by MBE on semi-insulating GaAs (111) B substrates as described in chapter 2. Two samples with the same growth recipe are prepared in this study, and they can be referred as sample S1 and S2. We have fabricated Hall bar devices with various width. The $500 \mu\text{m}$ wide devices were fabricated by an aluminum hard mask and dry etching method, while $200 \mu\text{m}$, $100\mu\text{m}$, and $50 \mu\text{m}$ devices were fabricated by photolithography. All devices with these four widths were fabricated on sample S1. We further fabricated mesoscopic devices with channel width $<10 \mu\text{m}$ on sample S2 with the help of electron beam lithography. The sample was first patterned into a $10\text{-}\mu\text{m}$ wide Hall bars using photolithography, then the narrow channels were further defined with electron beam

lithography. An optical image and a false-colored scanning electron microscopy image of representative devices are shown in Fig. 6-1 a and 6-1 b. To reveal size dependent transport behaviors, a set of four Hall bar devices with channel width of 5 μm , 3 μm , 1.5 μm , and 0.6 μm were fabricated.

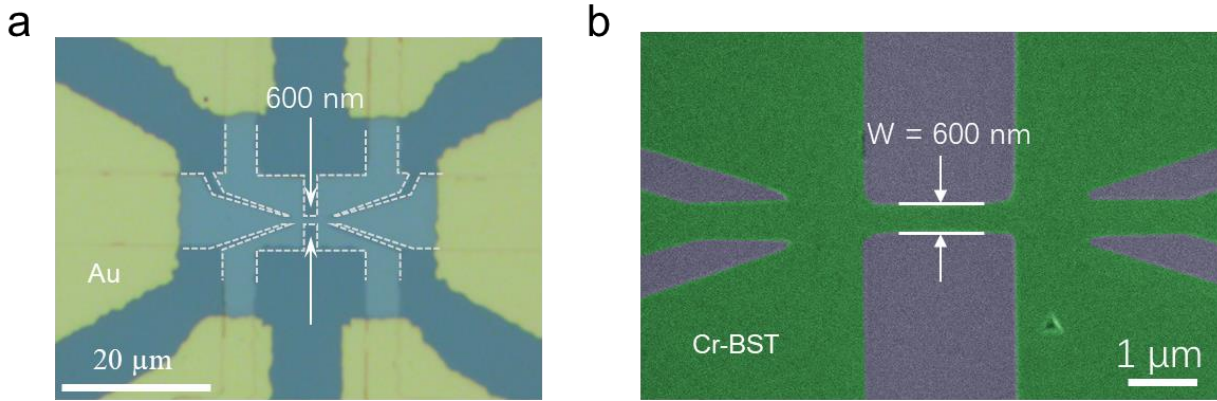


Figure 6- 1 QAH devices with sub-micron size fabricated by the hybrid method of photolithography and E beam lithography. (a) optical microscope and (b) TEM image of the device with channel width of 600nm.

The longitudinal resistivity ρ_{xx} (red curve) and Hall resistivity ρ_{xy} (blue curve) of all the eight devices measured at 100 mK are presented in Fig. 6-2. Here, low AC current excitation of 10 nA (500 μm , 200 μm , 100 μm , and 50 μm devices), 1 nA (5 μm and 3 μm devices), and 0.5 nA (1.5 μm and 0.6 μm devices) were used, to avoid the current heating effect and transverse electric field breakdown (see discussion in sub-section 3.1.2). It is shown that, depending on the magnetization directions, the Hall resistivity ρ_{xy} is fully quantized at $\pm h/e^2$ for all the devices. The longitudinal resistance ρ_{xx} shows a vanishing value when in quantized states, and a resistance peak near the coercive field H_c , corresponding to trivial insulating states during magnetic domain switching.

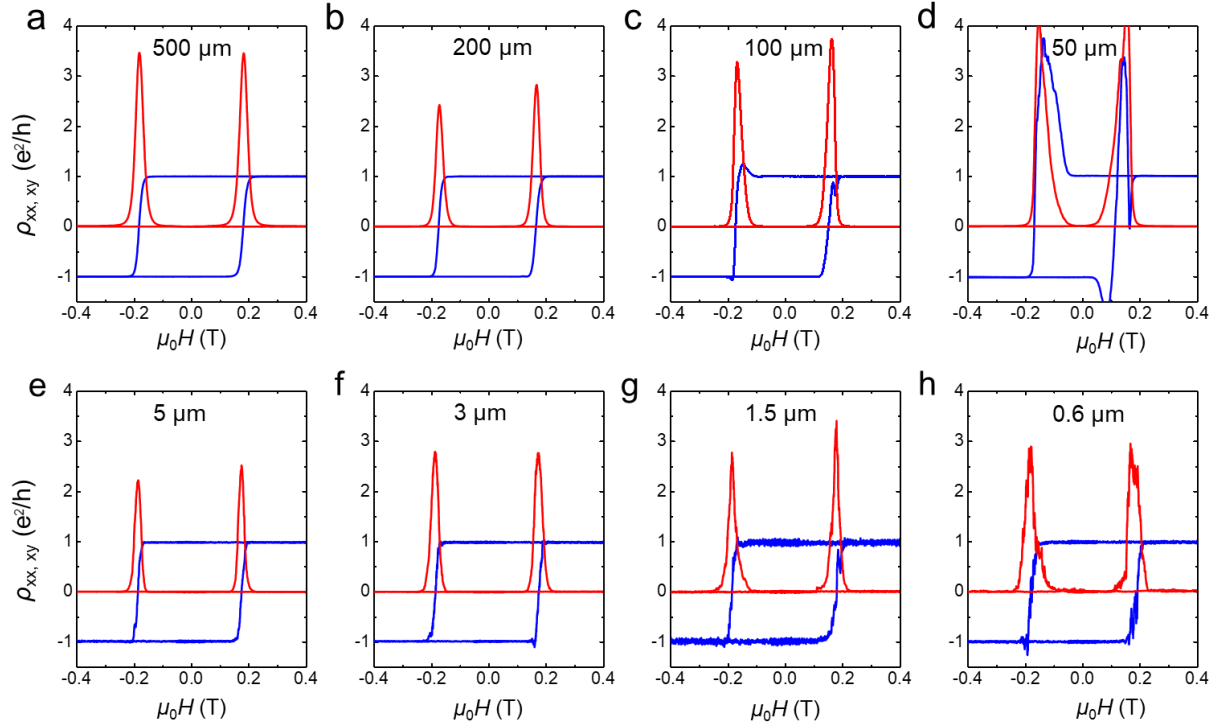


Figure 6- 2 ρ_{xx} and ρ_{xy} of QAH devices with various sizes measured at 100K. (a)-(h) Longitudinal and Hall resistance of all devices shows good quantization with channel width from 500um down to 600nm.

Therefore, we conclude that the general features of the QAH insulators are preserved in all devices with width ranging from 500 μm down to 600 nm. This is the first demonstration of QAH effect in sub-micron size device in the Cr-BST material system, which is below the direct imaged edge conduction [116] and estimated edge state localization length [115] of few micrometers.

6.1.2 Size dependence of QAH

In order to make a more comprehensive comparison of the QAH behavior of devices with different sizes, we carried out the temperature dependence measurements. Fig. 6-3 shows the longitudinal resistivity ρ_{xx} (a-h) and Hall resistivity ρ_{xy} (i-p) of all the eight devices measured at

various temperature ranging from 100 mK to 1 K. The longitudinal conductivity σ_{xx} and transverse conductivity σ_{xy} are converted through the tensor matrix $\sigma_{xx} = \rho_{xx} / (\rho_{xx}^2 + \rho_{xy}^2)$ and $\sigma_{xy} = \rho_{xy} / (\rho_{xx}^2 + \rho_{xy}^2)$ and plotted in Fig. 6-4 accordingly, where the signatures of QAH states is again confirmed. It is shown that, at 100 mK, the converted σ_{xx} is approaching to zero and σ_{xy} are fully quantized at $\pm e^2/h$, which is originated from integer topological invariant *i.e.*, Chern number $C = \pm 1$ of the system. The σ_{xy} in Fig. 6-4 also shows an intermediate state $\sigma_{xy} = 0$ near the coercive field H_c , as a result of the matrix tensor conversion of the resistance peak, which represents the trivial insulating states during magnetic domain switching.

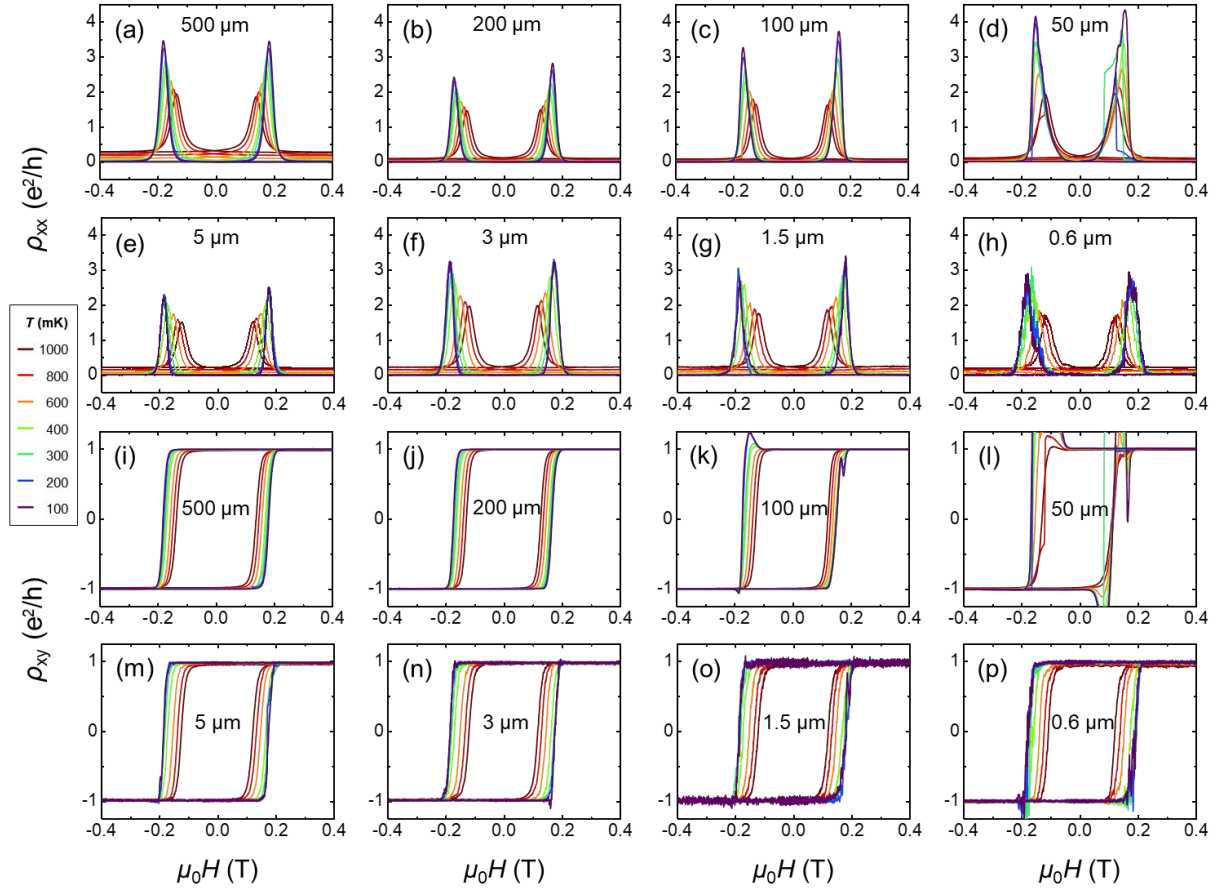


Figure 6- 3 σ_{xx} and σ_{xy} of QAH devices with various sizes measured at different temperatures. (a)-(h) Longitudinal and (i)-(p) Hall resistance of devices with channel width

from 500um down to 600nm.

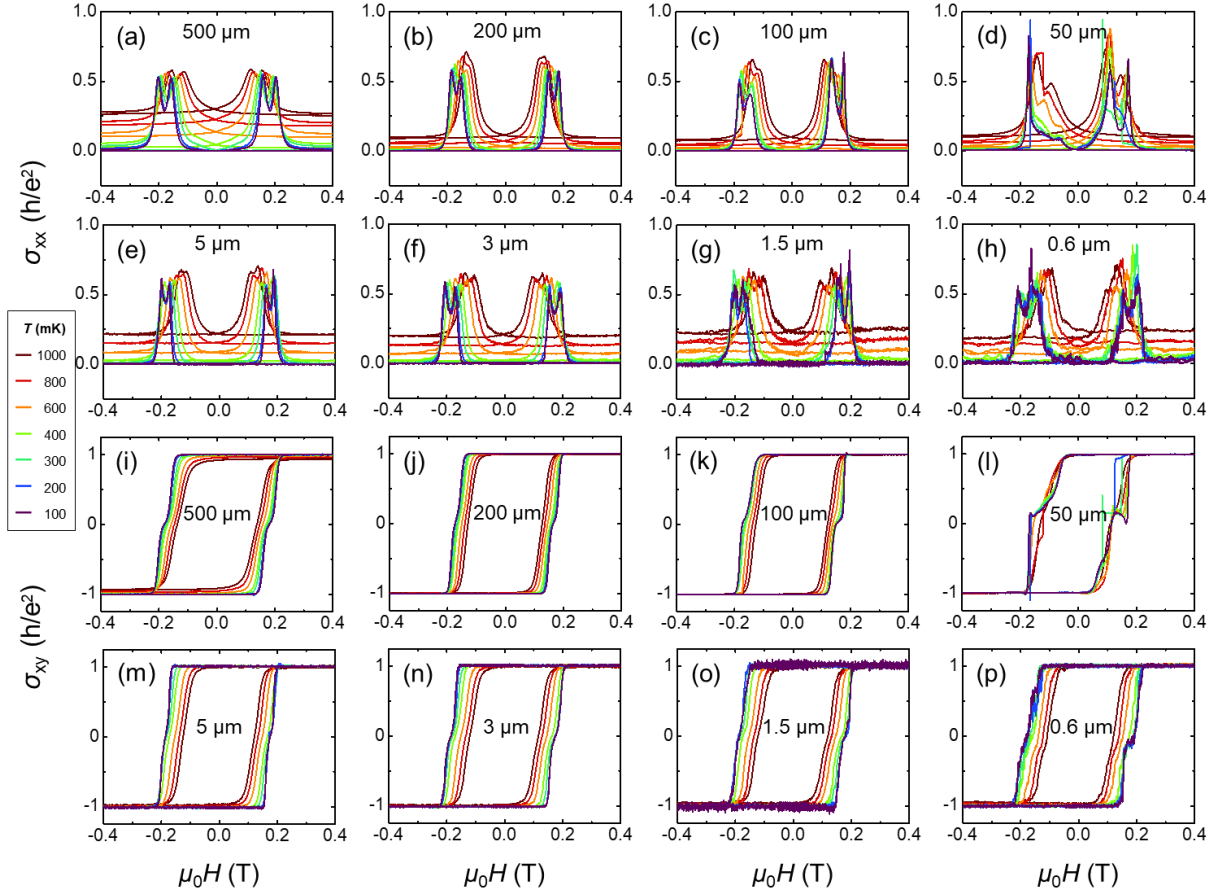


Figure 6- 4 Transport result of QAH devices with various sizes measured at different temperatures. (a)-(h) Longitudinal and (i)-(p) Hall conductance of devices with channel width from 500um down to 600nm.

As shown in Fig. 6-3 and Fig. 6-4, while Hall resistivity ρ_{xy} and conductance σ_{xy} can keep good quantization in a wide temperature range, the remnant longitudinal resistance ρ_{xx} starts to increase with the increase of temperature, which can be seen more obviously in the plot of σ_{xx} . This increase of remnant ρ_{xx} or σ_{xx} is interpreted as the involvement of additional dissipative channels, which might be contributed from variable range hopping due to in-gap

states [115], thermally activated bulk carriers [117-119], and quasi-helical non-chiral edge transport due to the un-gapped side surface [113, 120].

The remnant ρ_{xx} of all devices under an external magnetic field 400 mT ($> H_c$) are summarized in Fig. 6-5 a. where the x -axis is the Hall bar width. There are two major observations: First, the 500 μm hard mask made device shows a much larger remnant ρ_{xx} compared to 200 μm , 100 μm and 50 μm devices made by photolithography from the same sample. This is because there is an inevitable air gap between the aluminum hard-mask and sample surface, causing potential edge damage or degradation during the etching process. On the contrary, for devices fabricated by photolithography, the photo resist is in close contact to sample surface, thus the edge region remains intact during the etching process. Second, for the devices fabricated by photolithography or e-beam lithography, the remnant resistance increases for devices with smaller sizes, when it's in the QAH region (low temperature range). This phenomenon becomes more obvious when comparing within the mesoscopic devices (5 μm , 3 μm , 1.5 μm and 0.6 μm).

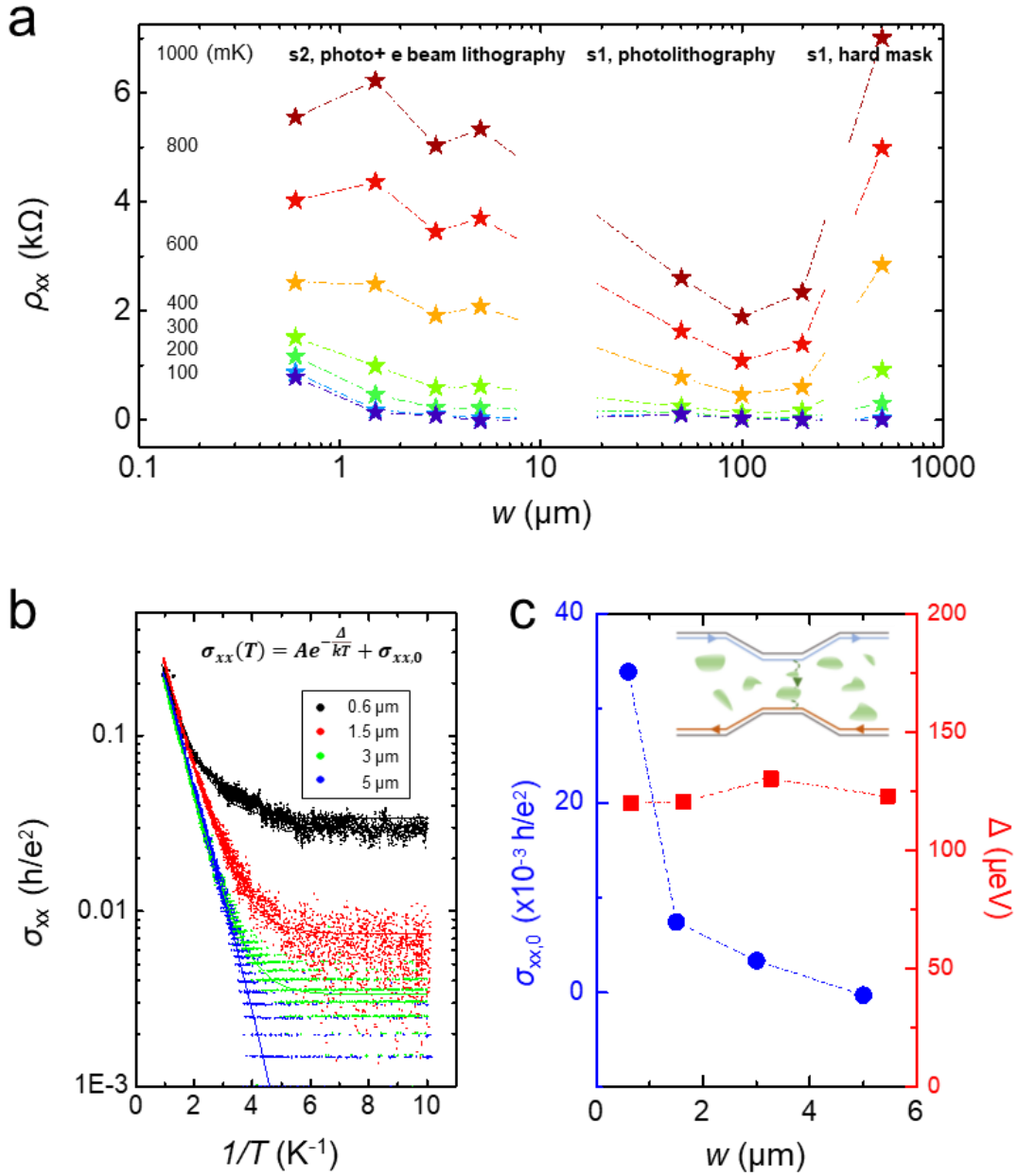


Figure 6- 5 Summary of the size dependence of QAH quality. (a) Longitudinal resistance versus channel width measured at various temperatures. (b) The longitudinal conductance versus $1/T$ during the field cooling. By fitting the data using a thermal activation relationship with a constant offset, the activation gap size and remanence conductance can be obtained, summarized in (c).

The converted remnant conductance σ_{xx} for all four mesoscopic devices during field cooling are shown in an Arrhenius plot in Fig. 6-5 b. At high temperatures, σ_{xx} drops exponentially with $1/T$ at the same decaying rate for all four sizes of devices, suggesting a bulk thermal activation gap independent of size dominates in this temperature regime. At low temperatures, the resistance saturates at a certain value, indicating a dissipative channel that originates from a temperature independent mechanism. The activation gap can be extracted by fitting the data with the following equation:

$$\sigma_{xx}(T) = A \exp\left(-\Delta/k_B T\right) + \sigma_{xx,0} \quad (6-1)$$

where Δ is the activation gap or surface magnetization gap, k_B is the Boltzmann constant, A is a device-dependent constant, and $\sigma_{xx,0}$ describes the remnant conduction from additional dissipative channels. The extracted average activation gap and remnant conduction are plotted in Fig. 6-5 c. It is shown that the activation gap is around $120 \mu\text{eV}$, and no obvious correlation with the geometric size can be drawn. On the other hand, the remnant conductance $\sigma_{xx,0}$ increases monotonically with reduced size, suggesting a back-scattering mechanism is introduced despite topological protection when the width of the channel is reduced. However, since the width of the narrowest device is still considerably larger than the Fermi wavelength, the direct overlapping of wave functions of chiral edge states on the opposite boundary is unlikely. Instead, we believe this is most likely due to the inter-channel electrons scattering through percolative tunneling with the assistance of random 2D puddles in the energy landscape as shown in the inset of Fig. 6-5 c.

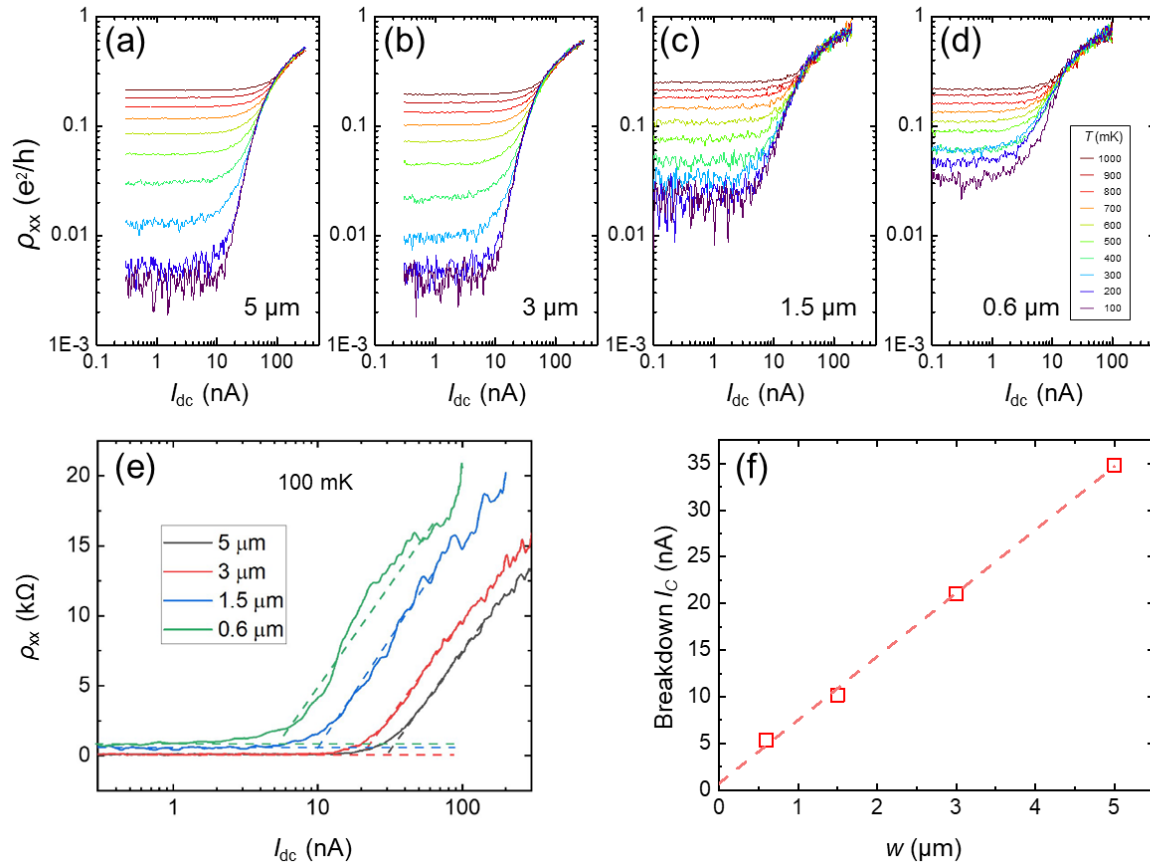


Figure 6- 6 Size dependence of the current induced breakdown of QAH. (a)-(d) Longitudinal resistance dV/dI versus DC current intensity of the four devices measured at various temperature. (e) plotting the dV/dI for four devices measured at 100mK together. (f) The extracted breakdown current I_c versus channel width.

In addition, the QAH critical current was also measured in these devices using DC+AC current bias. A large DC current bias is sent through the device along with a fixed small AC excitation down to 0.2 nA, and the differential resistance was measured by a synchronized lock-in amplifier. The differential ρ_{xx} as a function of DC current bias at various temperature for all the four mesoscopic devices are shown in Fig. 6-6 a-d, respectively. It can be seen that at low DC bias, the remnant differential ρ_{xx} is irrelevant to I_{dc} but only determined by the previously

mentioned back-scattering mechanism. When DC current bias exceed a critical value which is the breakdown current I_c , the resistance begins to shoot up, as large current drives the system out of QAH states, which is attributed to the electric-field-driven percolation in the transverse direction [121]. It is also shown that, the devices show higher breakdown current at higher temperature, and all curves at various temperature merge together when further increase DC bias. This is because at large DC bias region, the breakdown of QAH is dominated by current rather than thermal effects. The differential resistance as a function of DC bias at 100mk for all devices are plotted together in Fig. 6-6 e, and their breakdown current is extracted in Fig. 6-6 f. It shows that the breakdown current scales linearly with the channel width, which also supports the argument of electric-field driven break-down of QAH [121].

6.1.3 Summary of chapter 6.1

As a conclusion, in this work we presented a detailed study on the transport behavior of QAH insulators with various size down to the sub-micron regime. QAH signatures, including vanished longitudinal resistance and quantized Hall resistance, are well preserved in narrow-channel devices down to 600 nm. The monotonic increase of the remnant conductance $\sigma_{xx,0}$ with reduced size suggests an inter-channel back-scattering through percolative tunneling with the assistance of random 2D puddles in the energy landscape. This is further evident by the current break-down measurements, where breakdown current scales linearly with the channel width, suggesting the electric-field driven break-down of QAH, consistent with the strong electric-field dependence of percolative tunneling process.

6.2 Manipulation of QAH Through Electric Field

Though the magnetic field controlled exchange bias could offer great capability to manipulate the topological quantum phases, full electrical control of topological quantum phase transition is of greater interest for the application of functionalized dissipationless quantum electronics such as topological transistors [122]. In a gated MTI device, the electric gate has two distinct functionalities. First, it serves as a direct method to inject charge carriers into the MTI thus tuning its fermi level position. Second, it introduces an external perpendicular electric field across the device through which the topological and magnetic states of the MTI can be controlled, suggested by theoretical calculations by Wang et al. [123]. However, the latter effect is usually small in energy scale compared to other effects. As a result, in order to study the electric field controlled phenomenon, the carrier dependent effects need to be ruled out. Motivated by this, we conduct a research study on dual gated MTI devices, where the two degrees of freedom (electric field and carrier density) can be individually tuned.

6.2.1 MBE growth of QAH quality Cr-BST on MICA

In order to fabricate the dual gated MTI devices, we need to search for proper substrates for the MBE growth other than commonly used thick GaAs or Sapphire substrates. Muscovite mica with a stoichiometry of $\text{KAl}_2(\text{Si}_3\text{Al})\text{O}_{10}(\text{OH})_2$ is a layered material that is commonly used for van der Waals epitaxy [124]. It is a highly insulating, transparent, and flexible material, which is of great advantages to study the optical properties and strain effects of its epilayer. Most importantly, its layered structure allows the exfoliation protocol as widely implemented in graphene and 2D materials [125], and its high dielectric constant makes it a great candidate as the bottom gate dielectric material.

Followed by the procedures shown in table 2-1, we were able to growth high quality Cr-BST films on 100 μm -thick mica substrates, as evidenced by the streaky RHEED patterns (Fig. 6-

7 a) and RHEED intensity oscillations (Fig. 6-7 b) during the growth. Fig. 6-7 a inset shows an image of the as grown 6QL Cr-BST film on a mica sheet after cleaning backside indium glue. Some curve textures can be seen because the 2cm-by-2cm surface contains several discontinuous stages, which is common because of peeling off the top surface for a clean growth surface. A 1mm by 0.5mm Hall bar device was fabricated by using hard mask and dry etch method for quick transport measurement. Fig. 6-7 c shows the field dependence of longitudinal sheet resistance ρ_{xx} (blue) and Hall resistance ρ_{xy} (red) measured at $T= 100$ mK. Surprisingly, the quantized ρ_{xy} and almost vanished ρ_{xx} shows the realization of QAH effect on 6QL Cr-BST film grown on mica substrates, for the first time.

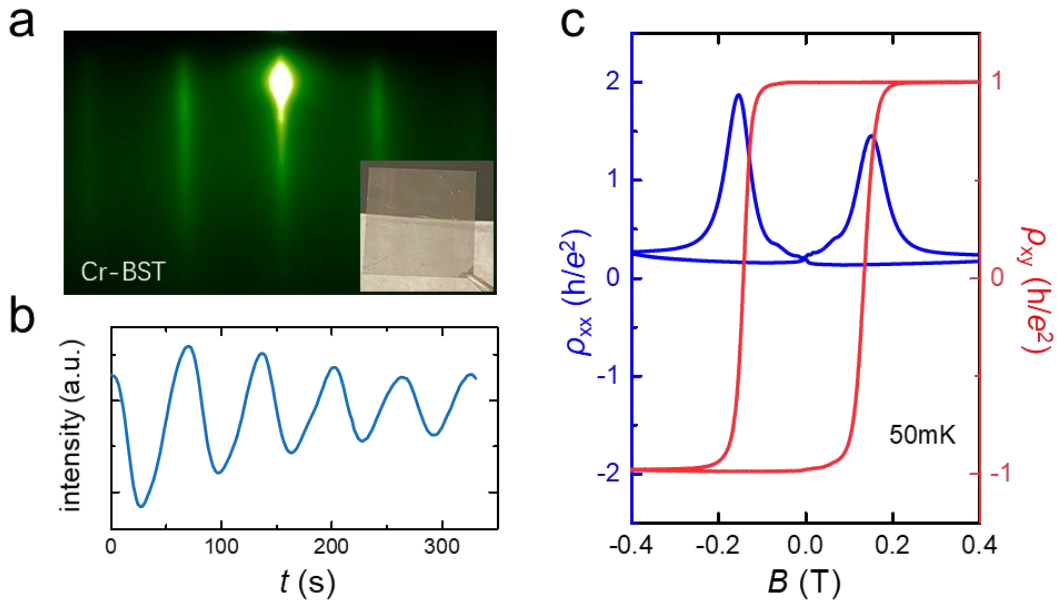


Figure 6- 7 MBE growth of QAH quality Cr-BST on MICA. (a) RHEED pattern of as grown Cr-BST on MICA and an image of the film. The streaky RHEED patterns and RHEED oscillations in (b) show high quality layer-by-layer mode growth. (c) shows the transport measurement results on a millimeter size Hall bar device. A quantized Hall resistance and

vanishing longitudinal resistance in (e) indicated the Cr-BST film grown on MICA can host QAH effect.

6.2.2 Dual-gated QAH devices

We then developed a dry transfer scheme to fabricate the CBST dual-gated device, as shown in Fig. 6-8 a. First, a large piece of graphite on SiO₂ substrate was prepared, and then the as grown Cr-BST/mica was exfoliated with mica thickness down to ~20 nm and transferred onto the graphite bottom gate contact. Second, the film was patterned into a 10 μm by 10 μm Hall bar device using photolithography and dry etching. Third, The Cr/Au contacts were fabricated through another photolithography and etching process. Finally, an exfoliated thin mica sheet ($t \sim 20$ nm) and graphite were transferred onto the device to form the top gate. Fig. 6-8 b shows the optical microscopic image of a dual-gated device. Fig. 6-8 c shows schematics of the various layers, and the measurement scheme we employed to trigger the electric field effect on QAH insulator.

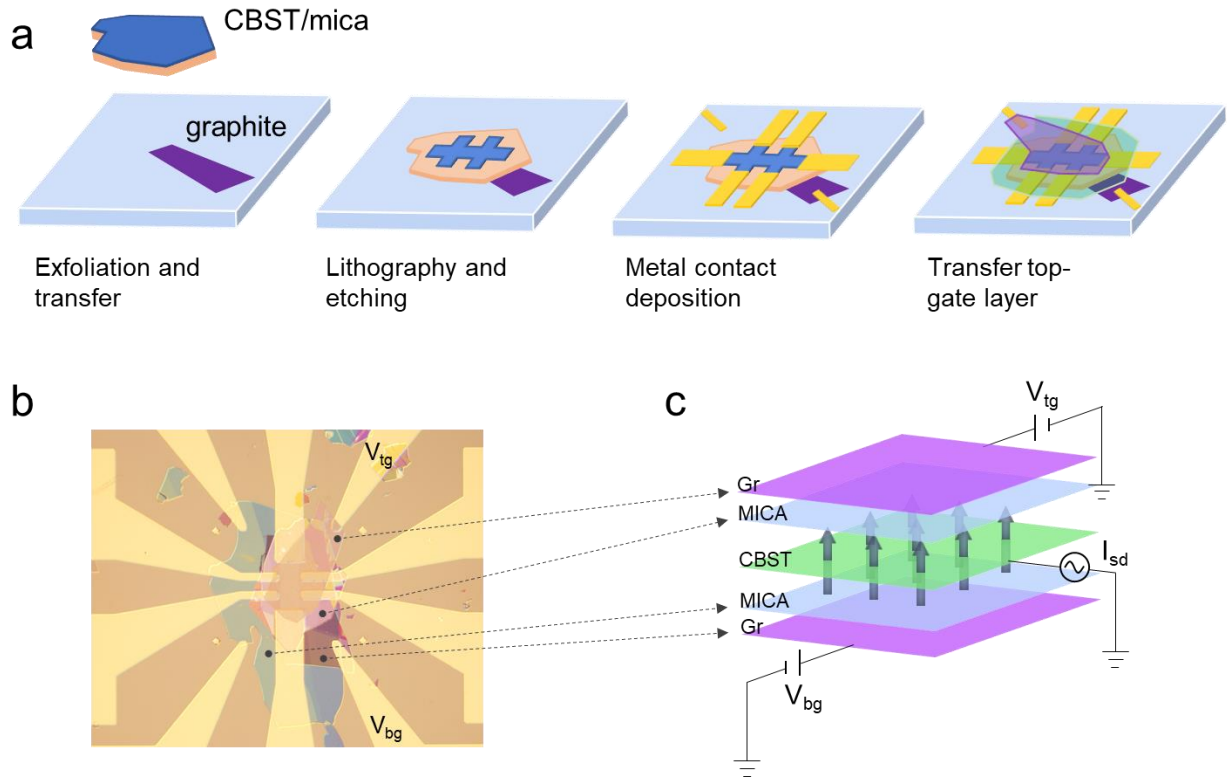


Figure 6- 8 Fabrication process of dual-gated QAH devices. (a) Starting from the exfoliation and transfer of as grown CBST/mica onto graphite bottom electrode, the CBST film was patterned into Hall bar devices by photolithography and etching. Metal contacts was formed, and then top dielectric mica was transferred on top of the device. Finally, a graphite acting as top electrode was transferred on the top and connected to Metal contact. (b) Optical image of a 6QL Cr-BST Hall bar device in a dual-gated configuration. (c) A schematic of the device structure and measurement scheme for the dual-gated MTI, with each layer corresponding to its location in (b).

We carried out the transport measurement down to 100 mK to see the gate responses. Fig. 6-9 shows the longitudinal resistance R_{xx} and Hall resistance R_{xy} as a function of top-gate voltage V_{tg} at various temperatures, with bottom gate fixed at $V_{bg}=0V$. Both the R_{xx} and R_{xy}

show strong gate dependence, indicating a wide tunability range. The QAH effect is shown to survive in a wide range of gate voltage, with an optimized $V_{tg}=+10V$ for this device.

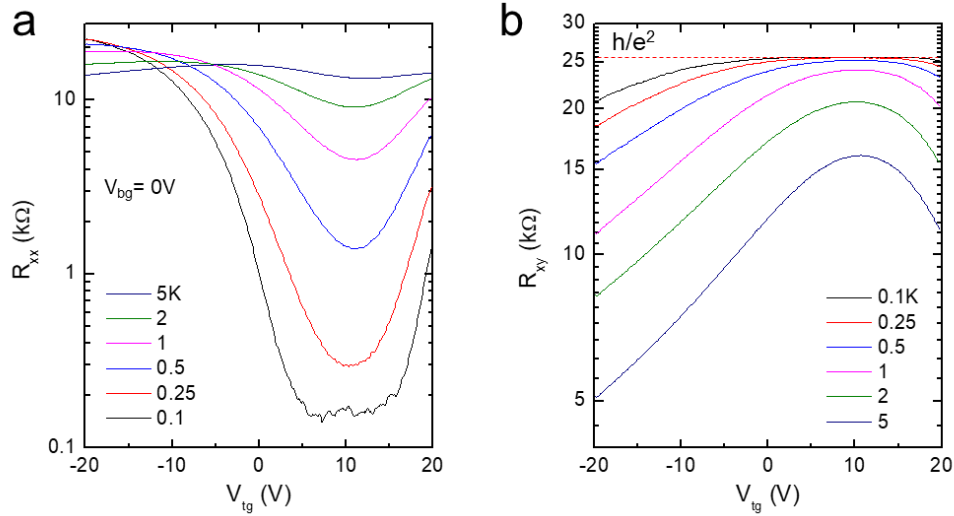


Figure 6- 9 Single top-gate response of the QAH device. (a) R_{xx} and (b) R_{xy} curves as a function of top-gate voltage for the 6QL CBST sample measured at various temperatures with the magnetic field fixed at 0.5 T.

After successfully demonstrating QAH effect and the functionality of both top and bottom gates independently, we carried out the dual gate measurement. The quality of our dual-gated device is again verified by the high-quality dual-gate mapping as presented in Fig. 6-10, where the R_{xx} , R_{xy} taken at 500mK and 1K, respectively. From the color maps, the Cr-BST film reaches a quantization in R_{xy} of h/e^2 (25.8 k Ω) as the dual-gate voltages tune to a global R_{xx} minimum, confirming the QAH state. Unlike a single gate, which introduces electric field and charge carriers simultaneously, the dual-gate measurement is able to control them independently. The elongated R_{xx} minimum along the diagonal of the dual-gate map (Fig. 6-10 a arrow direction) indicates an electric field acting to the thin Cr-BST film. On the other hand, along the

direction perpendicular to the arrow, only carrier density is playing a role while electric field is unchanged.

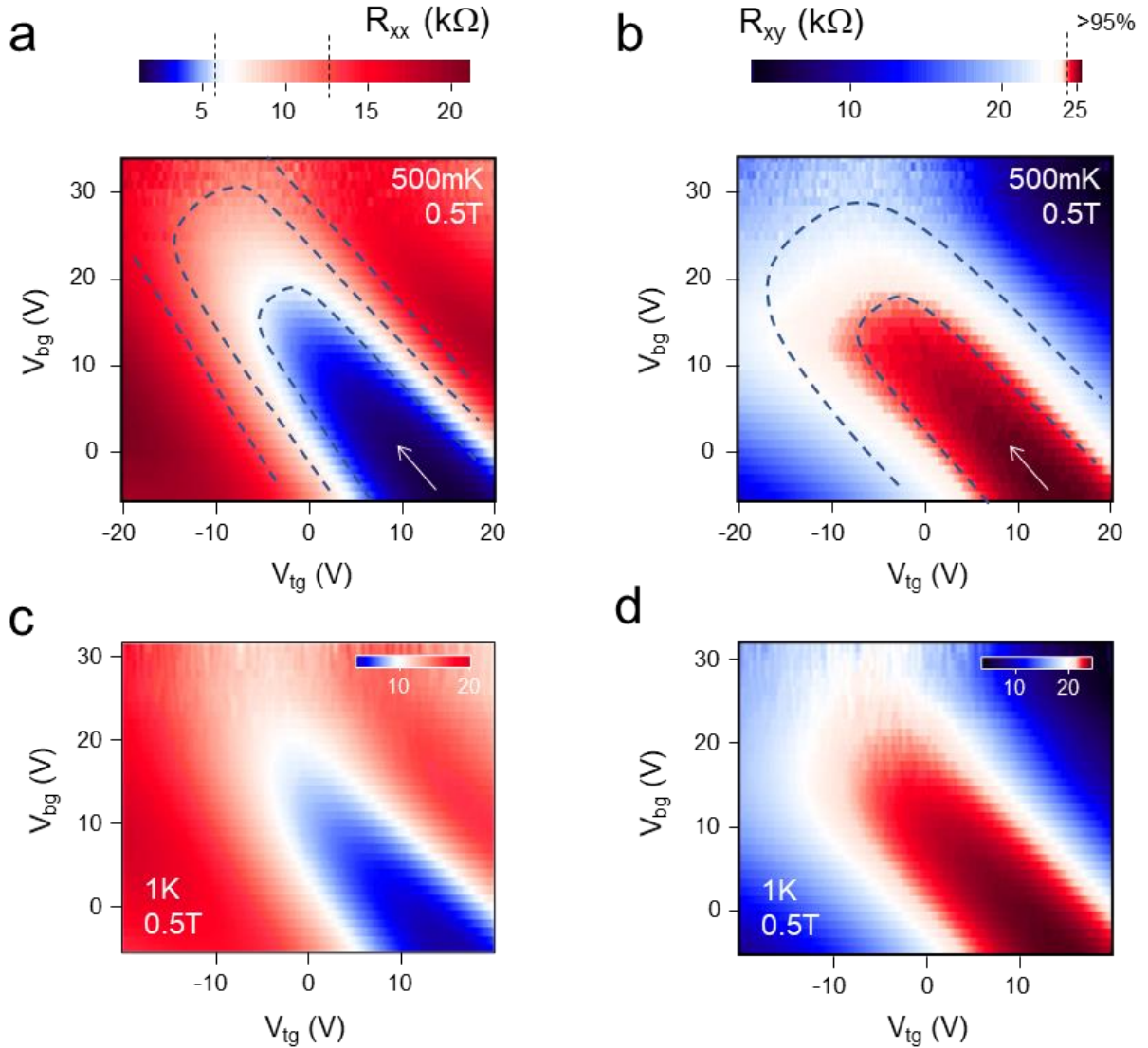


Figure 6- 10 Dual-gate response of the QAH device. 2D color maps of (a) R_{xx} and (b) R_{xy} as a function of dual-gate voltages for the Cr-BST device measured at temperature and magnetic field of 500 mK and 0.5T, respectively. The same 2D color maps of (c) R_{xx} and (d) R_{xy} taken at 1K.

6.2.3 Electric field induced topological quantum phase transition

To analyze this effect, we convert the dual-gate voltages into the displacement field (D)-charge density (n) function using the relations:

$$D = \left(\frac{\epsilon_r}{\epsilon_0}\right)\left(\frac{\Delta V_{bg}}{d^b} - \frac{\Delta V_{tg}}{d^t}\right) \quad (6 -2)$$

$$n = (C_b \Delta V_{bg} + C_t \Delta V_{tg}) \quad (6 -3)$$

where ϵ_r is dielectric constant of mica, d^b and d^t are the thickness of bottom gate mica and top gate mica, C_b and C_t are the capacitance of bottom gate and top gate, ΔV_{bg} and ΔV_{tg} are relative gate voltages referred to the optimized gate position (center point of the QAH region).

The Hall resistance hysteresis under various displacement field and carrier density are shown in Fig. 6-11. With the increasing displacement field applied on the sample, there is an obvious drop of Hall resistance, while coercivity keeps the same. With introduction of charge carriers, the fermi level shifts outside the surface magnetic gap (QAH activation gap), resulting in the decrease of Hall resistance. In addition, an increase of coercivity can be observed with the increase of carrier density, which is more pronounced for p-type hole doping, indicating a carrier mediated magnetization mechanism.

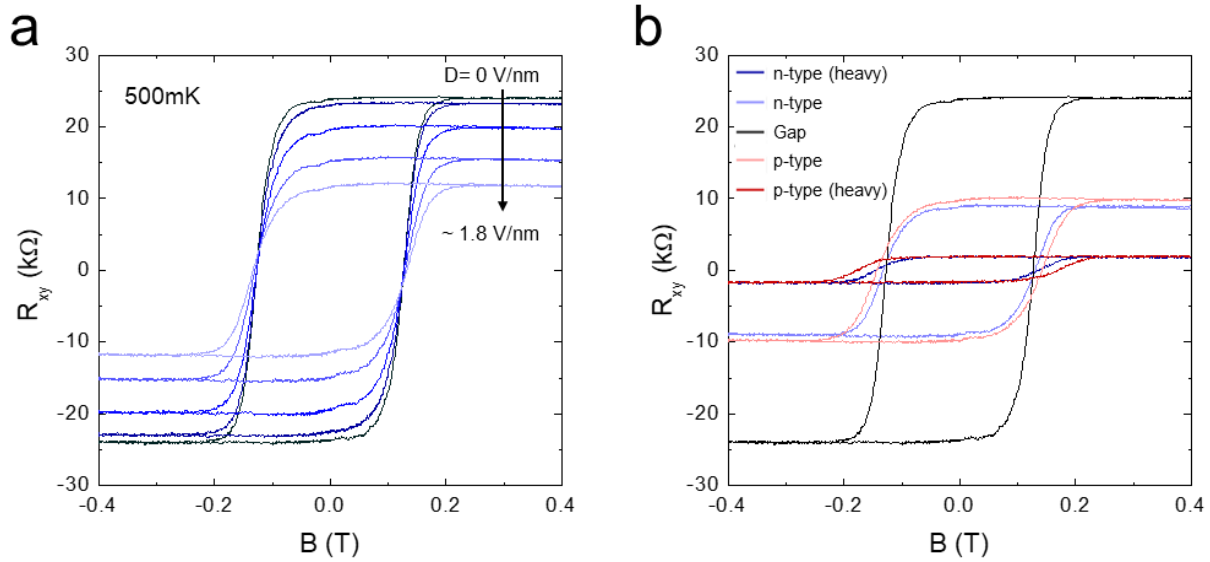


Figure 6- 11 Electric field and carrier dependence. (a) R_{xy} – B curve under various electric displacement field. (b) R_{xy} – B curve under various carrier doping.

We further conducted the dual-gate measurements at various temperatures and summarized the displacement field dependence of longitudinal resistance ρ_{xx} and Hall resistance ρ_{xy} in Fig. 6-12. As shown in Fig. 6-12 a, the ρ_{xx} - D curves taken at different temperatures converge at $D_c \sim 1.9$ V/nm and slowly diverge at higher D , indicating a metal ($D < D_c$) to insulator ($D > D_c$) phase transition, which is related to a gap closure and reopening processes mediated by the electric field. A suppression of the Hall signal by electric field can also be seen in Fig. 6-12 b, which is due to the reduction of magnetic exchange coupling (J_{ex}) by electric field (see later discussion). The ρ_{xy} - D curves also show a trend of converging together but not reaching the critical point yet.

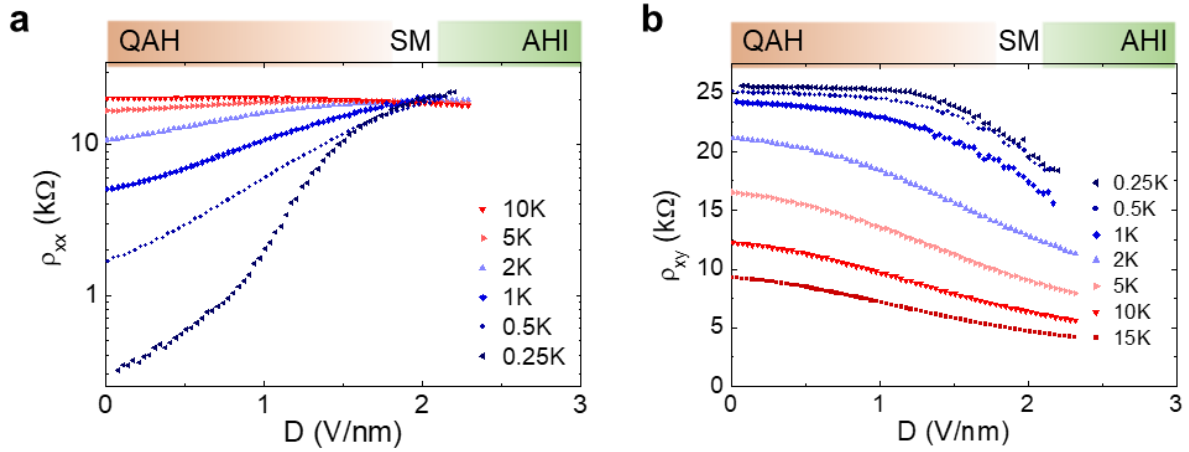


Figure 6- 12 Electric field induced topological quantum phase transition. (a) ρ_{xx} and (b) ρ_{xy} as a function of displacement field (D) extracted at different temperatures.

Fig. 6-13 a shows the ρ_{xx} - T curves measured at different D with 0.5T constant magnetic field applied. Thermal activation energy Δ can be extracted from by a linear fitting of the $\log(\rho_{xx})$ to T^{-1} , similar to Equation (6-1). As shown in Fig. 6-13 b, Δ drops with D and reaches zero when $D > D_c$, indicating a gap closing by electric field. The suppression of thermal-activation behavior is consistent with the predicted electric field-induced topological quantum phase transition [123], which can be explained by the band structure evolution in electric field as depicted in Fig. 6-13 c.

In the QAH regime, the magnetic exchange energy (E_{ex}) due to the surface band splitting for opposite spins is greater than the top and bottom inter-surface hybridization gap (Δ_h), and thus the gap lies in the inverted regime. With the apply electric field, the E_{ex} shrink slowly as the magnetic exchange coupling (J_{ex}) reduces due to the reduction of spin susceptibility and magnetic anisotropy [123, 126]. Meanwhile, the electric field can also shift the top and bottom surface band oppositely due to the structure inversion asymmetry [127]. These cause the

competition between the E_{ex} and Δ_h . At sufficient electric field, the surface bands with opposite spin states cross at their band edges and results in the gap closing, leading to the converging ρ_{xx} signature as we observed in Fig. 6-12 a. As a result, electric field turns the system into an anomalous Hall insulator (AHI) phase with a trivial insulating gap. If further increase electric field, a ferromagnetic to paramagnetic magnetic quantum phase transition is predicted to occur, where the sample changes from AHI phase into a normal insulator (NI) phase [123]. However, we didn't see this AHI to NI magnetic quantum phase transition because it requires a much higher electric field, which can be also inferred from Fig. 6-12 b.

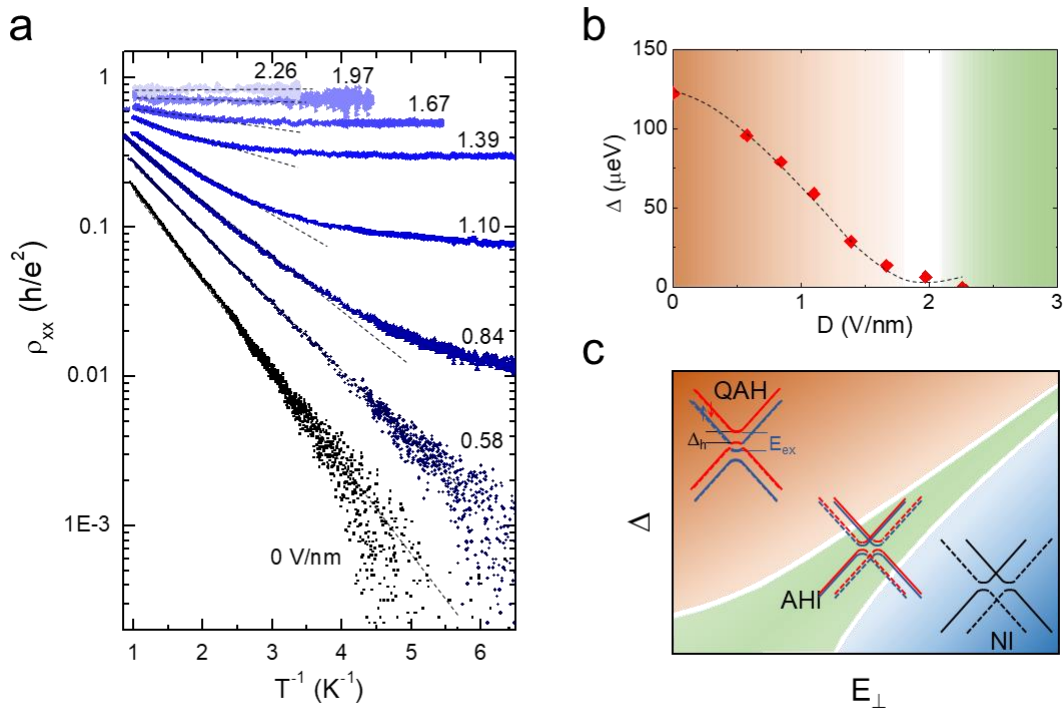


Figure 6- 13 Electric field induced closing of surface magnetic gap. (a) ρ_{xx} -temperature at different D. (b) Plot of the thermal activation gap (Δ) as a function of D calculated from the ρ_{xx} -temperature curves. (c) Topological phase diagram for a MTI in an external perpendicular electric field (E_{\perp}). Insets are the surface band structures in the different topological phases as

labeled.

6.2.4 Thickness-dependent surface bands evolution

In addition, we also carried out the thickness dependent study to see the topological surface states evolution. 8QL, 10QL, and 12QL QAH insulator films were also prepared, and dual-gate devices were fabricated. The dual-gate response for all thickness were measured at 2K, and the 2D color maps of R_{xx} are shown in Fig. 6-14. As mentioned for 6QL device, the elongated R_{xx} minimum along the diagonal of the dual-gate indicates an electric field acting to the thin Cr-BST film. This feature becomes less obvious in 8QL film, and fully disappear in 10QL and 12QL films. This means, as the sample becomes thicker the top gate and bottom gate tend to be tuning the top layers and bottoms layers only. In other words, the gate cannot fully penetrate through the films, so the method of electric field and carrier density coordinate becomes no longer valid. This is also in consistence with the fact that, the top and bottom topological surface states become decoupled as the film goes into 3D region when it reaches 10QL [48].

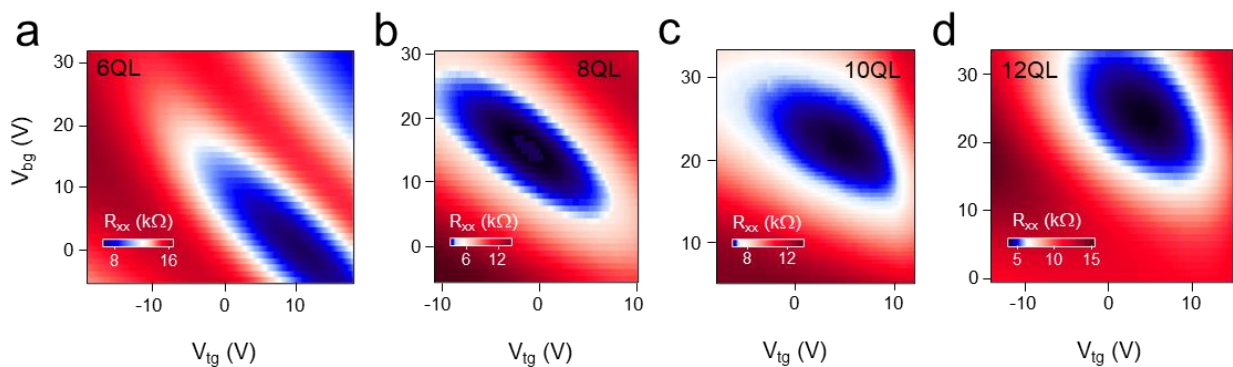


Figure 6- 14 Thickness dependent dual-gate response. 2D color maps of (a) R_{xx} and (b) R_{xy} as a function of top-gate voltage and bottom-gate voltage of the 6QL CBST measured at 2K.

6.2.5 Summary of chapter 6.2

we achieved high quality epitaxial growth of Cr-BST on mica sheet. We fabricated dual-gating QAH devices and demonstrated an electric field control of topological quantum phase transition. Our works may facilitate the application of functionalized dissipationless quantum electronics.

In summary, we successfully realized high quality Cr-BST epitaxial growth on mica substrate, and fabricated well-functioning dual-gate devices. We demonstrate the electric field control of the topological quantum phase transition between the topological non-trivial QAH state and trivial gapped AHI state. The device and measurement scheme can also be implemented to other exotic quantum phases such as axion insulator [58, 69, 70] and high Chern number QAH systems [90] to achieve electrical control of different topological phases.

Chapter 7 Conclusion and Perspectives

In this dissertation, we first introduced the MBE techniques and demonstrated the capability of growing high quality MTI thin films to realize QAH effect. We have also discussed the fine-tuning effort to enhance QAH observation temperature and the successful transfer of QAH recipe onto various substrates. In Chapter 3, we introduced a thickness dependent study on MTI sandwiched structures and addressed the different origins of the zero-Hall conductance plateau in QAH insulator and axion insulator. A minor loops measurement was utilized to distinguish the zero-Hall conductance plateau in the two systems, and their temperature scaling analysis result in different critical components. In Chapter 4, we studied the QAH insulator and antiferromagnetic heterostructures. We show the coupling between MTI and uncompensated AFM insulator Al-Cr₂O₃ leads to an exchange biased QAH effect and it can be effectively controlled by a field training process. In Chapter 5, we focus on the QAH insulator and superconductor heterostructures which was believed to host chiral Majorana edge mode. QAH insulator with superconductor Nb and normal metals hybrid devices were measure carefully to understand the debate of recent experimental reports on chiral Majorana fermions. A possible non-Majorana origin of the half-quantized conductance plateau was described, and the important role of interface details was addressed. In Chapter 6, two collaborative works will be introduced. Mesoscopic scale QAH insulator devices were fabricated to probe the size limit of QAH effect, and detailed size dependent study were carried out to understand the inter-channel scattering in QAH. The development of QAH insulator growth on mica substrates allow us to fabricate dual-gate QAH devices using exfoliation and transfer techniques, and an electric field induced topological quantum phase transition was demonstrated.

References

- [1] X.-L. Qi, T. L. Hughes, and S.-C. Zhang, "Topological field theory of time-reversal invariant insulators," *Physical Review B*, vol. 78, 2008.
- [2] M. Z. Hasan and C. L. Kane, "Colloquium: Topological insulators," *Reviews of Modern Physics*, vol. 82, pp. 3045-3067, 2010.
- [3] X.-L. Qi and S.-C. Zhang, "Topological insulators and superconductors," *Reviews of Modern Physics*, vol. 83, pp. 1057-1110, 2011.
- [4] J. Sinova, D. Culcer, Q. Niu, N. A. Sinitsyn, T. Jungwirth, and A. H. MacDonald, "Universal intrinsic spin Hall effect," *Phys Rev Lett*, vol. 92, p. 126603, Mar 26 2004.
- [5] B. A. Bernevig, T. L. Hughes, and S. C. Zhang, "Quantum spin Hall effect and topological phase transition in HgTe quantum wells," *Science*, vol. 314, pp. 1757-61, Dec 15 2006.
- [6] M. König, S. Wiedmann, C. Brune, A. Roth, H. Buhmann, L. W. Molenkamp, *et al.*, "Quantum spin hall insulator state in HgTe quantum wells," *Science*, vol. 318, pp. 766-70, Nov 2 2007.
- [7] I. Knez, R. R. Du, and G. Sullivan, "Evidence for helical edge modes in inverted InAs/GaSb quantum wells," *Phys Rev Lett*, vol. 107, p. 136603, Sep 23 2011.
- [8] S. Wu, V. Fatemi, Q. D. Gibson, K. Watanabe, T. Taniguchi, R. J. Cava, *et al.*, "Observation of the quantum spin Hall effect up to 100 kelvin in a monolayer crystal," *Science*, vol. 359, pp. 76-79, Jan 5 2018.
- [9] L. Fu, C. L. Kane, and E. J. Mele, "Topological insulators in three dimensions," *Phys Rev Lett*, vol. 98, p. 106803, Mar 9 2007.
- [10] L. Fu and C. L. Kane, "Topological insulators with inversion symmetry," *Physical*

- Review B*, vol. 76, 2007.
- [11] D. Hsieh, D. Qian, L. Wray, Y. Xia, Y. S. Hor, R. J. Cava, *et al.*, "A topological Dirac insulator in a quantum spin Hall phase," *Nature*, vol. 452, pp. 970-4, Apr 24 2008.
- [12] H. Zhang, C.-X. Liu, X.-L. Qi, X. Dai, Z. Fang, and S.-C. Zhang, "Topological insulators in Bi₂Se₃, Bi₂Te₃ and Sb₂Te₃ with a single Dirac cone on the surface," *Nature Physics*, vol. 5, pp. 438-442, 2009.
- [13] Y. Xia, D. Qian, D. Hsieh, L. Wray, A. Pal, H. Lin, *et al.*, "Observation of a large-gap topological-insulator class with a single Dirac cone on the surface," *Nature Physics*, vol. 5, pp. 398-402, 2009.
- [14] Y. L. Chen, J. H. Chu, J. G. Analytis, Z. K. Liu, K. Igarashi, H. H. Kuo, *et al.*, "Massive Dirac fermion on the surface of a magnetically doped topological insulator," *Science*, vol. 329, pp. 659-62, Aug 6 2010.
- [15] D. Hsieh, Y. Xia, D. Qian, L. Wray, F. Meier, J. H. Dil, *et al.*, "Observation of time-reversal-protected single-dirac-cone topological-insulator states in Bi₂Te₃ and Sb₂Te₃," *Phys Rev Lett*, vol. 103, p. 146401, Oct 2 2009.
- [16] J. Zhang, C. Z. Chang, Z. Zhang, J. Wen, X. Feng, K. Li, *et al.*, "Band structure engineering in (Bi(1-x)Sb(x))₂Te₃ ternary topological insulators," *Nat Commun*, vol. 2, p. 574, Dec 6 2011.
- [17] L. A. Wray, S.-Y. Xu, Y. Xia, D. Hsieh, A. V. Fedorov, Y. S. Hor, *et al.*, "A topological insulator surface under strong Coulomb, magnetic and disorder perturbations," *Nature Physics*, vol. 7, pp. 32-37, 2010.
- [18] S.-Y. Xu, M. Neupane, C. Liu, D. Zhang, A. Richardella, L. Andrew Wray, *et al.*, "Hedgehog spin texture and Berry's phase tuning in a magnetic topological insulator,"

- Nature Physics*, vol. 8, pp. 616-622, 2012.
- [19] R. Yu, W. Zhang, H. J. Zhang, S. C. Zhang, X. Dai, and Z. Fang, "Quantized anomalous Hall effect in magnetic topological insulators," *Science*, vol. 329, pp. 61-4, Jul 2 2010.
- [20] X. L. Qi, R. Li, J. Zang, and S. C. Zhang, "Inducing a magnetic monopole with topological surface States," *Science*, vol. 323, pp. 1184-7, Feb 27 2009.
- [21] X. F. Kou, Y. B. Fan, M. R. Lang, P. Upadhyaya, and K. L. Wang, "Magnetic topological insulators and quantum anomalous hall effect," *Solid State Communications*, vol. 215, pp. 34-53, Jul 2015.
- [22] W. Luo and X.-L. Qi, "Massive Dirac surface states in topological insulator/magnetic insulator heterostructures," *Physical Review B*, vol. 87, 2013.
- [23] M. Lang, M. Montazeri, M. C. Onbasli, X. Kou, Y. Fan, P. Upadhyaya, *et al.*, "Proximity induced high-temperature magnetic order in topological insulator--ferrimagnetic insulator heterostructure," *Nano Lett*, vol. 14, pp. 3459-65, Jun 11 2014.
- [24] X. Che, K. Murata, L. Pan, Q. L. He, G. Yu, Q. Shao, *et al.*, "Proximity-Induced Magnetic Order in a Transferred Topological Insulator Thin Film on a Magnetic Insulator," *ACS Nano*, vol. 12, pp. 5042-5050, May 22 2018.
- [25] C. Tang, C. Z. Chang, G. J. Zhao, Y. W. Liu, Z. L. Jiang, C. X. Liu, *et al.*, "Above 400-K robust perpendicular ferromagnetic phase in a topological insulator," *Science Advances*, vol. 3, Jun 2017.
- [26] P. Wei, F. Katmis, B. A. Assaf, H. Steinberg, P. Jarillo-Herrero, D. Heiman, *et al.*, "Exchange-coupling-induced symmetry breaking in topological insulators," *Phys Rev Lett*, vol. 110, p. 186807, May 3 2013.
- [27] F. Katmis, V. Lauter, F. S. Nogueira, B. A. Assaf, M. E. Jamer, P. Wei, *et al.*, "A high-

- temperature ferromagnetic topological insulating phase by proximity coupling," *Nature*, vol. 533, pp. 513-6, May 26 2016.
- [28] C. Lee, F. Katmis, P. Jarillo-Herrero, J. S. Moodera, and N. Gedik, "Direct measurement of proximity-induced magnetism at the interface between a topological insulator and a ferromagnet," *Nature Communications*, vol. 7, Jun 2016.
- [29] L. D. Alegria, H. Ji, N. Yao, J. J. Clarke, R. J. Cava, and J. R. Petta, "Large anomalous Hall effect in ferromagnetic insulator-topological insulator heterostructures," *Applied Physics Letters*, vol. 105, p. 053512, 2014.
- [30] M. Mogi, T. Nakajima, V. Ukleev, A. Tsukazaki, R. Yoshimi, M. Kawamura, *et al.*, "Large Anomalous Hall Effect in Topological Insulators with Proximitized Ferromagnetic Insulators," *Phys Rev Lett*, vol. 123, p. 016804, Jul 3 2019.
- [31] C. Y. Yang, L. Pan, A. J. Grutter, H. Wang, X. Che, Q. L. He, *et al.*, "Termination switching of antiferromagnetic proximity effect in topological insulator," *Sci Adv*, vol. 6, p. eaaz8463, Aug 2020.
- [32] Q. L. He, X. Kou, A. J. Grutter, G. Yin, L. Pan, X. Che, *et al.*, "Tailoring exchange couplings in magnetic topological-insulator/antiferromagnet heterostructures," *Nat Mater*, vol. 16, pp. 94-100, Jan 2017.
- [33] J.-M. Zhang, W. Ming, Z. Huang, G.-B. Liu, X. Kou, Y. Fan, *et al.*, "Stability, electronic, and magnetic properties of the magnetically doped topological insulators Bi₂Se₃, Bi₂Te₃, and Sb₂Te₃," *Physical Review B*, vol. 88, 2013.
- [34] J. M. Zhang, W. Zhu, Y. Zhang, D. Xiao, and Y. Yao, "Tailoring magnetic doping in the topological insulator Bi₂Se₃," *Phys Rev Lett*, vol. 109, p. 266405, Dec 28 2012.
- [35] J. J. Cha, J. R. Williams, D. Kong, S. Meister, H. Peng, A. J. Bestwick, *et al.*, "Magnetic

- doping and kondo effect in Bi_2Se_3 nanoribbons," *Nano Lett*, vol. 10, pp. 1076-81, Mar 10 2010.
- [36] Y. S. Hor, P. Roushan, H. Beidenkopf, J. Seo, D. Qu, J. G. Checkelsky, *et al.*, "Development of ferromagnetism in the doped topological insulator $\text{Bi}_{2-x}\text{Mn}_x\text{Te}_3$," *Physical Review B*, vol. 81, 2010.
- [37] J. G. Checkelsky, J. T. Ye, Y. Onose, Y. Iwasa, and Y. Tokura, "Dirac-fermion-mediated ferromagnetism in a topological insulator," *Nature Physics*, vol. 8, pp. 729-733, Oct 2012.
- [38] D. Zhang, A. Richardella, D. W. Rench, S.-Y. Xu, A. Kandala, T. C. Flanagan, *et al.*, "Interplay between ferromagnetism, surface states, and quantum corrections in a magnetically doped topological insulator," *Physical Review B*, vol. 86, 2012.
- [39] C. Z. Chang, J. Zhang, M. Liu, Z. Zhang, X. Feng, K. Li, *et al.*, "Thin films of magnetically doped topological insulator with carrier-independent long-range ferromagnetic order," *Adv Mater*, vol. 25, pp. 1065-70, Feb 20 2013.
- [40] X. Kou, L. He, M. Lang, Y. Fan, K. Wong, Y. Jiang, *et al.*, "Manipulating surface-related ferromagnetism in modulation-doped topological insulators," *Nano Lett*, vol. 13, pp. 4587-93, Oct 9 2013.
- [41] X. Kou, M. Lang, Y. Fan, Y. Jiang, T. Nie, J. Zhang, *et al.*, "Interplay between different magnetisms in Cr-doped topological insulators," *ACS Nano*, vol. 7, pp. 9205-12, Oct 22 2013.
- [42] M. A. Ruderman and C. Kittel, "Indirect Exchange Coupling of Nuclear Magnetic Moments by Conduction Electrons," *Physical Review*, vol. 96, pp. 99-102, 1954.
- [43] T. Kasuya, "A Theory of Metallic Ferro- and Antiferromagnetism on Zener's Model,"

- Progress of Theoretical Physics*, vol. 16, pp. 45-57, 1956.
- [44] J. J. Zhu, D. X. Yao, S. C. Zhang, and K. Chang, "Electrically controllable surface magnetism on the surface of topological insulators," *Phys Rev Lett*, vol. 106, p. 097201, Mar 4 2011.
- [45] D. A. Abanin and D. A. Pesin, "Ordering of magnetic impurities and tunable electronic properties of topological insulators," *Phys Rev Lett*, vol. 106, p. 136802, Apr 1 2011.
- [46] K. v. Klitzing, G. Dorda, and M. Pepper, "New Method for High-Accuracy Determination of the Fine-Structure Constant Based on Quantized Hall Resistance," *Physical Review Letters*, vol. 45, pp. 494-497, 1980.
- [47] C. Z. Chang, J. Zhang, X. Feng, J. Shen, Z. Zhang, M. Guo, *et al.*, "Experimental observation of the quantum anomalous Hall effect in a magnetic topological insulator," *Science*, vol. 340, pp. 167-70, Apr 12 2013.
- [48] X. Kou, S. T. Guo, Y. Fan, L. Pan, M. Lang, Y. Jiang, *et al.*, "Scale-invariant quantum anomalous Hall effect in magnetic topological insulators beyond the two-dimensional limit," *Phys Rev Lett*, vol. 113, p. 137201, Sep 26 2014.
- [49] X. Kou, L. Pan, J. Wang, Y. Fan, E. S. Choi, W. L. Lee, *et al.*, "Metal-to-insulator switching in quantum anomalous Hall states," *Nat Commun*, vol. 6, p. 8474, Oct 7 2015.
- [50] C. Z. Chang, W. Zhao, D. Y. Kim, H. Zhang, B. A. Assaf, D. Heiman, *et al.*, "High-precision realization of robust quantum anomalous Hall state in a hard ferromagnetic topological insulator," *Nat Mater*, vol. 14, pp. 473-7, May 2015.
- [51] Y. Deng, Y. Yu, M. Z. Shi, Z. Guo, Z. Xu, J. Wang, *et al.*, "Quantum anomalous Hall effect in intrinsic magnetic topological insulator MnBi₂Te₄," *Science*, vol. 367, pp. 895-900, Feb 21 2020.

- [52] M. Serlin, C. L. Tschirhart, H. Polshyn, Y. Zhang, J. Zhu, K. Watanabe, *et al.*, "Intrinsic quantized anomalous Hall effect in a moire heterostructure," *Science*, vol. 367, pp. 900-903, Feb 21 2020.
- [53] T. Li, S. Jiang, B. Shen, Y. Zhang, L. Li, T. Devakul, *et al.* (2021, July 01, 2021). Quantum anomalous Hall effect from intertwined moiré bands. arXiv:2107.01796. Available: <https://ui.adsabs.harvard.edu/abs/2021arXiv210701796L>
- [54] R. D. Peccei and H. R. Quinn, "CPConservation in the Presence of Pseudoparticles," *Physical Review Letters*, vol. 38, pp. 1440-1443, 1977.
- [55] A. M. Essin, J. E. Moore, and D. Vanderbilt, "Magnetoelectric polarizability and axion electrodynamics in crystalline insulators," *Phys Rev Lett*, vol. 102, p. 146805, Apr 10 2009.
- [56] T. Morimoto, A. Furusaki, and N. Nagaosa, "Topological magnetoelectric effects in thin films of topological insulators," *Physical Review B*, vol. 92, 2015.
- [57] J. Wang, B. Lian, X.-L. Qi, and S.-C. Zhang, "Quantized topological magnetoelectric effect of the zero-plateau quantum anomalous Hall state," *Physical Review B*, vol. 92, 2015.
- [58] M. Mogi, M. Kawamura, A. Tsukazaki, R. Yoshimi, K. S. Takahashi, M. Kawasaki, *et al.*, "Tailoring tricolor structure of magnetic topological insulator for robust axion insulator," *Sci Adv*, vol. 3, p. eaao1669, Oct 2017.
- [59] L. Du, I. Knez, G. Sullivan, and R. R. Du, "Robust helical edge transport in gated InAs/GaSb bilayers," *Phys Rev Lett*, vol. 114, p. 096802, Mar 6 2015.
- [60] Y. L. Chen, J. G. Analytis, J. H. Chu, Z. K. Liu, S. K. Mo, X. L. Qi, *et al.*, "Experimental realization of a three-dimensional topological insulator, Bi₂Te₃," *Science*, vol. 325, pp.

178-81, Jul 10 2009.

- [61] A. Koma, "Van der Waals epitaxy—a new epitaxial growth method for a highly lattice-mismatched system," *Thin Solid Films*, vol. 216, pp. 72-76, 1992.
- [62] C. Weyrich, M. Drogele, J. Kampmeier, M. Eschbach, G. Mussler, T. Merzenich, *et al.*, "Growth, characterization, and transport properties of ternary $(\text{Bi}_{1-x}\text{Sb}_x)_2\text{Te}_3$ topological insulator layers," *J Phys Condens Matter*, vol. 28, p. 495501, Dec 14 2016.
- [63] L. Pan, X. Liu, Q. L. He, A. Stern, G. Yin, X. Che, *et al.*, "Probing the low-temperature limit of the quantum anomalous Hall effect," *Sci Adv*, vol. 6, p. eaaz3595, Jun 2020.
- [64] L. Pan, A. Grutter, P. Zhang, X. Che, T. Nozaki, A. Stern, *et al.*, "Observation of Quantum Anomalous Hall Effect and Exchange Interaction in Topological Insulator/Antiferromagnet Heterostructure," *Adv Mater*, vol. 32, p. e2001460, Aug 2020.
- [65] W. Li, M. Claassen, C. Z. Chang, B. Moritz, T. Jia, C. Zhang, *et al.*, "Origin of the low critical observing temperature of the quantum anomalous Hall effect in V-doped $(\text{Bi}, \text{Sb})_2\text{Te}_3$ film," *Sci Rep*, vol. 6, p. 32732, Sep 7 2016.
- [66] M. Mogi, R. Yoshimi, A. Tsukazaki, K. Yasuda, Y. Kozuka, K. S. Takahashi, *et al.*, "Magnetic modulation doping in topological insulators toward higher-temperature quantum anomalous Hall effect," *Applied Physics Letters*, vol. 107, Nov 2 2015.
- [67] J. G. Checkelsky, R. Yoshimi, A. Tsukazaki, K. S. Takahashi, Y. Kozuka, J. Falson, *et al.*, "Trajectory of the anomalous Hall effect towards the quantized state in a ferromagnetic topological insulator," *Nature Physics*, vol. 10, pp. 731-736, Oct 2014.
- [68] F. Wilczek, "Two applications of axion electrodynamics," *Phys Rev Lett*, vol. 58, pp. 1799-1802, May 4 1987.
- [69] M. Mogi, M. Kawamura, R. Yoshimi, A. Tsukazaki, Y. Kozuka, N. Shirakawa, *et al.*, "A

- magnetic heterostructure of topological insulators as a candidate for an axion insulator," *Nat Mater*, vol. 16, pp. 516-521, May 2017.
- [70] D. Xiao, J. Jiang, J. H. Shin, W. Wang, F. Wang, Y. F. Zhao, *et al.*, "Realization of the Axion Insulator State in Quantum Anomalous Hall Sandwich Heterostructures," *Phys Rev Lett*, vol. 120, p. 056801, Feb 2 2018.
- [71] C. Liu, Y. Wang, H. Li, Y. Wu, Y. Li, J. Li, *et al.*, "Robust axion insulator and Chern insulator phases in a two-dimensional antiferromagnetic topological insulator," *Nat Mater*, vol. 19, pp. 522-527, May 2020.
- [72] J. Wang, B. Lian, and S.-C. Zhang, "Universal scaling of the quantum anomalous Hall plateau transition," *Physical Review B*, vol. 89, 2014.
- [73] Y. Feng, X. Feng, Y. Ou, J. Wang, C. Liu, L. Zhang, *et al.*, "Observation of the Zero Hall Plateau in a Quantum Anomalous Hall Insulator," *Phys Rev Lett*, vol. 115, p. 126801, Sep 18 2015.
- [74] K. M. Fijalkowski, N. Liu, M. Hartl, M. Winnerlein, P. Mandal, A. Coschizza, *et al.*, "Any axion insulator must be a bulk three-dimensional topological insulator," *Physical Review B*, vol. 103, 2021.
- [75] M. Kawamura, M. Mogi, R. Yoshimi, A. Tsukazaki, Y. Kozuka, K. S. Takahashi, *et al.*, "Topological quantum phase transition in magnetic topological insulator upon magnetization rotation," *Physical Review B*, vol. 98, Oct 22 2018.
- [76] C. Z. Chang, W. Zhao, J. Li, J. K. Jain, C. Liu, J. S. Moodera, *et al.*, "Observation of the Quantum Anomalous Hall Insulator to Anderson Insulator Quantum Phase Transition and its Scaling Behavior," *Phys Rev Lett*, vol. 117, p. 126802, Sep 16 2016.
- [77] T. Nozaki, M. Al-Mahdawi, Y. Shiokawa, S. P. Pati, H. Imamura, and M. Sahaishi,

- "Magnetic anisotropy of doped Cr₂O₃ antiferromagnetic films evaluated by utilizing parasitic magnetization," *Journal of Applied Physics*, vol. 128, p. 023901, 2020.
- [78] X. Wu, D. Xiao, C. Z. Chen, J. Sun, L. Zhang, M. H. W. Chan, *et al.*, "Scaling behavior of the quantum phase transition from a quantum-anomalous-Hall insulator to an axion insulator," *Nat Commun*, vol. 11, p. 4532, Sep 10 2020.
- [79] W. Li, G. A. Csathy, D. C. Tsui, L. N. Pfeiffer, and K. W. West, "Scaling and universality of integer quantum Hall plateau-to-plateau transitions," *Phys Rev Lett*, vol. 94, p. 206807, May 27 2005.
- [80] Z. Jiang, C. Z. Chang, C. Tang, P. Wei, J. S. Moodera, and J. Shi, "Independent Tuning of Electronic Properties and Induced Ferromagnetism in Topological Insulators with Heterostructure Approach," *Nano Lett*, vol. 15, pp. 5835-40, Sep 9 2015.
- [81] W. Liu, L. He, Y. Xu, K. Murata, M. C. Onbasli, M. Lang, *et al.*, "Enhancing magnetic ordering in Cr-doped Bi₂Se₃ using high-TC ferrimagnetic insulator," *Nano Lett*, vol. 15, pp. 764-9, Jan 14 2015.
- [82] M. Li, C. Z. Chang, B. J. Kirby, M. E. Jamer, W. Cui, L. Wu, *et al.*, "Proximity-Driven Enhanced Magnetic Order at Ferromagnetic-Insulator-Magnetic-Topological-Insulator Interface," *Phys Rev Lett*, vol. 115, p. 087201, Aug 21 2015.
- [83] X. He, Y. Wang, N. Wu, A. N. Caruso, E. Vescovo, K. D. Belashchenko, *et al.*, "Robust isothermal electric control of exchange bias at room temperature," *Nat Mater*, vol. 9, pp. 579-85, Jul 2010.
- [84] T. Ashida, M. Oida, N. Shimomura, T. Nozaki, T. Shibata, and M. Sahashi, "Observation of magnetoelectric effect in Cr₂O₃/Pt/Co thin film system," *Applied Physics Letters*, vol. 104, p. 152409, 2014.

- [85] T. Ashida, M. Oida, N. Shimomura, T. Nozaki, T. Shibata, and M. Sahaishi, "Isothermal electric switching of magnetization in Cr₂O₃/Co thin film system," *Applied Physics Letters*, vol. 106, p. 132407, 2015.
- [86] W. Echtenkamp and C. Binck, "Electric control of exchange bias training," *Phys Rev Lett*, vol. 111, p. 187204, Nov 1 2013.
- [87] F. Wang, D. Xiao, W. Yuan, J. Jiang, Y. F. Zhao, L. Zhang, *et al.*, "Observation of Interfacial Antiferromagnetic Coupling between Magnetic Topological Insulator and Antiferromagnetic Insulator," *Nano Lett*, vol. 19, pp. 2945-2952, May 8 2019.
- [88] T. Nozaki, M. Al-Mahdawi, Y. Shiokawa, S. P. Pati, S. Ye, Y. Kotani, *et al.*, "Manipulation of Antiferromagnetic Spin Using Tunable Parasitic Magnetization in Magnetoelectric Antiferromagnet," *physica status solidi (RRL) – Rapid Research Letters*, vol. 12, p. 1800366, 2018.
- [89] S. Cao, X. Zhang, N. Wu, A. T. N'Diaye, G. Chen, A. K. Schmid, *et al.*, "Spin polarization asymmetry at the surface of chromia," *New Journal of Physics*, vol. 16, p. 073021, 2014.
- [90] Y. F. Zhao, R. Zhang, R. Mei, L. J. Zhou, H. Yi, Y. Q. Zhang, *et al.*, "Tuning the Chern number in quantum anomalous Hall insulators," *Nature*, vol. 588, pp. 419-423, Dec 2020.
- [91] E. Majorana, "Teoria simmetrica dell'elettrone e del positrone," *Il Nuovo Cimento*, vol. 14, pp. 171-184, 1937.
- [92] A. Y. Kitaev, "Fault-tolerant quantum computation by anyons," *Annals of Physics*, vol. 303, pp. 2-30, 2003.
- [93] F. Wilczek, "Majorana returns," *Nature Physics*, vol. 5, pp. 614-618, 2009.
- [94] C. Nayak, S. H. Simon, A. Stern, M. Freedman, and S. Das Sarma, "Non-Abelian anyons

- and topological quantum computation," *Reviews of Modern Physics*, vol. 80, pp. 1083-1159, 2008.
- [95] J. Alicea, "New directions in the pursuit of Majorana fermions in solid state systems," *Rep Prog Phys*, vol. 75, p. 076501, Jul 2012.
- [96] C. W. J. Beenakker, "Search for Majorana Fermions in Superconductors," *Annual Review of Condensed Matter Physics*, vol. 4, pp. 113-136, 2013.
- [97] A. Stern, "Non-Abelian states of matter," *Nature*, vol. 464, pp. 187-93, Mar 11 2010.
- [98] A. P. Mackenzie and Y. Maeno, "The superconductivity of Sr₂RuO₄ and the physics of spin-triplet pairing," *Reviews of Modern Physics*, vol. 75, pp. 657-712, 2003.
- [99] L. Fu and C. L. Kane, "Superconducting proximity effect and majorana fermions at the surface of a topological insulator," *Phys Rev Lett*, vol. 100, p. 096407, Mar 7 2008.
- [100] A. Das, Y. Ronen, Y. Most, Y. Oreg, M. Heiblum, and H. Shtrikman, "Zero-bias peaks and splitting in an Al–InAs nanowire topological superconductor as a signature of Majorana fermions," *Nature Physics*, vol. 8, pp. 887-895, 2012.
- [101] V. Mourik, K. Zuo, S. M. Frolov, S. R. Plissard, E. P. Bakkers, and L. P. Kouwenhoven, "Signatures of Majorana fermions in hybrid superconductor-semiconductor nanowire devices," *Science*, vol. 336, pp. 1003-7, May 25 2012.
- [102] S. M. Albrecht, A. P. Higginbotham, M. Madsen, F. Kuemmeth, T. S. Jespersen, J. Nygard, *et al.*, "Exponential protection of zero modes in Majorana islands," *Nature*, vol. 531, pp. 206-9, Mar 10 2016.
- [103] M. T. Deng, S. Vaitiekenas, E. B. Hansen, J. Danon, M. Leijnse, K. Flensberg, *et al.*, "Majorana bound state in a coupled quantum-dot hybrid-nanowire system," *Science*, vol. 354, pp. 1557-1562, Dec 23 2016.

- [104] H. Zhang, C. X. Liu, S. Gazibegovic, D. Xu, J. A. Logan, G. Wang, *et al.*, "Quantized Majorana conductance," *Nature*, vol. 556, pp. 74-79, Apr 5 2018.
- [105] J. P. Xu, M. X. Wang, Z. L. Liu, J. F. Ge, X. Yang, C. Liu, *et al.*, "Experimental detection of a Majorana mode in the core of a magnetic vortex inside a topological insulator-superconductor Bi(2)Te(3)/NbSe(2) heterostructure," *Phys Rev Lett*, vol. 114, p. 017001, Jan 9 2015.
- [106] S.-Y. Xu, N. Alidoust, I. Belopolski, A. Richardella, C. Liu, M. Neupane, *et al.*, "Momentum-space imaging of Cooper pairing in a half-Dirac-gas topological superconductor," *Nature Physics*, vol. 10, pp. 943-950, 2014.
- [107] J. Wang, Q. Zhou, B. Lian, and S.-C. Zhang, "Chiral topological superconductor and half-integer conductance plateau from quantum anomalous Hall plateau transition," *Physical Review B*, vol. 92, 2015.
- [108] Q. L. He, L. Pan, A. L. Stem, E. C. Burks, X. Che, G. Yin, *et al.*, "Chiral Majorana fermion modes in a quantum anomalous Hall insulator-superconductor structure," *Science*, vol. 357, pp. 294-299, Jul 21 2017.
- [109] M. Kayyalha, D. Xiao, R. Zhang, J. Shin, J. Jiang, F. Wang, *et al.*, "Absence of evidence for chiral Majorana modes in quantum anomalous Hall-superconductor devices," *Science*, vol. 367, pp. 64-67, Jan 3 2020.
- [110] Y. Y. Huang, F. Setiawan, and J. D. Sau, "Disorder-induced half-integer quantized conductance plateau in quantum anomalous Hall insulator-superconductor structures," *Physical Review B*, vol. 97, Mar 9 2018.
- [111] W. Ji and X. G. Wen, " $1/2(e^2/h)$ Conductance Plateau without 1D Chiral Majorana Fermions," *Phys Rev Lett*, vol. 120, p. 107002, Mar 9 2018.

- [112] M. Buttiker, "Absence of backscattering in the quantum Hall effect in multiprobe conductors," *Phys Rev B Condens Matter*, vol. 38, pp. 9375-9389, Nov 15 1988.
- [113] C. Z. Chang, W. Zhao, D. Y. Kim, P. Wei, J. K. Jain, C. Liu, *et al.*, "Zero-Field Dissipationless Chiral Edge Transport and the Nature of Dissipation in the Quantum Anomalous Hall State," *Phys Rev Lett*, vol. 115, p. 057206, Jul 31 2015.
- [114] K. Yasuda, M. Mogi, R. Yoshimi, A. Tsukazaki, K. S. Takahashi, M. Kawasaki, *et al.*, "Quantized chiral edge conduction on domain walls of a magnetic topological insulator," *Science*, vol. 358, pp. 1311-1314, Dec 8 2017.
- [115] M. Kawamura, R. Yoshimi, A. Tsukazaki, K. S. Takahashi, M. Kawasaki, and Y. Tokura, "Current-Driven Instability of the Quantum Anomalous Hall Effect in Ferromagnetic Topological Insulators," *Phys Rev Lett*, vol. 119, p. 016803, Jul 7 2017.
- [116] M. Allen, Y. Cui, E. Yue Ma, M. Mogi, M. Kawamura, I. C. Fulga, *et al.*, "Visualization of an axion insulating state at the transition between 2 chiral quantum anomalous Hall states," *Proc Natl Acad Sci U S A*, vol. 116, pp. 14511-14515, Jul 16 2019.
- [117] A. J. Bestwick, E. J. Fox, X. Kou, L. Pan, K. L. Wang, and D. Goldhaber-Gordon, "Precise Quantization of the Anomalous Hall Effect near Zero Magnetic Field," *Phys Rev Lett*, vol. 114, p. 187201, May 8 2015.
- [118] E. J. Fox, I. T. Rosen, Y. Yang, G. R. Jones, R. E. Elmquist, X. Kou, *et al.*, "Part-per-million quantization and current-induced breakdown of the quantum anomalous Hall effect," *Phys Rev B*, vol. 98, Aug 27 2018.
- [119] L. K. Rodenbach, I. T. Rosen, E. J. Fox, P. Zhang, L. Pan, K. L. Wang, *et al.*, "Bulk dissipation in the quantum anomalous Hall effect," *APL Materials*, vol. 9, p. 081116, 2021.

- [120] S.-W. Wang, D. Xiao, Z. Dou, M. Cao, Y.-F. Zhao, N. Samarth, *et al.*, "Demonstration of Dissipative Quasihelical Edge Transport in Quantum Anomalous Hall Insulators," *Physical Review Letters*, vol. 125, 2020.
- [121] G. Lippertz, A. Bliesener, A. Uday, L. M. C. Pereira, A. A. Taskin, and Y. Ando. (2021, August 01, 2021). Current-induced breakdown of the quantum anomalous Hall effect. arXiv:2108.02081. Available: <https://ui.adsabs.harvard.edu/abs/2021arXiv210802081L>
- [122] X. Qian, J. Liu, L. Fu, and J. Li, "Solid state theory. Quantum spin Hall effect in two-dimensional transition metal dichalcogenides," *Science*, vol. 346, pp. 1344-7, Dec 12 2014.
- [123] J. Wang, B. Lian, and S. C. Zhang, "Electrically Tunable Magnetism in Magnetic Topological Insulators," *Phys Rev Lett*, vol. 115, p. 036805, Jul 17 2015.
- [124] K. Wang, Y. Liu, W. Wang, N. Meyer, L. H. Bao, L. He, *et al.*, "High-quality Bi₂Te₃ thin films grown on mica substrates for potential optoelectronic applications," *Applied Physics Letters*, vol. 103, p. 031605, 2013.
- [125] Y. Huang, Y. H. Pan, R. Yang, L. H. Bao, L. Meng, H. L. Luo, *et al.*, "Universal mechanical exfoliation of large-area 2D crystals," *Nat Commun*, vol. 11, p. 2453, May 15 2020.
- [126] Z. Zhang, X. Feng, J. Wang, B. Lian, J. Zhang, C. Chang, *et al.*, "Magnetic quantum phase transition in Cr-doped Bi₂(S₆Te_{1-x})₃ driven by the Stark effect," *Nat Nanotechnol*, vol. 12, pp. 953-957, Oct 2017.
- [127] T. Zhang, J. Ha, N. Levy, Y. Kuk, and J. Stroscio, "Electric-field tuning of the surface band structure of topological insulator Sb₂Te₃ thin films," *Phys Rev Lett*, vol. 111, p. 056803, Aug 2 2013.